

Multi-wavelength photoacoustic imaging of the atherosclerotic carotid artery

Citation for published version (APA):

Arabul, M. U. (2018). *Multi-wavelength photoacoustic imaging of the atherosclerotic carotid artery: a preclinical feasibility study*. [Phd Thesis 1 (Research TU/e / Graduation TU/e), Biomedical Engineering]. Technische Universiteit Eindhoven.

Document status and date:

Published: 07/12/2018

Document Version:

Publisher's PDF, also known as Version of Record (includes final page, issue and volume numbers)

Please check the document version of this publication:

- A submitted manuscript is the version of the article upon submission and before peer-review. There can be important differences between the submitted version and the official published version of record. People interested in the research are advised to contact the author for the final version of the publication, or visit the DOI to the publisher's website.
- The final author version and the galley proof are versions of the publication after peer review.
- The final published version features the final layout of the paper including the volume, issue and page numbers.

[Link to publication](#)

General rights

Copyright and moral rights for the publications made accessible in the public portal are retained by the authors and/or other copyright owners and it is a condition of accessing publications that users recognise and abide by the legal requirements associated with these rights.

- Users may download and print one copy of any publication from the public portal for the purpose of private study or research.
- You may not further distribute the material or use it for any profit-making activity or commercial gain
- You may freely distribute the URL identifying the publication in the public portal.

If the publication is distributed under the terms of Article 25fa of the Dutch Copyright Act, indicated by the "Taverne" license above, please follow below link for the End User Agreement:

www.tue.nl/taverne

Take down policy

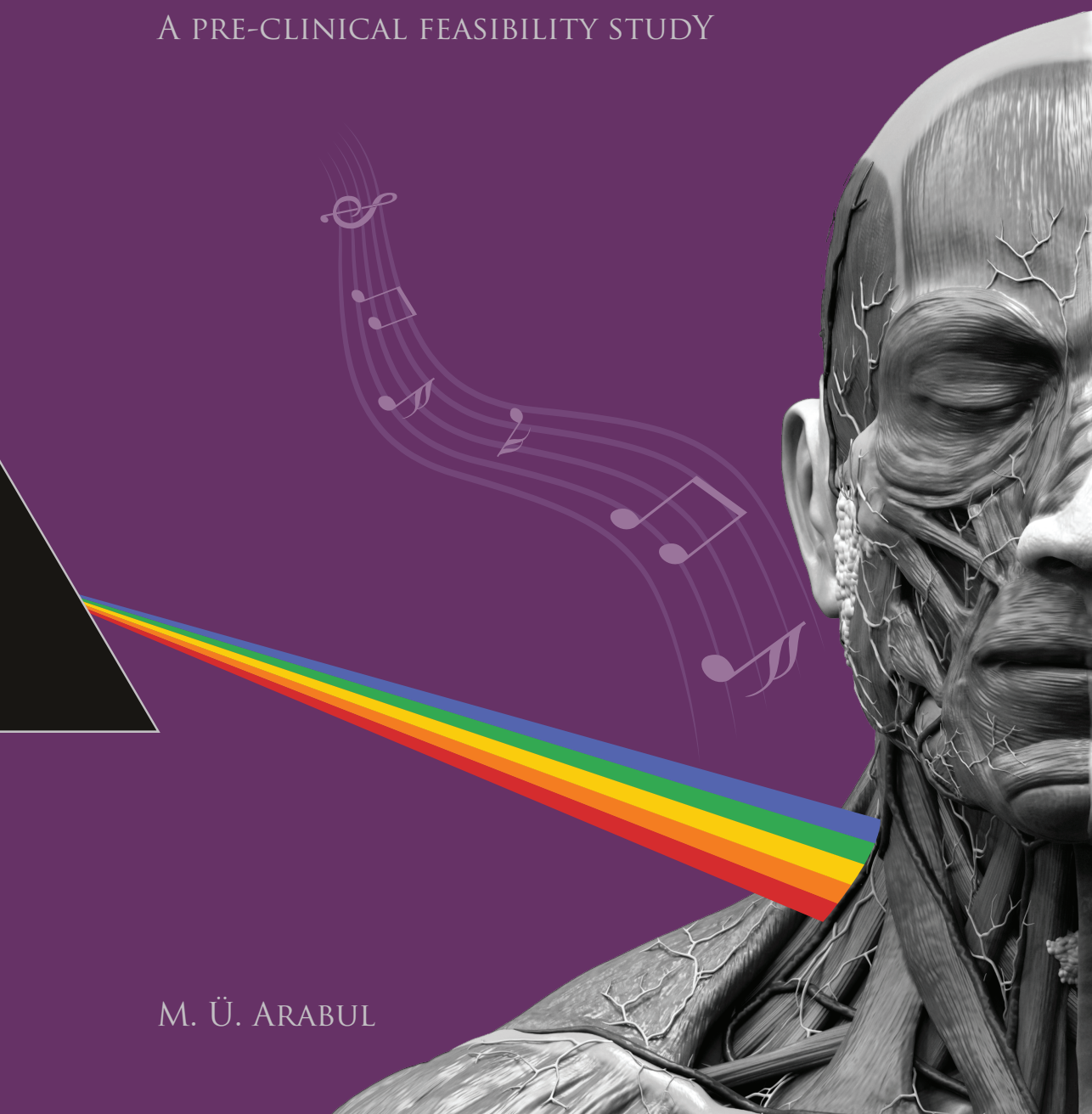
If you believe that this document breaches copyright please contact us at:

openaccess@tue.nl

providing details and we will investigate your claim.

MULTI-WAVELENGTH PHOTOACOUSTIC IMAGING OF THE ATHEROSCLEROTIC CAROTID ARTERY

A PRE-CLINICAL FEASIBILITY STUDY



M. Ü. ARABUL

**MULTI-WAVELENGTH
PHOTOACOUSTIC IMAGING
OF THE ATHEROSCLEROTIC
CAROTID ARTERY**

A preclinical feasibility study

M. Ü. Arabul

The research discussed in this thesis was funded by the FULLPHASE (EU FP7 Programme) and CVENT (EU Horizon 2020 Programme) projects.

A catalogue record is available from the Eindhoven University of Technology Library
ISBN: 978-94-6380-166-9

Printed by: ProefschriftMaken || www.proefschriftmaken.nl
Cover Design: M. Ü. Arabul, Illustration: Stock Photo (64471508 - 123RF.com)

The printing of this thesis was supported by Esaote Europe and Lumibirds (formerly Quantel).

Financial support by the Dutch Heart Foundation for the publication of this thesis is gratefully acknowledged.

© Copyright 2018, M. Ü. Arabul

All rights reserved. No part of this publication may be reproduced, stored in a retrieval system, or transmitted, in any form or by any means, electronic, mechanical, photocopying, recording or otherwise, without the prior written permission from the copyright owner.

MULTI-WAVELENGTH PHOTOACOUSTIC IMAGING OF THE ATHEROSCLEROTIC CAROTID ARTERY

A preclinical feasibility study

PROEFSCHRIFT

ter verkrijging van de graad van doctor aan de
Technische Universiteit Eindhoven, op gezag van de
Rector Magnificus, prof.dr.ir. F.P.T. Baaijens, voor een
commissie aangewezen door het College voor
Promoties in het openbaar te verdedigen
op vrijdag 7 december 2018 om 13.30 uur

door

Mustafa Ümit Arabul

geboren te Istanbul, Turkije

Dit proefschrift is goedgekeurd door de promotoren en de samenstelling van de promotiecommissie is als volgt:

voorzitter:	prof.dr. P.A.J. Hilbers
1e promotor:	prof.dr.ir. F.N. van de Vosse
Copromotor:	dr.ir. R.G.P Lopata
2e Copromotor:	dr.ir. M.C.M. Rutten
leden:	prof.dr. G. Schmitz
	prof.dr.ir. C.L. de Korte
	prof.dr.ir. M.W.J. Prins
adviseur:	prof.dr. M.R.H.M. van Sambeek

Het onderzoek of ontwerp dat in dit proefschrift wordt beschreven is uitgevoerd in overeenstemming met de TU/e Gedragscodex Wetenschapsbeoefening.

To the "Academics for Peace" *

* In total, 517 scholars were suspended (January 2016 - September 2018) from the universities in Turkey for signing a petition for "Peace".

Contents

Summary	xi
1 General Introduction	1
1.1 Atherosclerosis Disease of Carotid Artery	3
1.2 Photoacoustic imaging of carotid atherosclerosis	5
1.3 Rationale and outline of the thesis	8
2 <i>Ex vivo</i> photoacoustic imaging of carotid plaques	11
2.1 Abstract	12
2.2 Introduction	12
2.3 Methods	15
2.3.1 Sample Preparation and Experimental Setup	15
2.3.2 Hand-held Photoacoustic Probe	16
2.3.3 Scanning Protocol	16
2.3.4 Post Processing	16
2.3.5 Histology Comparison	17
2.4 Results	18
2.5 Discussion	20
2.6 Conclusion	23
2.7 Acknowledgments	23
3 Spatial compounding of photoacoustic images	25

3.1	Abstract	26
3.2	Introduction	26
3.3	Materials and Methods	28
3.3.1	Phantoms and Plaque Samples	28
3.3.2	Experiment Setup and Imaging Device	29
3.3.3	Experimental Procedure	30
3.3.4	Compounding Method	31
3.3.5	Image Quantification	32
3.4	Results	33
3.4.1	PVA Phantom Experiments	33
3.4.2	<i>Ex vivo</i> Plaque Samples	36
3.5	Discussion	38
3.6	Conclusion	41
3.7	Acknowledgments	41
4	Multi-wavelength PA unmixing	43
4.1	Abstract	44
4.2	Introduction	44
4.3	Materials and Methods	46
4.3.1	Sample Preparation for Imaging	46
4.3.2	Scanning setup and photoacoustic acquisition system	47
4.3.3	Experiment Protocol	48
4.3.4	Blind Source Spectral Unmixing	49
4.3.5	Histology Procedure	50
4.4	Results	51
4.5	Discussion	55
4.6	Conclusion	57
4.7	Acknowledgments	58
4.8	Supplementary Materials	58
4.8.1	ICA overview of plaque section	58
4.8.2	Convergence MSE values of ICA	58
5	Photoacoustic simulation tool-chain	61
5.1	Introduction	62
5.2	Materials and methods	64
5.2.1	Monte Carlo Photon Migration	64

5.2.2	Acoustic Wave Propagation	67
5.2.3	Simulations	68
5.3	Results	70
5.3.1	Sphere Simulations	70
5.3.2	Human Carotid Sample Simulation	72
5.4	Discussion	74
5.5	Conclusion	76
5.6	Supporting information	77
5.6.1	Kerf Analysis	77
5.7	Acknowledgments	78
6	General Discussion	79
6.1	General Limitations	82
6.2	Outlook	84
	Curriculum Vitae	87
	Acknowledgments	89
	List of Publications	93
	Peer-Reviewed Journal Publications	93
	Conference Publications	94

Summary

The circulatory system is responsible for the delivery of nutrition and oxygen to organs and tissues by the supply of blood through the heart and vessels. Due to various reasons, such as high blood pressure, obesity, poor or unhealthy dietary, smoking, etc., the functionality of the circulatory system can be disrupted leading to cardiovascular diseases (CVDs). The prevalence of CVDs is the highest according to the latest reports from the World Health Organisation (WHO) [1]. Therefore, CVDs are constantly attracting the scientific community to develop new diagnosis and treatment methods.

Stroke is one of the severe consequences of CVDs, leading to disability or even mortality. One of the causes of stroke is the rupture of an atherosclerotic plaque in the carotid artery. Prevention of stroke can be achieved by removing the plaque by endarterectomy surgery or carotid stenting. According to medical guidelines [2], the decision criterion for this surgery is based on the level of stenosis being above 50% obtained from duplex ultrasound (US) images [3]. However, this criterion does not indicate the patient-specific risk of rupture of the plaques. Studies showed that only 16% of the patients undergoing endarterectomy surgery actually had a vulnerable plaque and thus gained from surgery by a reduction in the risk of stroke [4]. Retrospective studies demonstrated the typical characteristics of rupture-prone carotid plaques such as intraplaque hemorrhages, necrotic lipid pool, thin fibrous cap, macrophages [5]–[9], all of which are related to the composition of the plaque rather than the level of stenosis.

US images are created based on the echoes from boundaries between tissues with dif-

ferent stiffness. However, those differences are negligible within a plaque, so there is no contrast between different tissue types; hence, the specificity of US is not sufficient to obtain tissue morphology of carotid plaques.

Although the acoustic contrast is low, the optical absorption properties differ between those components. Nevertheless, carotid tissue typically is located at 1-2 cm depth from the skin surface, and pure optical detection is difficult due to high scattering of light. On the other hand, with photoacoustics, it is possible to overcome this restriction and measure the ultrasonic response of tissue to light.

In photoacoustics, a short laser pulse is sent into the tissue. When the laser light hits the tissue, it penetrates into the tissue while subjected to scattering and absorption. Once the light reaches a site that absorbs light significantly more than its surroundings, the optical energy is absorbed and converted into heat, which causes a temperature rise in the order of mK. The temperature rise is so sudden that it creates a thermoelastic expansion resulting in a pressure wave that propagates through the tissue as ultrasound. This phenomenon is called photoacoustics (PA) and can provide the optical contrast of the tissue with acoustic resolution.

Depending on the composition of the irradiated material, the acoustic response varies with different wavelength of light. To make an analogy, this can be considered as hearing the 'colors' of the tissue (see the cover). In a sense, there is a light-driven orchestra of the biological tissue that we can listen to with an ultrasound transducer.

In this thesis, we investigated the merit of PA imaging for the morphology assessment and, indirectly, vulnerability assessment of carotid plaques. A novel hand-held system, suitable for clinical use, was used in this thesis. The laser was integrated into the probe, which limits the energy of the laser pulses used. Since the targeted tissue is surrounded by soft tissues (skin, subcutaneous fat, muscle and connective tissue) that absorb and scatter the light, we worked on *ex vivo* human carotid samples for preclinical validation of the methods. We demonstrated that using only one optical excitation wavelength, it is possible to create images of the so-called intraplaque hemorrhages in the human plaque samples. The detection of intraplaque hemorrhages is clinically essential since they have been found to be important markers of plaque vulnerability [10]–[12]. Next, we developed a novel experimental approach

that allows compounding multiple data from different acquisitions from different rotational positions to elevate the quality of the PA images. We showed that this method could be beneficial when applied *in vivo* with the limited available view angles. Next, we used multi-wavelength PA imaging on *ex vivo* carotid plaques and demonstrated that we could discriminate recent hemorrhages from old hemorrhages using a blind-source spectral unmixing method. Furthermore, we found evidence that PA unmixing might detect signatures of cholesterol clefts. Lastly, we created a tool-chain to simulate PA generation starting from optics to acoustic wave generation and, finally, image reconstruction. Using this tool-chain, PA images were successfully replicated in simulations of the experimental setup including out-of-plane clutter sources. This simulation tool can be used as a benchmarking platform for newly developed experimental approaches in PA imaging and can provide an additional dimension of validation for techniques such as clutter removal techniques, new compounding algorithms, and spectral unmixing techniques.

To sum up, this thesis contributes to the scientific knowledge in photoacoustic imaging, and its application to cardiovascular diseases. It is also a first step in making PA technology clinically available in the near future, offering medical professionals a more advanced tool for improved diagnosis of carotid plaques, which may aid in a reduction in the overall risk of stroke and prevention of overtreatment.

Chapter 1

General Introduction

The aim of medical imaging is to make the human body visible at different scales. Different contrast mechanisms are utilized to obtain partial or full images of the human body, in either a non-invasive or (minimally) invasive manner. The four major imaging modalities are plain X-ray imaging, computed tomography (CT), magnetic resonance imaging (MRI) and ultrasound (US), each of which utilizes different contrast mechanism. Plain X-ray and CT uses radiodensity (i.e., X-ray attenuation), whereas MRI uses the decay time of the transient magnetic signal (related to proton density) to create the contrast between different tissue types in the final images. Ultrasound (US) uses acoustic waves, forming images from the backscattered sound caused by differences in the mechanical stiffness and density (acoustic impedance) of biological tissues as well as small inhomogeneities present in the tissue.

All four modalities are widely used in clinical practice and have their advantages and disadvantages [12], [13]. Among the four, US has the advantage of being non-invasive, inexpensive, portable and practical. Recent technological advancements in hardware led to the further miniaturization of US devices that can be used with a tablet or smartphone [14], [15]. Moreover, due to its high temporal resolution, US is also widely used for real-time functional imaging, especially in cardiovascular applications [16], [17]. Ultrafast image acquisition rates, on the order of 10 kHz, enabled further functional imaging areas in cardiovascular elastography and flow imaging [18]–[20]. Due to the aforementioned advantages, US is a widely preferred imaging modality for diagnosis, monitoring, and treatment follow-up for cardiovascular diseases. It is also the most frequently used modality for the assessment of atherosclerotic disease of the carotid artery (see the Section 1.1). However, there are still unmet needs in improving US-based diagnosis of so-called vulnerable atherosclerotic plaques and assessment of their risk of rupture.

This thesis focuses on atherosclerotic disease in the carotid artery as the core medical problem and investigates the feasibility of potentially non-invasive photoacoustic imaging (see the Section 1.2) to complement or replace conventional US imaging in the diagnosis of carotid plaque disease.

1.1 Atherosclerosis Disease of Carotid Artery

The carotid arteries (CA) are the principal arteries that supply nutrition and oxygenated blood to the brain and are located on either side of the neck. The common carotid artery (CCA), branches into the internal carotid artery (ICA) that is the main supplier for most of the brain, and the external carotid artery (ECA) that supplies the more superficial tissues and organs in the head and face (see Figure 1.1). A healthy carotid artery has three layers: the adventitia, media, and intima (see Figure 1.1). The outermost layer, the adventitia, comprises mainly collagen type-I fibers, which provide elasticity and reinforces the artery to adapt to varying blood pressure. The adventitia also has the role of attaching the artery to the surrounding tissue [21]. The media is the thickest layer which mostly consists of smooth muscle cells and circumferentially oriented elastin fibers [22]. The innermost layer, the intima, is composed of endothelial cells that form the lumen border [23]. Each carotid artery

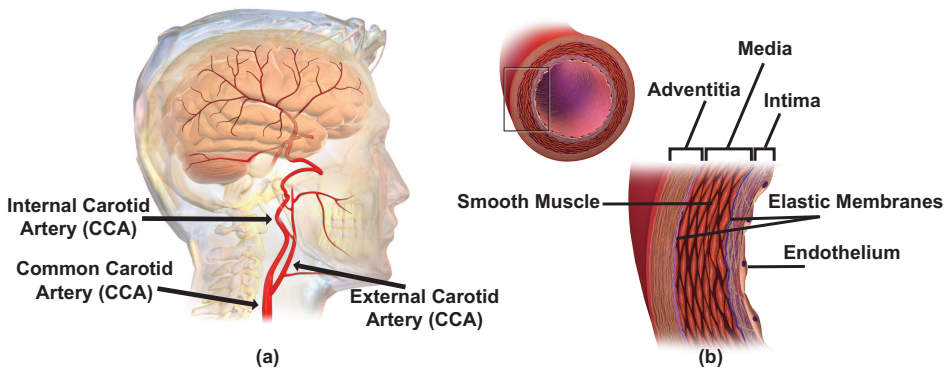


Figure 1.1: Illustration of (a) the carotid artery bifurcation and (b) the structure of a healthy artery cross-section [24]. [Retrieved from Wikimedia Commons, CC3 License]

is subjected to structural and morphological transformations with aging. Although the age-related morphological changes (such as intima-media thickening, diameter increase and stiffening of the arterial wall) are usual, occasionally, pathological morphological changes occur that can lead to atherosclerotic plaque formation (See Figure 1.2). The complete mechanism of plaque formation is not known yet. However, the lesions are inflammatory and believed to be related to the immune response of

the body (see Figure 1.2).

Plaque growth inside the artery wall ultimately leads to stenosis and disturbs the blood flow to the brain. In case of a stenosed carotid artery, blood supply to the brain can be compensated through a complete system of cerebral flow autoregulation and contralateral carotid artery, or the vertebral arteries [25]. However, plaques can also be unstable and therefore prone to rupture. Once ruptured, the content of the plaque can leak into the bloodstream, forming blood clots, which can migrate downstream into smaller branches of the artery in the brain. Eventually, this can lead to an embolism in the brain and cause an ischemic stroke. Stroke-induced mor-

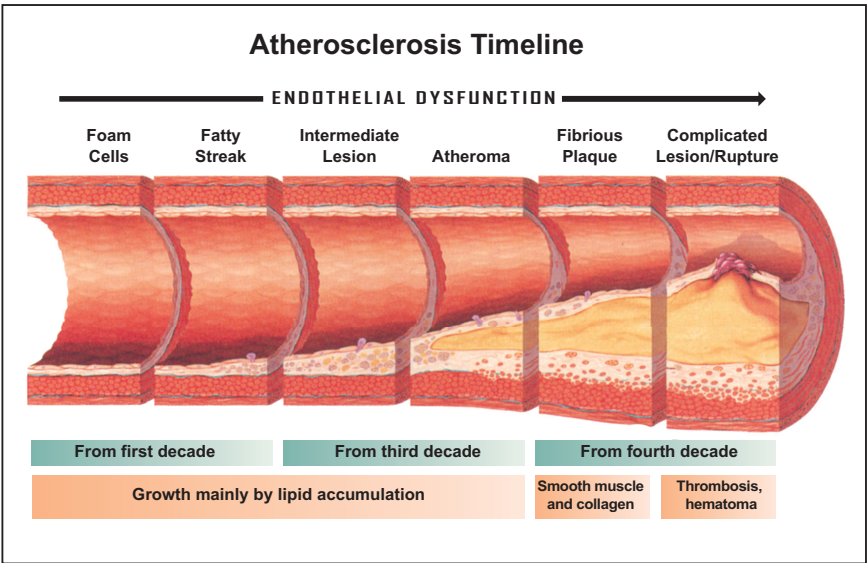


Figure 1.2: Illustration of atherosclerosis in different stages of its progression. Reprinted with permission [26]

tality rate is high and account for over 11% of total deaths worldwide [27]. One of the primary causes of stroke is the sudden rupture of an atherosclerotic plaque in the carotid artery (20-25% of all stroke cases) as described in the previous paragraph. Depending on the sites of the embolism in the brain, stroke can lead to speech impairments, paralysis, unconsciousness, and even death. Hence, stroke is associated with high rates of mortality, co-morbidities, life-long disability, and a reduction in the quality-of-life in general [28], [29].

Symptomatic patients undergo duplex ultrasound (B-mode and Doppler ultrasound) for diagnosis of atherosclerotic carotid disease. The severity of the stenosis is determined, based on the structural and functional measurements obtained from duplex US. The ratio of the ICA peak systolic velocity (PSV) to the CCA PSV or end-diastolic velocity is used as the decision criterion for intervention [30]–[32]. Current clinical practice regarding treatment is to remove the plaque with an endarterectomy surgery or carotid artery stenting. The criterion of stenosis grade is based on extensive population studies but does not assess patient-specific plaque vulnerability. Moreover, retrospective studies showed that vulnerability of a plaque is more related to the composition of plaques rather than the level of stenosis [4]. As a result, it requires an endarterectomy intervention in nine symptomatic patients to prevent a stroke happening in one of them. For asymptomatic patients this is even one out of nineteen [33].

The characteristic features of vulnerable plaques are the presence of intra-plaque hemorrhages, a necrotic lipid core, and a thin fibrous cap [8], [34], [35]. Since the acoustic properties of those composition materials are quite similar, there is not enough acoustic contrast in the US images to identify those components using B-mode imaging alone. However, there is a clear distinction in the optical absorption spectra of different tissue components (See Figure 1.3) [36]. At this point, photoacoustic imaging (PAI) can be a promising technique to fill the gap by providing a high tissue specificity with the resolution of ultrasound (US) imaging. Hybrid modalities, for instance, US combined with multi-wavelength PAI, have the potential to reveal the morphology of carotid plaques within a geometrical image, whereas the gray values of US images alone do not. However, the scattering of light in turbid tissue is significantly high, so pure optical detection of the optical absorption is cumbersome especially for source localization [37].

1.2 Photoacoustic imaging of carotid atherosclerosis

The discovery of the phenomenon of photoacoustics (also known as optoacoustics) dates back to 1880 when Alexander Graham Bell describes his findings as hearing the voice of the sunlight. In his letter, he stated this as: "I have heard a ray of sun laugh and cough and sing!" [39]. However, the technology that utilizes photoacous-

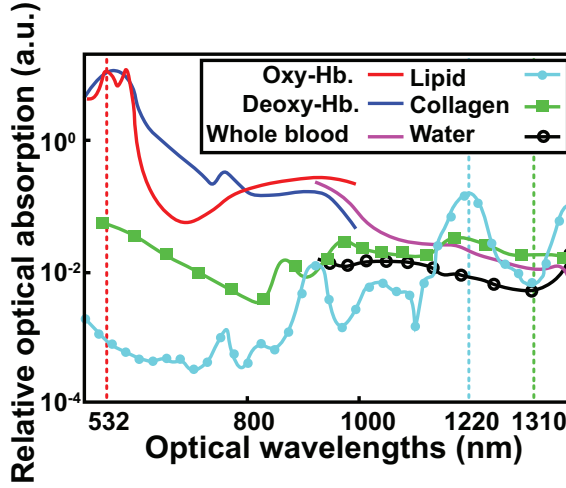


Figure 1.3: Optical absorption spectra of the main components of the biological tissue. Reprinted with permission [38]

tics to create images of optic absorption of the biological tissue only became possible in the 1970s with the developments in lasers and ultrasonic transducer technology [40]–[42].

The mechanism of photoacoustic wave generation is based on the thermoelastic expansion of the tissue due to light absorption. When tissue is illuminated with short-pulsed laser light (on the order of nanoseconds), the photons propagate into the tissue subjected to scattering and absorption. Once the light is absorbed by a chromophore, the optical energy is converted into heat which creates a thermoelastic expansion of the local tissue and sudden pressure rise in the absorber site. The overall efficiency of this momentum transfer from optics to pressure wave is related to the Grüneisen coefficient Γ (dimensionless) and the conversion ratio constant η_{th} (dimensionless) of the material, which can be formulated as [43]

$$p_0 = \Gamma \eta_{th} \mu_a(r_0) \Phi(r_0) \quad (1.1)$$

where μ_a (cm^{-1}) is the absorption, and $\Phi(r_0)$ (J/cm^2) is the optical fluence at the location of the absorber, r_0 . The pressure wave generated, $p(\vec{r}, t)$ (MPa), is in the ultrasonic range of frequencies. Since the amplitude of pressures are generally low

($p < 1$ kPa), wave propagation can be modeled by the linear, inhomogeneous, 3-D wave equation:

$$\left(\nabla^2 - \frac{1}{v_s^2} \frac{\partial^2}{\partial t^2} \right) p(\vec{r}, t) = \frac{-\beta}{C_p} \frac{\partial H(\vec{r}, t)}{\partial t}. \quad (1.2)$$

Here v_s (m/s) denotes the speed of pressure wave, β (K^{-1}) denotes the thermal coefficient of volume expansion, and C_p (J/kg.K) denotes the specific heat capacities at constant pressure. The input, or source function of Eq. 1.2 is represented by the heating function $H(\vec{r}, t)$, which depends on the spatio-temporal profile of the laser source [44], [45].

Next, the US waves propagate through the tissue and can be detected at the skin surface by a conventional (or custom) ultrasonic transducer. Finally, the initial pressure distribution can be reconstructed using back-projection [43], linear inversion [46], or k-space reconstruction [47] depending on the sensor positions and geometry. The differences in the Grüneisen coefficient Γ and the conversion ratio η_{th} are neglected for biological soft tissues [48]. Therefore, the reconstructed pressure map can be assumed to represent the absorption coefficient map of the tissue.

The use of PA from microscopic scale to mesoscopic scale was reported by different research groups [43], [48]–[54]. The molecular imaging of PA enables functional imaging using various endogenous [55], [56] and exogenous [57], [58] chromophores.

Blood is a strong endogenous chromophore that is highly absorbing in the near-infrared region of the optical spectrum. Therefore, PA was widely used for detection of vasculatures in small animals [59], [60], in cancerous lesions [61], [62], in finger joints for early detection of rheumatoid arthritis disease [63]–[65], and in skin [66]–[68].

The use of PA is also appealing for plaque characterization due to the high tissue specificity of PA. Intravascular photoacoustic (IVPA) imaging has demonstrated promising results for coronary artery plaques. IVPA has the advantage of encountering a short optical path to the target tissue, and therefore one can deliver the optical energy with less depletion. Previously, imaging of lipids [69]–[71] and macrophages [72], [73] was demonstrated using IVPA in phantoms and animal models.

Clinically, invasive detection with IVPA will not be preferred over non-invasive US for diagnosis of atherosclerotic disease of the carotid artery, which is a relatively superficial organ (1.5 – 3.0 cm below the skin surface) [23]. Hence, a non-invasive PA measurement of carotid artery plaque is desired. Previously, non-invasive PA imaging attempts for imaging carotid artery were made using concave custom-designed ultrasound transducer on healthy volunteers [74], [75], and minimally invasive method using optical illumination via the pharynx on a human neck phantom [76]. So far, the technique has not found its way to the clinic due to technical and practical limitations, such as the limited penetration depth, and the lack of handheld systems suitable for clinical use.

1.3 Rationale and outline of the thesis

The current clinical approach to reduce the risk of stroke is the removal of the atherosclerotic plaque from the artery using endarterectomy. The threshold to decide in favor of an operation is the 50% stenosis level, which is based on extensive population studies and does not assess patient-specific plaque vulnerability. A patient can have up to 99% stenosis but a structurally stable carotid plaque [4]. Therefore there is an unmet need to characterize the vulnerability of carotid plaques by assessing the composition of the plaque. Although the contrast between the components of plaques is low in conventional ultrasound imaging, photoacoustic imaging has the potential to reveal the morphology utilizing the optical absorption differences between the typical morphological signatures of vulnerable plaques such as the presence of intra-plaque hemorrhages, a necrotic lipid core, and a thin fibrous cap.

The aforementioned studies found in the literature were not able to draw any conclusion regarding *in vivo* carotid plaque characterization with PA. This is mostly due to the complex nature of the plaque morphology in the later phases of plaque progression. Moreover, the skin and connective soft tissue around the carotid artery results in a severe reduction of the optical energy delivered to the chromophores, producing low amplitude photoacoustic waves, which leads to low signal-to-noise (SNR) ratio of the PA signals.

In this thesis, we describe preclinical studies performed to investigate the applicability and the potential of PAI in plaque characterization using a multi-wavelength, hand-held PA device. To show the feasibility of PA in plaque imaging, we designed and performed a series of *ex vivo* experiments using a novel hand-held PA probe that was designed for clinical use. In other words, reduce complexity from *in vivo* to experiment, before taking the techniques into the reverse direction.

In Chapter 2, the merit of the novel PA probe regarding plaque imaging and hemorrhage detection was investigated using a single wavelength. Additional to the use of a novel PA system, an experimental setup for *ex vivo* imaging of human carotid plaque samples was introduced.

In Chapter 3, the performance of the novel experimental setup was characterized with a series of phantom experiments. Spatial compounding and its merits regarding penetration depth, SNR and contrast-to-noise ratio (CNR) were investigated considering future *in vivo* application.

In Chapter 4, the latest prototype of the PA probe with four available wavelengths ($\lambda = 808, 915, 940, 980$ nm) was used to obtain information on the composition of human carotid plaque samples. Since the PA response at any wavelength is the collective contribution of different chromophores, a blind-source spectral unmixing technique was adopted to separate the individual chromophores. Additionally, a verification experiment was performed using PVA vessel phantoms with three inclusions: fresh porcine blood to mimic recent hemorrhages, thrombus to mimic old hemorrhages, and pure cholesterol to mimic fatty streaks.

Finally, in Chapter 5, a PA simulation tool-chain was established by coupling the output of mesh-based Monte Carlo photon distribution simulations to acoustic simulations in k-Wave. Hence, a validation scheme was created for the previously developed methods such as spatial compounding and blind-source unmixing. Furthermore, it is now possible to perform prospective tests of novel techniques that are developed prior to *in vivo* application, such as photoacoustic clutter reduction.

Chapter 2

Towards the detection of intraplaque hemorrhage in carotid artery lesions using photoacoustic imaging

The content of this chapter is based on M. U. Arabul, M. Heres, M. C. M. Rutten, M. R. van Sambeek, F. N. van de Vosse, and R. G. P. Lopata, "Toward the detection of intraplaque hemorrhage in carotid artery lesions using photoacoustic imaging," J. Biomed. Opt., vol. 22, no. 4, p. 041010, Dec. 2016.

2.1 Abstract

Photoacoustic imaging (PAI) may have the ability to reveal the composition and the anatomical structure of carotid plaques, which determines its mechanical properties and vulnerability. In this study, we used PAI and plane-wave ultrasound (PUS) imaging to obtain 3D images of endarterectomy samples *ex-vivo*, and compared the results with histology to investigate the potential of PAI-based identification of intraplaque hemorrhage. Seven carotid plaque samples were obtained from patients undergoing carotid endarterectomy, and imaged with a fully integrated hand-held photoacoustic (PA) probe, consisting of a pulsed diode laser ($t_{pulse} = 130$ ns, $E_{pulse} = 1$ mJ, $\lambda = 808$ nm) and a linear array transducer ($f_c = 7.5$ MHz). The samples were rotated 360° with 10° steps and data were spatially compounded to obtain complete 3D images of the plaques. Areas of high absorption in the 3D datasets were identified and compared to histological data of the plaques. Data in six out of seven endarterectomy samples revealed the presence of intraplaque hemorrhages, which were not visible in the PUS images. Due to the noninvasive nature of PAI, this *ex vivo* study may elucidate preclinical studies towards the *in vivo*, noninvasive, vulnerability assessment of the atherosclerotic carotid plaque.

2.2 Introduction

The abrupt rupture of an atherosclerotic carotid plaque is one of the main causes of stroke and stroke-induced death [27], [77]. Current practice to prevent stroke in patients with a significant carotid stenosis is the removal of the plaque during an endarterectomy procedure. The current decision-making procedure for patients with atherosclerotic plaques to undergo an endarterectomy is based on the severity of stenosis. However, a study by Rothwell and Warlow [4] has shown that only 16% of the patients that underwent endarterectomy, based on the degree of the stenosis of their carotid plaque (70 – 99%), were really at risk to suffer from stroke in a 5-year period. Although the complete rupture mechanism is not resolved yet, there is a strong evidence supporting the hypothesis of plaque composition playing a key role in plaque rupture rather than the degree of stenosis [31], [34].

Retrospective studies have demonstrated that the common features of the risk of

plaque rupture are the existence of a large lipid necrotic core, a thin fibrous cap over the core, and intraplaque hemorrhages [5], [7], [9]. However, common clinical practice is still based on the estimation of the degree of stenosis based on duplex ultrasound. In case ultrasonography was insufficient due to excessive calcifications in the plaque, additional magnetic resonance imaging (MRI) or computed tomography angiography (CTA) scans may be required. Nevertheless, the studies performed with MRI[78]–[80] or CTA[81], [82] showed moderate sensitivity (60% - 92%) and specificity (74%) in detecting the plaque morphology.

Despite all the advantages of the current imaging modalities, the unmet need is a noninvasive approach, suitable for patient follow-up, that can distinguish between different plaque components [8], [34]. The wavelength specific optical absorption differences of distinct constituents of plaque might be advantageous to create contrast for imaging [83], [84]. In photoacoustics, the tissue is illuminated with short-pulsed laser light, and ultrasound is generated locally inside the tissue wherever the optical energy is absorbed. Since the scattering of acoustic waves is negligible for the soft tissue, imaging depth can reach up to 3 cm with large area illumination [85]. Combining the optical contrast with ultrasonic resolution and imaging depth, photoacoustic imaging (PAI) may outperform MRI and CTA for plaque assessment, with a comparably low cost and practical applicability similar to ultrasound.

In early studies, the applicability of intravascular photoacoustic (IVPA) imaging was investigated on phantoms and also on *ex vivo* rabbit arteries [86]. Results showed that the use of IVPA accompanied by intravascular ultrasound (IVUS) may provide morphological information in the assessment of atherosclerotic plaques. Moreover, spectroscopic IVPA provides an additional dimension of assessment depending on different constituents [87]. The capability of IVPA on detecting labeled macrophages as well as lipids embedded in polyvinyl alcohol (PVA) vessel phantoms was shown [72], [88], [89]. Successful differentiation of distinct lipid types have been reported on a PVA phantom [70] and on human coronary samples [69] using multi-spectral IVPA. The feasibility of intravascular photoacoustic tomography (IVPAT) for imaging lipid accumulation over time (25 weeks follow-up study) were shown in the aortas of rabbits which were on a high cholesterol diet [90]. Recently, an *ex vivo* study were reported to high speed imaging of lipid pools in carotid plaques using IVPA [91].

IVPA carries huge potential, especially for coronary plaques, where catheterization is inevitable. However, a catheter-based solution is less suitable for carotid plaque assessment before deciding on treatment. Furthermore, the superficial nature of the carotid artery (1 to 3 cm) makes it an attractive application for non-invasive PA studies. Therefore, an *in vivo* approach of noninvasive photoacoustics combined with ultrasound is regarded as a more accessible method. There are *in vivo* studies using a multi-spectral tomographic approach using a concave curved array around the neck [74] and using internal illumination via the pharynx [76] and external acquisition from the surface of the skin. Both studies presented promising phantom experiments; however, the specificity of the *in vivo* measurements was insufficient for drawing any conclusions.

Aforementioned PAI studies mostly focused on lipid detection and yet, the *in vivo* results are still sparse and often lack proper validation. In addition to the lipid in the plaque, intraplaque hemorrhages are fundamental indicators of plaque rupture [10]. Findings of medical studies in last decade led the interest towards intraplaque hemorrhage and vasa vasorum density as better risk predictors of plaque vulnerability [92]. Although there are few studies that aimed to detect intraplaque hemorrhages using MRI [79], [93] or CTA [94], it was disregarded by the previous photoacoustic studies.

The aim of this study is to demonstrate and validate the ability of PAI of carotid plaques, specifically targeting intraplaque hemorrhage, and neo-vascularization. To our knowledge, intraplaque hemorrhage was imaged for the first time in human tissue samples using PAI. The uncertainty of the optical energy reaching the plaque and the morphological complexity of the plaque were the two major challenges of the *in vivo* experiments. To identify the challenges of *in vivo* PAI of the carotid artery, the photoacoustic (PA) response of the human carotid plaque should be understood thoroughly. Therefore, an experimental setup, which allows complete rotation of the sample and creates a better quality 3D imaging using multi-angle spatial compounding, was designed to investigate the PA signals of the human carotid samples *ex vivo*. In this study, we used an integrated PA probe [95], and combined PA and plane-wave ultrasound (PUS) images to obtain 3D morphology of the samples. The wavelength of the probe was chosen to be 808 nm to obtain optimal absorption by the blood at the focal depth (~ 20 mm) of the ultrasound transducer. For valida-

tion, we compared the overlaid 3D PA and PUS images to the ground truth, i.e., the histology.

2.3 Methods

2.3.1 Sample Preparation and Experimental Setup

The endarterectomy samples were obtained from the Department of Vascular Surgery of the Catharina Hospital Eindhoven. All patients ($n = 7$) had ipsilateral neurological symptoms within the two weeks prior to the surgery; therefore, the samples are assumed to be vulnerable/ruptured plaques. The study was approved by the local ethics committee and all patients gave their informed consent. The carotid endarterectomy was performed using a method similar to the one described by Wijeyaratne et al. [96] to extract the plaques as intact as possible. If the plaque was fully intact, it was transferred to the laboratory in a phosphate buffered saline (PBS) solution. The plaque samples were flushed with PBS to remove blood clots from the outer surface of the media layer and inner surface of the intima. Washing out excess blood reduced possible clutter artifacts during photoacoustic imaging. After cleaning the

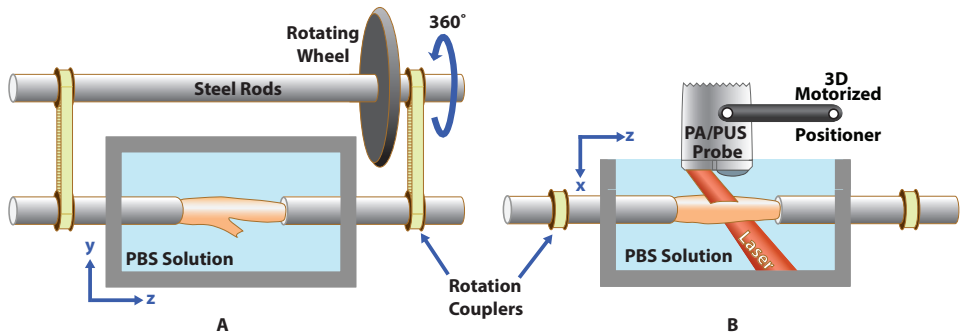


Figure 2.1: Illustration of the experimental setup from the top view (a) and from the side view (b). The sample was immersed into phosphate-buffered-saline (PBS) solution. The imaging probe was positioned in the cross-section of the sample for photoacoustic (PA) imaging.

plaque sample, plastic cannulas were attached to both ends of the carotid artery to enable rigid mounting of the sample in the PA/PUS imaging setup (Fig. 2.1). The

setup was designed to perform imaging during rigid rotation of vessel samples with 10° steps [97]. A motorized 3D stage (M-403.2DG, Physik Instrumente, Germany) was mounted to the setup to precisely adjust the position of the PAI probe.

2.3.2 Hand-held Photoacoustic Probe

For both PA and PUS imaging, a hand-held PA probe was used. This probe has an integrated diode laser system ($t_{pulse} = 130$ ns, $E_{pulse} = 1$ mJ, $\lambda = 808$ nm, QUANTEL, France, OSRAM, Germany, SILIOS, France) and a linear array ultrasound transducer (SL3323, $f_c = 7.5$ MHz, ESAOTE Europe, Maastricht, The Netherlands) for the acquisition. The pulse repetition rate (PRF) of the laser and the acquisition system is software limited to 2 kHz due to the laser safety regulations. The point-spread function (PSF) measurements of the system revealed that the system has 0.5 mm mean resolution in lateral direction and 0.28 mm in axial direction [95]. The detailed operation and specifications of the system and the hand-held probe (developed by the FULLPHASE Consortium) was described by Daoudi et al. [95].

2.3.3 Scanning Protocol

The probe was positioned in the transverse plane of the sample and the plaque was mechanically scanned along its longitudinal axis. PUS data were recorded at 10 Hz PRF during forward scanning and PA data were recorded at 100 Hz PRF during backward scanning. The mechanical scanning speed of the 3D stage was 1.0 mm/s; hence, the distances between two consecutive frames were $100\text{ }\mu\text{m}$ for PUS and $10\text{ }\mu\text{m}$ for PA acquisitions. A higher PRF was preferred in PA acquisition to allow more averaging in post-processing to increase the signal-to-noise ratio (SNR). After obtaining the data for both modalities, the sample was rotated by 10° and the measurements were repeated for all 36 angles.

2.3.4 Post Processing

During acquisition, the raw radio frequency (RF) data were acquired with a sampling rate of 50 MHz and stored. Data were processed offline using MATLAB 2014b (The MathWorks, Natick, MA, USA). The data were denoised with a series of digital filters, a DC blocking, a moving average ($N = 20$) for reducing the random electrical noise,

and a bandpass filter ($f_{low} = 0.8$ MHz $f_{high-PA} = 5.5$ MHz, $f_{high-PUS} = 15$ MHz) for suppressing the frequency content out of the acoustic bandwidth of the probe.

Beamformed RF data were reconstructed using the conventional delay-and-sum reconstruction method. After obtaining reconstructed ultrasound and photoacoustic acquisitions, data were rotated in reference to the position of the sample obtained at 0° . Next, data from all angles were spatially compounded into one 3D volume image to obtain a higher signal-to-noise ratio (SNR) and contrast-to-noise ratio. Spatial compounding provided geometry and morphology (mostly calcification) independent imaging performance, and lead a high resolution and contrast for the complete plaque. Finally, PA and PUS images were overlaid by assigning a transparency to PA image depending on its intensity value.

2.3.5 Histology Comparison

After PA/PUS imaging, five of seven samples (one sample was fractured during snap-freeze process and one sample was used for other purposes) were fixated in glycol (Tissue-Tek O.C.T., Sakura Finetek Europe, The Netherlands) solution and snap-frozen in liquid nitrogen. Each frozen sample was mounted to a cryotome (HM550, Thermo Scientific, USA) to obtain histology cross-sections. The samples were sliced with $10\ \mu\text{m}$ thickness. Since intraplaque hemorrhages were clearly identifiable in the white background of the frozen glycol solution, no additional staining needed to be performed. Instead, for each cross-sectional slice, an image was recorded by a digital camera. A total of approximately 2000 images were obtained from each plaque sample. This enabled a complete geometrical inspection, by comparing the slices to the PUS data.

Next, four samples that had a positive indication of hemorrhage in the PA images were selected for comparison with histology. The intraplaque hemorrhages were identified in the histology pictures, and five distinct regions in each plaque were selected for comparison. The corresponding cross-sectional PUS data were identified, based on the similarity in geometry. Next, the same regions with hemorrhage in histology were selected in the PA/PUS images and the corresponding PA intensities were compared to the PA data of the remaining vessel area.

2.4 Results

The 3D rendered volume images of PUS reveal the anatomy and shape of the plaque, clearly resembling the shape in the pictures of the plaques (Fig. 2.2), which were available for five cases. The pictures of the two sample were absent due to the fact that the intact geometry comparison was initially unintended and pictures were not taken. As expected, there is no contrast between the soft plaque content and the vessel wall. Conversely, the PA images solely provide the absorbing regions inside the plaque, i.e., the regions filled with blood (Fig. 2.2). The overlaid 3D volumes provide an overview of the samples, however, for a more elaborate comparison the transverse views need to be compared to the histology (see Fig. 2.3). In the histologic

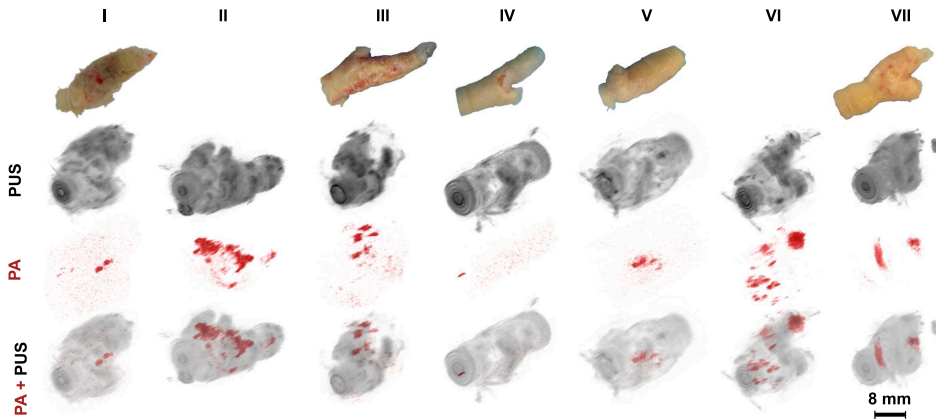


Figure 2.2: Imaging results for all plaque samples (I - VII). Pictures of the plaques are shown in the first row when available. The 3D plane wave ultrasound (PUS, second row), photoacoustic (PA, third row) and the overlaid PA/PUS images (bottom row) of the human carotid plaques are shown. Darker regions in the grayscale represent the higher echogenicity in pulse-echo ultrasound. The red regions show the PA signals, which correspond to a higher absorption of optical energy, i.e., higher concentration of blood content. Overlaid PA/PUS images with transparency indicates the possible intraplaque hemorrhage location in these atherosclerotic plaque samples.

cross-sections, the yellow regions are the vessel wall, whereas the dark red areas are hemorrhages. The darker (brownish-yellow) color represents the calcified area in the plaque and the light yellow area is in this case the lipid pool, which is not really distinguishable from the wall in these images (see Fig. 2.3). However, since targeting

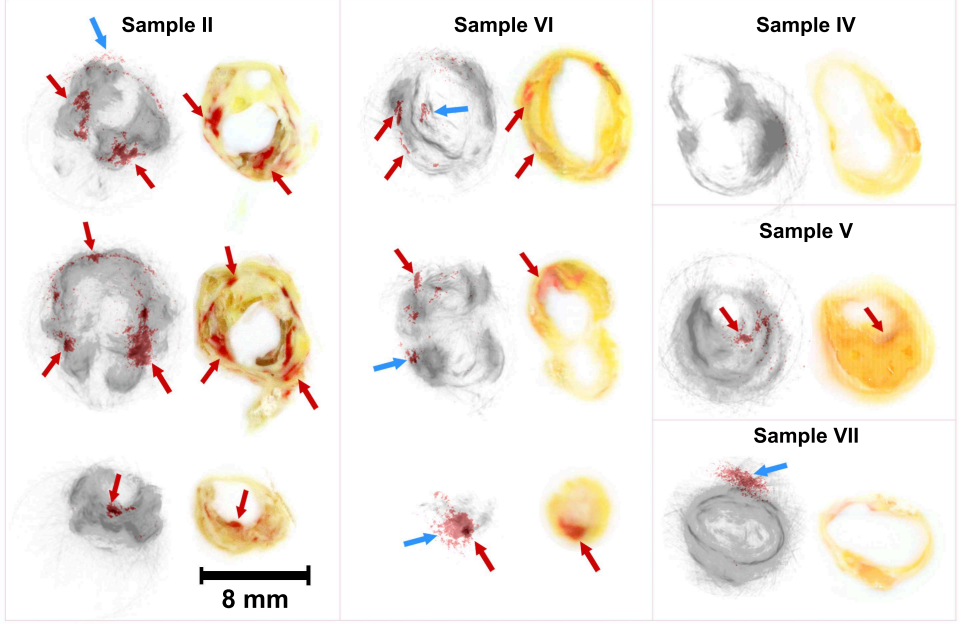


Figure 2.3: Pictures of histology sections and the corresponding cross-sections in overlaid photoacoustic (PA) - plane wave ultrasound (PUS) images of five plaques. Gray color represents the ultrasound signals and overlaid red colors represent the PA signals. The red arrows indicate the blood content inside the plaques in the histology pictures and the corresponding PA signals in overlaid PA/PUS images. Blue arrows indicate the clutter artifacts and regions with overestimation of the PA signals.

lipid was not an aim of this study, no additional histological analysis on lipid content was performed.

Qualitative comparison of overlaid PA/PUS images to histology reveals one to one correspondence between the two (see the red arrows in Fig. 2.3). These images confirm that the high signal intensity in PA images indicates regions with high blood content, most likely intraplaque hemorrhage. There are additional regions located outside of the vessel with high intensity signals (see the blue arrows in Fig. 2.3) for some of the cross-sections. Those signals were identified as clutter artifacts and were recognized based on the geometry provided by PUS images. The quantification of the severity of the clutter was not performed, and in the scope of this study, the

clutter artifacts were assumed not to deteriorate the actual PA signals significantly.

The quantitative comparison of the segmented regions with hemorrhage vs. the remainder of the vessel area supports the objective of this study. The PA signal intensities in the segmented area were significantly higher (one way ANOVA, $p < 0.001$), whereas the PUS gray values were not (Fig. 2.4). An additional correlation analysis between US and PA images was performed to show the independence of the two modalities. There was no correlation in the hemorrhage segments ($R^2 = 7.01 \pm 8.05\%$) and the rest of the vessel segments ($R^2 = 2.10 \pm 4.22\%$) for all the selected frames in the histology comparison.

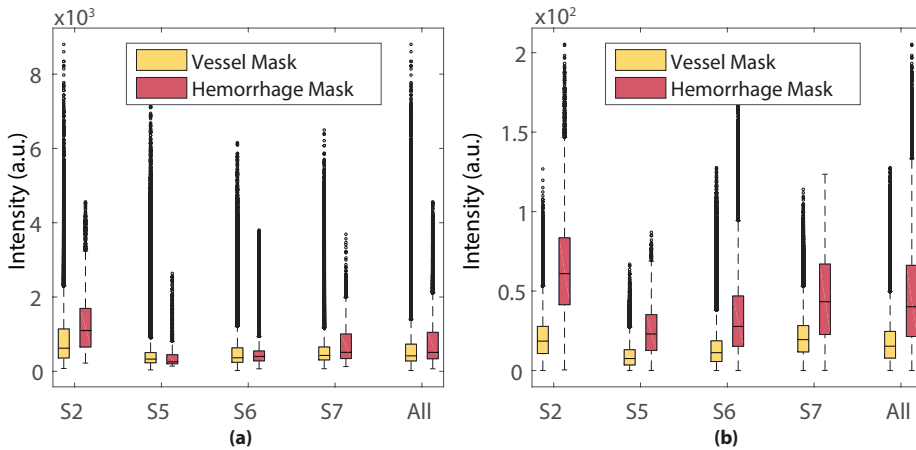


Figure 2.4: Statistical comparison of the intensities in the segmented regions of hemorrhages: (a) boxplots of the gray values of ultrasound images in regions with hemorrhage (red) and those found in the surrounding tissue region (yellow), for samples II, V, VI and VII; (b) boxplots of the photoacoustic signal measured in hemorrhage segments (red) vs. those detected in the surrounding tissue (yellow). The black circles are data points that are considered outliers of the statistical distribution

2.5 Discussion

In this study, we have demonstrated the feasibility of PAI to locate intraplaque hemorrhages (any intraplaque blood pools) in atherosclerotic carotid plaques as a first step towards noninvasive plaque characterization. We used a hand-held photoa-

coustic probe with integrated diode laser and a portable medical ultrasound system. Signals corresponding to blood-filled regions, which can be extensions of the vasculature in the plaque, intraplaque hemorrhage, or the result of trauma inflicted on the medial vascularization, were found in the PA images with high contrast with respect to the wall, whereas these regions were not distinguishable in the PUS images. The detection of intraplaque hemorrhage in carotid plaques is the novelty of this study and promising towards *in vivo* preclinical studies regarding carotid plaque vulnerability assessment.

The histologic cross-sections show one to one correspondence with the overlaid photoacoustic and ultrasound images. While ultrasound images reveal the shape of the vessel, photoacoustic images show where the intraplaque hemorrhage is located (Fig. 2.2). The lack of PA signals in the rest of the plaque components such as lipid, calcification, and vessel wall proves that the optical absorption of those constituents at 808 nm illumination is not sufficient to create detectable photoacoustic signals. Moreover, the histology based manual segmentation validated that the PA intensities were significantly higher in the segmented regions.

The overlaid PA images contain some clutter artifacts (Fig. 2.2) due to optical energy deposition outside the imaging plane or multiple reflections from calcifications (highly echogenic) in the vicinity of the blood content. By adopting recently developed clutter reduction methods, we may benefit from the pulsation of the carotid artery *in vivo* to reduce the clutter [98]. Furthermore, a priori ultrasound data can be used to reduce the reflection clutter [99].

The PA/PUS images were obtained in a controlled setting using a tomographic approach by rotating the samples, which provides a complete cross-sectional view. This approach also overcomes the limited field of view in the presence of excessive calcifications. Obviously, this is not a method designed for, or feasible in, *in vivo* applications, but purely for preclinical validation of the PA/PUS techniques. The tomographic approach in this study could be partially translated to *in vivo* scanning via the development of novel, optimal multi-angle, *in vivo* imaging methods.

The use of integrated diode laser lowers the available energy of the imaging system; however the limiting factor for the maximum permeable energy (MPE) of the laser

is the medical laser device standards (IEC/EN 60601-2-22 and IEC 60825-1) considering its future clinical use. The illumination scheme was optimized for highest optical flux at the focal depth of the ultrasound transducer (~ 20 mm). In the next prototypes, energy could be increased within the clinical safety limits. Nevertheless, in the scope of this study, the 1 mJ pulse energy was sufficient to provide the images of plaque samples in the *ex vivo* conditions.

The *ex vivo* imaging protocol developed in this study will contribute much needed, ground truth knowledge to overcome *in vivo* problems in PA imaging of the carotid plaques. The imaging depth of the PA system used is in the range of the anatomical depth of carotid arteries. However, the imaging system is likely not to achieve similar performances for patients with a high body-mass index. For instance, the peripheral vessels that are located between the skin and carotid artery, and the presence of luminal blood, will reduce the optical power that reaches the plaque. However, the multi-angle spatial compounding compensates the signal loss due to luminal blood absorption. Despite the *in vivo* challenges, the experimental method used in this study can provide complementary information to compare the pre-operative *in vivo* images to the post-operative, *ex vivo* images of both PA and PUS. Handling those challenges within laser safety limits will require to develop novel techniques based on the ground truth knowledge. Therefore, the ability to detect intraplaque hemorrhages while keeping the plaque intact will enable further research on increasing the signal-noise-ratio of the system in the presence of surrounding tissue and aforementioned *in vivo* conditions. Similarly, the presence of luminal blood besides the intraplaque blood will require a technique to distinguish between the two. Using the high temporal resolution of PA/PUS, and the fact that luminal blood will move with a high speed whereas thrombus will not, may provide a solution to encounter this problem. Moreover, the absorption spectrum of thrombus slightly deviates from hemoglobin, which may be beneficial for PA spectroscopic techniques using multiple wavelengths to distinguish between fresh blood and thrombus. Such a multi-spectral approach can also be used to reveal additional morphological features of the plaques.

2.6 Conclusion

In summary, PA and PUS imaging of intraplaque hemorrhages in human carotid plaques were performed as a first step towards *in vivo* imaging. A fully integrated PA probe was used externally, and spatial compounding of acquisitions from different angular positions were performed to obtain full 3D images of the samples with better image quality. Since intraplaque hemorrhage is considered to be one of the indicators of plaque vulnerability, this study showed that PAI can be used in vulnerability assessment of atherosclerotic carotid plaques. Future work, at higher penetration depths, will demonstrate its clinical merit.

To obtain the complete morphology (lipid pool, fibrous cap, and intraplaque hemorrhage) of a plaque, multi-spectral PA is necessary. We performed the measurements with single wavelength illumination and in isolated conditions to investigate the possibility of PAI for intraplaque hemorrhage detection. In future studies, the PA imaging performance will be further investigated in the presence of luminal blood, the pulsation of the vessel [100] and surrounding tissue. Incrementally approaching to more realistic conditions will ease the development of novel solutions to the challenges in PA imaging *in vivo*. Eventually, the ability to differentiate between rupture-prone and stable plaques will contribute to clinical decision making in vascular surgery. A reduction in over-treatment of the stable plaques will lower the burden on the patient, and additionally will reduce the risks and costs involved. Furthermore, prevention of stroke or other complications, by early detection of unstable plaques, will reduce the mortality and morbidity rates most importantly, increase the quality of life in aging societies.

2.7 Acknowledgments

This study is funded by the European Community's Seventh Framework Programme (FP7/2007-2013) under grant agreement n° 318067.

Chapter 3

Investigation on the effect of spatial compounding on photoacoustic images of carotid plaques in the *in vivo* available rotational range

The content of this chapter is based on M. U. Arabul, H. M. Heres, M. C. M. Rutten, M. R. H. M. van Sambeek, F. N. van de Vosse, and R. G. P. Lopata, "Investigation on the Effect of Spatial Compounding on Photoacoustic Images of Carotid Plaques in the *in vivo* Available Rotational Range," IEEE Trans. Ultrason. Ferroelectr. Freq. Control, vol. 65, no. 3, pp. 440–447, Mar. 2018.

3.1 Abstract

Photoacoustic imaging (PA) is a promising imaging modality due to its high optical specificity. However, the low signal-to-noise ratio (SNR) and contrast-to-noise ratio (CNR) of *in vivo* PA images are major challenges that prevent PA imaging from finding its place in clinics. This study investigates the merit of spatial compounding of PA images in arterial phantoms and the achievable improvements of SNR when *in vivo* conditions are mimicked. The analysis of the compounding technique was performed on a polyvinyl alcohol vessel phantom with black threads embedded in its wall. The *in vivo* conditions were mimicked by limiting the rotation range in $\pm 30^\circ$, adding turbid surrounding medium, and filling the lumen with porcine blood. Finally, the performance of the technique was evaluated in *ex vivo* human carotid plaque samples. Results showed that spatial compounding elevates the SNR by 5 to 10 dB and CNR by 1 to 5, depending on the location of the absorbers. This study elucidates prospective *in vivo* PA characterization of carotid plaques by proposing a method to enhance PA image quality.

3.2 Introduction

Recent developments in photo-acoustic imaging (PAI) have demonstrated promising results in various studies targeting cardiovascular diseases [69], [76], [87], [101]. Combining the anatomical information obtained from ultrasound with the tissue composition obtained from PAI, the complete morphology of atherosclerotic plaques can be revealed. This morphological information might be used to assess the content of the plaque, which is one of the markers for rupture risk of a plaque and a subsequent stroke [7], [34].

In previous studies, PAI was used for *ex vivo* imaging of atherosclerotic plaques in coronaries [69] and carotid arteries [101], while steps toward non-invasive imaging of carotid arteries were being taken [74], [76]. For plaques in coronary arteries, intra-vascular imaging using PA can be beneficial. Previously, a few studies have shown the feasibility of PA in the detection of lipid pools in coronary arteries [70], [91], [102]. However, due to the superficial anatomy of carotid arteries, non-invasive PAI is more suitable for carotid plaque assessment. Nevertheless, the attempts at *in*

in vivo PA imaging of carotid arteries are sparse [74], [76]. The typical challenge of *in vivo* PAI is the low signal-to-noise ratio (SNR) due to optical and acoustic energy losses in the tissue. Moreover, the complexity of the plaque composition and the inter-subject variability in tissue properties, such as different calcification densities, impose fundamental limitations on *in vivo* PAI of atherosclerosis, due to the acoustic scattering of PA waves. Therefore, the complexity of the problem increases without *a priori* knowledge of the exact content of the plaque. Additional complexity is found *in vivo* due to the absorption by luminal blood and the pulsation of the arterial wall caused by the varying blood pressure.

To eliminate the causes of artifacts *in vivo* such as pulsation, luminal blood, and surrounding scattering medium, we previously performed an *ex vivo* feasibility study [101]. Isolating the plaques from its surroundings simplified the identification of the tissue-of-interest and showed the feasibility of PAI in the detection of intraplaque hemorrhages. For proof of concept, we investigated human plaque samples *ex vivo* and imaged each sample from multiple angles for a full 360° rotation. This range of rotation is not available *in vivo* and was intended for research and validation purposes only. However, the increase in both SNR and CNR after compounding was significant and would certainly be desirable *in vivo*. Compounding of multi-angle PA data for a limited range of angles could partially recreate this effect.

Spatial compounding of multiple images has been extensively used in plane-wave ultrasound imaging [103]–[105] to elevate image resolution or to estimate the speed of sound differences in tissue [106]. However, until recently, the effect of spatial compounding in PA has not been characterized for different acquisition geometries. Recently, the necessity of a multi-angle photoacoustic acquisition has been studied for the accurate reconstruction of absorber distribution [107]. Additionally, spatial compounding of PA images, which are acquired in different imaging planes by tilting the probe around its elevational axis, was investigated to obtain better contrast and resolution in PA images [108]. In their study, Kang et al. used a fixed laser illumination and a variable acquisition geometry to reconstruct the spatial distribution of the absorbers.

In this study, we investigated the effects of multi-angle spatial compounding on PA images that are acquired from different rotational positions with respect to the axis

of the vessel sample. We aimed to investigate the merit of PA compounding for non-invasive *in vivo* plaque imaging. We used an integrated PA probe [95]; therefore, both the illumination geometry and the ultrasonic acquisition geometry were altered together during rotation. Since a full rotation of the sample as performed in *ex vivo* experiments [109] is not possible *in vivo*, the effect of compounding was analyzed. The effects of angular spatial compounding were investigated and quantified in polyvinyl alcohol (PVA) phantoms for *in vivo* mimicking conditions, such as a limited range of rotation, turbid surrounding medium and the presence of blood in the lumen of the samples. Finally, the proof of principle was shown in available *ex vivo* data of human carotid plaques ($n = 4$). A quantitative analysis was performed by comparing SNR and CNR of PA images for various cases.

3.3 Materials and Methods

3.3.1 Phantoms and Plaque Samples

A black thread-embedded polyvinyl alcohol (PVA) phantom was designed to characterize the performance of the spatial compounding technique to detect plaque hemorrhages in the vessel wall. The PVA gel was prepared by dissolving 15 wt% crystal PVA (Mowiol 28-99, Sigma-Aldrich, Zwijndrecht, The Netherlands) in demineralized water at 90°. Thereafter, 1 wt% Orgasol (ELF Atochem, Paris, France) was added to the gel for acoustic scattering. Next, the PVA gel was molded in a cylindrical mold, where black threads were attached along the height of the cylinder (see Figure 3.1c). Finally, molded PVA was frozen and thawed for four consecutive cycles (16 hours freeze and 8 hours thaw duration for 1 cycle) to approach stiffness of a generic vessel [100].

Next, the performance of spatial compounding were investigated on existing *ex vivo* atherosclerotic plaque data [101]. The samples were obtained from the Department of Vascular Surgery of the Catharina Hospital Eindhoven. Informed consent was obtained from the patients in a study approved by the local ethics committee. Analysis was performed on 4 plaque samples having intraplaque hemorrhages, which provided detectable PA signals. A total of 20 distinct cross-sections were included for the compounding analysis.

3.3.2 Experiment Setup and Imaging Device

For each specimen, imaging was performed in a custom-designed immersion chamber (see Figure 3.1). The setup consisted of a water tank with two steel pipes attached to its sides. The steel pipes were coupled via a gear system and a secondary steel rod, which allowed a synchronized rotation of both ends of the sample. A motorized rotation stage was concentrically mounted to the secondary rod. Additionally, a three-dimensional (3-D) linear stage (M-403.2DG, Physik Instrumente, Germany) was attached to the setup to control the position of the imaging probe with respect to the sample. Both the Cartesian position of the probe and the angular position of the specimen were controlled by a PC using LabVIEW software (National Instruments, Austin, Texas, USA). The PA imaging probe consisted of a diode laser

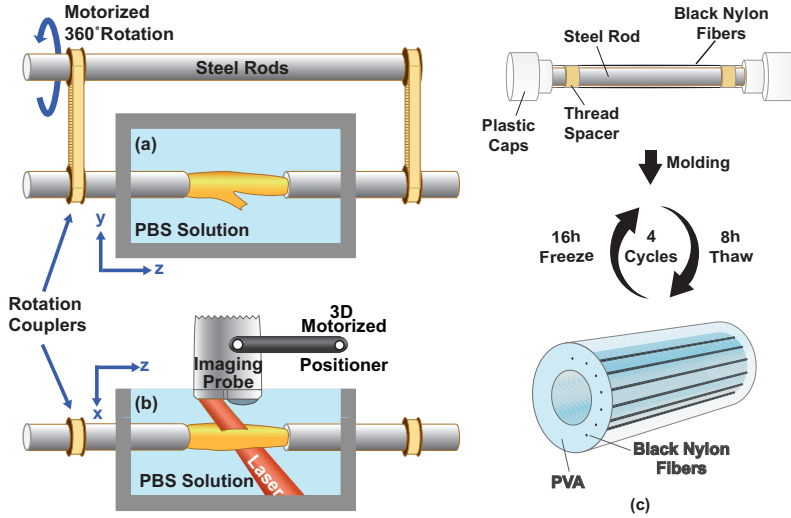


Figure 3.1: Illustration of the experimental setup from (a) the top view and (b) the side view; (c) the mold and the polyvinyl alcohol (PVA) phantom. The sample was immersed in a phosphate-buffered-saline (PBS) solution. The imaging probe was positioned in the cross-section of the sample for photoacoustic (PA) imaging and translated along the longitudinal axis of the vessel.

(QUANTEL, Paris, France) with a wavelength of 808 nm, a pulse duration of 130 ns, and a pulse energy of 1 mJ. The acoustic signals were acquired by the linear array transducer (SL3323, ESAOTE, Maastricht, The Netherlands) that was integrated into the PA probe. For data acquisition, the PA probe was attached to an ultrasound

scanner (MyLabOne, ESAOTE, The Netherlands), and the raw data were digitized at a sample frequency of 50 MHz and transferred to the PC via a USB connection.

3.3.3 Experimental Procedure

Phantom Experiments

Three different sets of phantom experiments (PE1-PE3) were performed as seen Table 3.1. During all the experiments, the PA probe was positioned in the transverse cross-section of the vessel. A total of 500 PA frames were acquired with a pulse repetition frequency (PRF) of 100 Hz. Next, the sample was rotated by 10° and acquisition was repeated for 36 different angular positions. The same acquisition protocol was repeated for plane-wave ultrasound. For each cross-section, 10 frames were acquired with a PRF of 50 Hz. In the first set of experiments (PE1), the volt-

Table 3.1: The experiments and corresponding parameters

Experiment Name	Surrounding Medium	Lumen	Depth of Sample Center (mm)	Laser Pulse Energy (μJ)
PE1	Demi-water	Demi-water	8.85	84 - 1045
PE2	Intralipid + India Ink Solution	Intralipid + India Ink Solution	8.45 - 18.85	1045
PE3	Intralipid + India Ink Solution	Porcine Blood	8.25 and 15.50	1045
ExPLQ	PBS	PBS	~ 8.5	1045

age of the high voltage capacitors of the laser driver circuit was varied from 30V to 100V to tune the optical output energy of the laser diode between $84 \mu\text{J}$ to $1045 \mu\text{J}$. Thereby, a lower optical absorption was mimicked, which was validated by the linear change in the intensity of PA signals (data are not shown). During PE1, the sample was immersed in water at 8.85 mm depth.

In the second set of experiments (PE2), the immersion medium was changed to a tissue mimicking liquid obtained by mixing 1 V/V % Intralipid (20%, Fresenius Kabi BV, Zeist, The Netherlands, Batch No: 10II5853) [110] and 0.001% of Indian Ink (Talens, Apeldoorn, The Netherlands) [36], [111] in demineralized water. The resulting optical properties represent a generic soft tissue ($\mu_s = 10 \text{ cm}^{-1}$ and $\mu_a = 0.5 \text{ cm}^{-1}$). Additionally, the depth of the sample was increased from 8.45 mm to 18.85 mm in four steps, to investigate performance of compounding with increasing tissue depth.

In the final set of experiments (PE3), the effect of luminal blood was investigated by replacing the medium in the lumen by porcine blood obtained from local slaughterhouse. The measurements were performed at two different depths ($z = 8.25 \text{ mm}$, 15.20 mm). Due to the manual adjustments during experiments, the initial position of the samples deviated slightly between the experiments. However, the effects of the deviation in depth were eliminated by considering only the relative changes in each experiment.

***Ex vivo* Human Plaques Experiments**

The *ex vivo* measurements of human plaque samples (ExPLQ) were explained previously, in detail [101]. The samples were immersed in phosphate-buffered-saline (PBS) solution at approximately 8.5 mm depth, and at a laser pulse energy of $1045 \mu\text{J}$. Differently, the probe position was mechanically scanned along the z axis (see Figure 3.1a) during acquisition of PA data. Therefore, temporal averaging was kept at 20 frames to prevent artifacts due to motion. Finally, the measurements were repeated for 36 angles.

3.3.4 Compounding Method

Data were filtered with a DC-blocking filter by subtracting the mean value of each channel. Afterwards, time frames were averaged into a single frame depending on the averaging window size (see Figure 3.3). Next, different band-pass filters were applied to each modality (PA vs. US) due to the spectral differences between the modalities [101]. While the pulse-echo signals were in the bandwidth of the transducer ($f_c = 7.5 \text{ MHz}$), the main frequency content of the PA signals was in the range

of 0.8 - 5 MHz.

The images were reconstructed using k-space reconstruction [47] and radio-frequency (RF) data were obtained prior to envelope detection. The spatial sampling in the axial direction ($c/f_s = 30.8 \mu\text{m}$) was 8 times higher than the lateral spatial sampling ($d_{pitch} = 245 \mu\text{m}$). Therefore, images were mapped to a $50 \mu\text{m}$ equispaced grid using bi-cubic interpolation. Next, the images acquired at different angular positions were rotated back to the reference position of the sample at 0° . Consequently, a multi-angle acquisition, where the sample is fixed and the probe rotates, was mimicked. Finally, pixel values in the rotated images were summed and the envelope of the final image was detected, resulting in the final compounded images.

3.3.5 Image Quantification

The contribution of spatial compounding to the image quality was quantified by comparing the SNR and CNR of the absorbers in the images. In the data of the PVA phantom, a circular region of interest (ROI) was manually selected around each thread to obtain the signal power locally. Next, the region without black threads in the vessel wall was considered as background (see the dashed lines in Figure 3.2a).

In the data of the *ex vivo* carotid plaque samples, the segmentation was performed on the compounded ultrasound images based on the geometric similarity of the cross-sectional vessel contours in the ultrasound image and the histology pictures [101]. The hemorrhage regions were identified in the histology pictures, and the corresponding areas in the ultrasound image were segmented as the signal ROI. However, in order to improve the registration of the US and PA data, ROIs were manually adjusted by enlarging and translating the ROI.

Lastly, the SNR was calculated as,

$$SNR = 20 \log_{10} \left(\frac{S_{rms}}{N_{rms}} \right),$$

and the CNR was calculated as,

$$CNR = \frac{S_{rms} - N_{rms}}{N_{rms}},$$

where S_{rms} represents the root-mean-square (RMS) of the signal ROI and N_{rms} represents the RMS value of the background ROI.

Quantitative analysis was performed for the compounded data for two cases: a) complete rotation and b) the *in vivo* available rotation range (angles between -30 to 30°). Since spatial compounding could be considered a form of averaging in space domain, the total number of frames was kept constant for temporal averaging and spatial compounding to make a fair comparison between the two. Finally, the SNR and CNR values of each thread were analyzed separately to assess the effect of the absorber location.

3.4 Results

3.4.1 PVA Phantom Experiments

A qualitative representation of the effect of spatial compounding is demonstrated in Figure 3.2. The illustration in Figure 3.2a shows the geometry, orientation of the threads, and the segmented ROIs for the threads. The single frame plane-wave ultrasound image of the phantom (Figure 3.2b) revealed the geometry of the phantom with blurry edges at the sides. The black threads were not clearly visible in a single frame ultrasound image. However, spatial compounding increased the resolution and the contrast of the ultrasound images as expected (Figure 3.2c). Since the focus of this study is the improvement in PA image quality, no further quantitative analysis was performed on the US images.

The signal levels in each single-shot PA image (Figure 3.2d) were insufficient to obtain a clear contrast at the absorber locations. Therefore, multiple acquisitions were temporally averaged to increase the signal quality of PA images (Figure 3.2e). Spatial compounding of averaged frames further increased image quality with higher resolution, contrast, and signal levels (Figure 3.2e). The separation and the size of the threads were not perfectly uniform, which affected the PA signals of each thread as seen in the compounded PA image (Figure 3.2f). Figure 3.3 shows that increasing the number of frames averaged improves the SNR of the PA images of the PVA phantom; however, the rate of improvement decreases. The SNR of the averaged

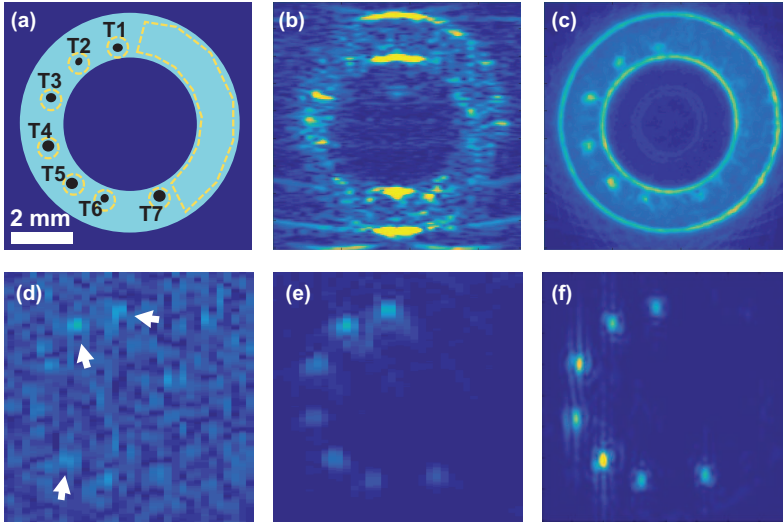


Figure 3.2: (a) Illustration of the phantom and embedded black threads labeled from T1 to T7, (b) conventional single-frame plane-wave ultrasound image of the phantom, (c) The resultant ultrasound image of PVA phantom after spatial compounding of all 36 angular positions, (d) Single frame photoacoustic (PA) image, (e) Photoacoustic image of the phantom after 500 frames temporal averaging, (f) The resultant PA image of PVA phantom after spatial compounding over 36 angular positions.

images follows the general shape of $20\log_{10}\sqrt{N}$ as the theory of temporal averaging of random signals states [112].

In Figures 3.3b to 3.3d, the effect of temporal averaging on the SNR of the PA images is shown (dashed lines) for increasing number of averaged frames ($N = 70, 210, 350, 490$ frames). Similarly, the effect of spatial compounding on SNR is shown (solid lines) for increasing range of rotation ($0, \pm 10, \pm 20, \pm 30$) and equivalent total number of frames. The SNR improvement of spatial compounding in the limited range of rotation outperforms temporal averaging by 4 dB in the case of 1 mJ optical illumination (see Figure 3.3d). The initial SNR values of the compounded images should be sufficiently high for compounding to be effective. As seen in Figure 3.3, if the SNR of initially generated PA signals are lower than a certain threshold (~ 2 dB), temporal averaging performed better than spatial compounding. The results of PE2 showed that changing the surrounding medium from water to tissue mimicking fluid decreased the SNR by 3 dB and CNR by 2, see Figure 3.4a. Furthermore, the

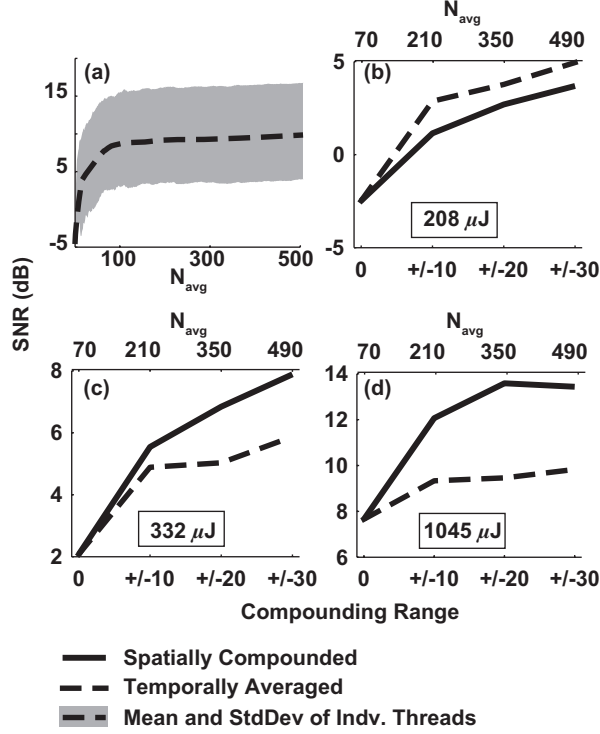


Figure 3.3: (a) The dashed line is the mean of the SNRs of individual threads and the shaded area shows the limits of the maximum and minimum SNR values of each thread in PA images after temporal averaging. Plots (b), (c), and (d) show a comparison of the effect of temporal averaging ($N_{avg} = 70, 210, 350, 490$) and spatial compounding ($N_{avg} = 70$, $\theta_{Range} = 0, \pm 10, \pm 20, \pm 30$) for an equal total number of frames on the SNR of the PA images. The PA images of the PVA phantom were obtained for optical pulse energies of (b) 208 μJ , (c) 332 μJ , and (d) 1045 μJ .

SNR of a single position PA image dropped by 11 dB at approximately 2 cm imaging depth. However, compounding the 7 angular positions between -30 and +30 degrees increased the SNR by 7 dB again.

Focusing on the individual absorbers for the lowest SNR case (I4), Figures 3.4b and 3.4c show that spatial compounding in the *in vivo* available range (± 30 degrees) increases the mean SNR by 6.5 dB and the CNR by 3. The results of the final set of experiments with the PVA phantom (PE3) shows that the presence of blood in the lumen decreases the SNR by 2.5 dB; however, the contribution of spatial compound-

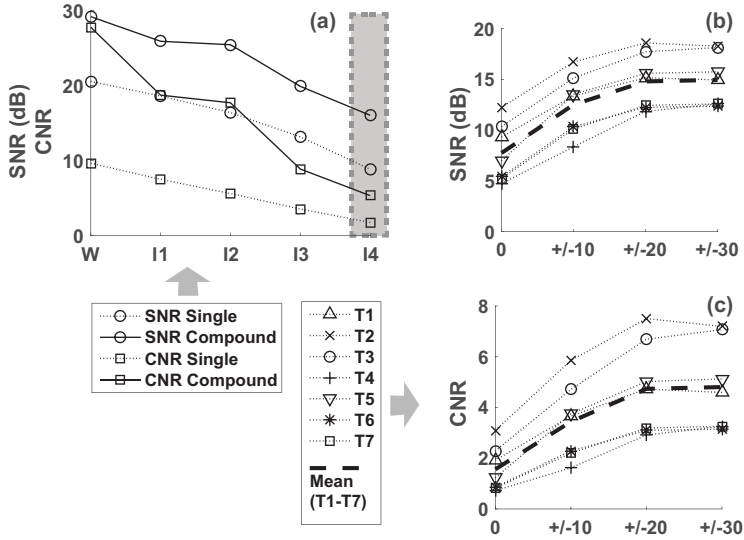


Figure 3.4: (a) SNR and CNR of the PA images of the PVA phantom in water (W, at 8.45 mm), and in Intralipid-Ink mixture (I1 at 8.45 mm, I2 at 11.60 mm, I3 at 15.75 mm, I4 at 18.85 mm). The dotted lines show the values of the single position acquisition and solid lines show the values of compounded images in the range of ± 30 degrees. The SNR and CNR values of individual threads for the case of I4 was demonstrated in (b) and (c), respectively. The dashed lines show the mean value of individual threads.

ing is larger (7.5 dB) compared to the loss in signal due to the presence of blood in the lumen. In Figure 3.6, resultant PA images were presented for a more qualitative illustration of the effect of spatial compounding for the extreme cases of PE2 (I4) and PE3 (B2). In the presence of a turbid surrounding medium, spatial compounding increased the quality of the images while the threads initially had a poor contrast (see Figure 3.6a and 3.6b). In the case of a lumen filled with blood, spatial compounding elevated the SNR of the distal threads (T6 and T7) by ~ 8 dB and the CNR by ~ 1 (see solid arrows in Figure 3.6). Moreover, the lumen border becomes clearer after spatial compounding in the limited range (see dashed arrows in Figure 3.6).

3.4.2 *Ex vivo* Plaque Samples

In Figure 3.7, two different cross-sections of a plaque are selected to illustrate the image qualities for single angle acquisition, limited angle compounding, and complete

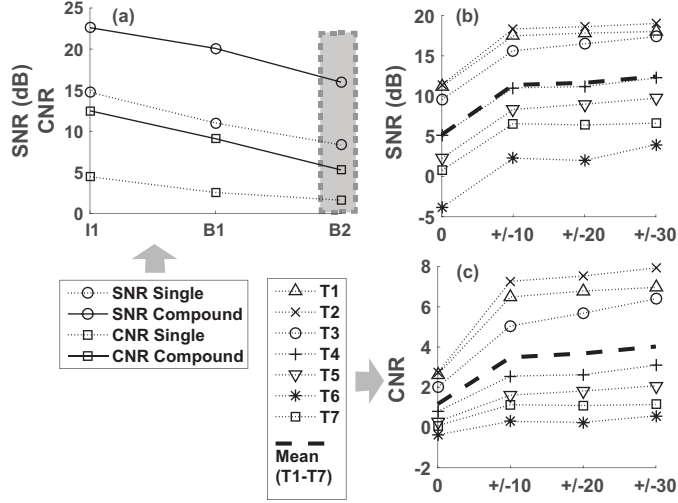


Figure 3.5: (a) SNR and CNR of the PA images of the PVA phantom where the surrounding and the lumen are both filled with Intralipid-Ink mixture (I1, at 8.25 mm), and with the lumen porcine blood (B1 at 8.25 mm, B2 at 15.55 mm). The dotted lines show the values of the single position acquisition and the solid lines show the values of the compounded images in the range of ± 30 degrees. The SNR and CNR values of the individual threads for the case of B2 was demonstrated in (b) and (c), respectively. The dashed lines show the mean value of individual threads.

rotational compounding. In the first cross-section (Figure 3.7a-c), the dominant absorber was located proximal to the PA probe at the initial position. Therefore, the SNR of the image was highest at zero position (16.2 dB). Compounding of all the rotational positions increased the background noise and eventually decreased the SNR by 6 dB.

In the second cross-section (Figures 3.7d-f), the SNR of the absorber that is proximal to the imaging probe dropped from 13.3 dB to 10.6 dB for limited range compounding, and to 11.5 dB for complete rotational compounding. However, the benefit of spatial compounding was significant for the absorber distal to the probe. The SNR of the absorber increased drastically from -2.4 dB to 12.7 dB. Additionally, the CNR values of the PA images revealed similar behavior with the SNR values. The CNR of the first cross-section (Figure 3.7a-c) dropped from 5.4 to 2.8 and 2.3 respectively for the limited range compounding and full range compounding cases. However, the CNR of the distal absorber in the second cross-section (Figure 3.7d-f) raised from -

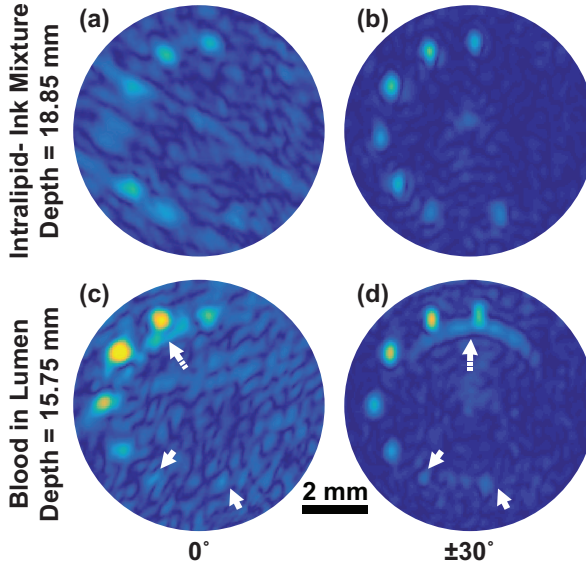


Figure 3.6: Single frame (a and c) and compounded (b and d) in the range of $\pm 30^\circ$ PA images of the PVA phantom in the tissue-mimicking liquid (Intralipid-Ink mixture) at 18.85 mm central depth (a and b), and with the presence of blood in lumen at 15.75 mm central depth (c and d).

0.2 to 3.3. The relative changes of SNR and CNR of individual absorber regions in all 20 cross-sections were represented in Figure 3.8. Spatial compounding for the full rotational range elevated the mean SNR by ~ 7 dB and CNR by 1. However, for the limited rotational range case, improvements were significant only for the distal absorbers, which was indicated by the outliers in the box-plot.

3.5 Discussion

In this study, we investigated the effects of multi-angle spatial compounding on the quality of PA images of a PVA vessel phantom. We demonstrated that spatial compounding of the acquisitions from different angular positions improved the quality of PA images in terms of higher SNR and CNR. The improvements introduced by spatial compounding are due to an increase in PA signal intensities of absorbers which were achieved by the rise of optical power at the far absorbers location. Therefore, spatial compounding outperforms temporal averaging, which increases the

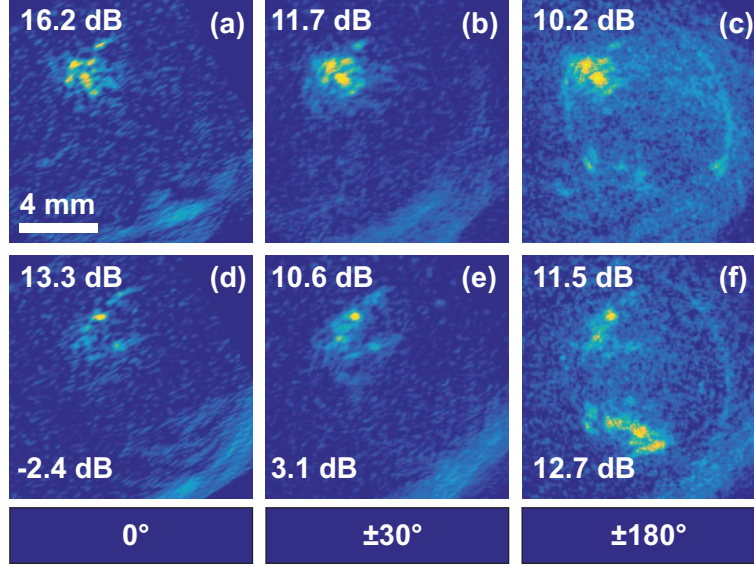


Figure 3.7: Single frame (a and d), compounded (b and e) in the range of $\pm 30^\circ$ and compounded (c and f) PA images in the range of $\pm 180^\circ$ of human plaque samples. The rows represent two different cross-sections of a plaque.

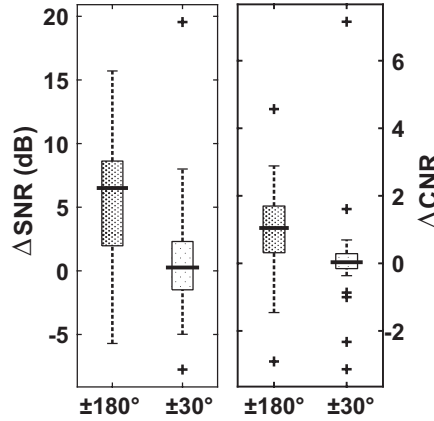


Figure 3.8: Relative changes in SNR and CNR of compounded images with respect to single angle acquisition.

SNR by suppressing the variance of the white-noise.

We further investigated the performance of compounding for *in vivo* mimicking conditions, such as turbid surrounding medium, the presence of blood in the lumen of the vessel, and limited angular rotation. The results illustrated that spatial compounding yielded a significant improvement for the limited range of rotation. The addition of tissue mimicking fluid to the surroundings, and porcine blood to the lumen of the phantom, reduced the SNR and CNR of the images. Especially the distal absorbers (T6 and T7) disappeared in the presence of luminal blood. However, spatial compounding, even for the limited *in vivo* range, compensated these losses, thereby improving the image quality.

Finally, we performed a reanalysis of previously published human plaque data to quantify the effect of spatial compounding on *ex vivo* PA images. The SNR improvement after spatial compounding of PA images in the range of $\pm 30^\circ$ was as high as 20 dB for distal absorbers; however, SNR change was observed to be negative for proximal absorbers. This is mostly due to inhomogeneities such as calcifications, lipid pools, and intraplaque hemorrhages in human plaque samples. Therefore, the image quality improvement of spatial compounding is highly dependent on the location of the absorber.

Since all the plaque samples were dissected during the histological examination, it was not possible to repeat measurements with different conditions as in the PVA phantom. However, relative losses in the SNR values can be assumed to apply to human plaque samples. Adding surrounding medium, increasing the depth, and adding luminal blood would potentially decrease the SNR of the plaque samples by approximately 12 dB. This shows that 2 cm depth will be the limit of this technique when applied *in vivo*. The authors acknowledge that in patients with high body-mass index this depth will probably not be sufficient. Moreover, the available data allowed for temporal averaging with 20 frames, and as Figure 3.3a shows, acquiring a higher number of frames could have drastically increased the SNR of plaque images.

For the future *in vivo* studies using spatial compounding, a method for registration of the data should be developed for hand-held use. Moreover, this study elucidates the future experimental designs by stating the need for a faster data acquisition that allows sufficiently high temporal averaging prior to spatial compounding. Finally, the presence of multi-layer surrounding tissue, such as skin, subcutaneous fat and

muscle might have more significant effects on optical losses than homogeneous tissue mimicking fluid used in this study. Therefore, a higher optical pulse energy within the safety limits may be necessary for *in vivo* experiments.

3.6 Conclusion

We showed that the quality of PA images in terms of SNR and CNR can be improved by compounding PA data from multiple angular positions. We presented the significance of the improvements in image quality on PVA phantom, and on the *ex vivo* human plaque data. In combination with suitable pulse energy and wave lengths, the limited range of rotation may allow for non-invasive imaging and characterization of atherosclerotic plaques *in vivo*.

3.7 Acknowledgments

The author acknowledges Dr. Jaeger from University of Bern for sharing the MATLAB script for the k-space reconstruction of ultrasound and photoacoustic data. This study is funded by the European Community's Seventh Framework Programme (FP7/2007-2013) under grant agreement n° 318067.

Chapter 4

Unmixing multi-spectral photoacoustic sources in human carotid plaques using non-negative independent component analysis

The content of this chapter is based on M. U. Arabul, M. C. M. Rutten, M. R. H. M. van Sambeek, F. N. van de Vosse, and R. G. P. Lopata, "Unmixing multi-spectral photoacoustic sources in human carotid plaques using non-negative independent component analysis," *Photoacoustics, Under Review*.

4.1 Abstract

Multi-spectral photoacoustic imaging (MSPAI) is promising for morphology assessment of carotid plaques; however, obtaining unique spectral characteristics of chromophores is cumbersome. We used MSPAI and non-negative independent component analysis (ICA) to unmix distinct signal sources in human carotid plaques blindly. The feasibility of the method was demonstrated on a plaque phantom with hemorrhage and cholesterol inclusions, and plaque endarterectomy samples *ex vivo*. Furthermore, the results were verified with histology using Masson's trichrome staining. Results showed that ICA could separate recent hemorrhages from old hemorrhages. Additionally, the signatures of cholesterol inclusion were also captured for the phantom experiment. Artifacts were successfully removed from signal sources. Histologic examinations showed high resemblance with the unmixed components and confirmed the morphologic distinction between recent and mature hemorrhages. In future preclinical studies, unmixing could be used for morphology assessment of intact human plaque samples.

4.2 Introduction

Tissue specificity of photoacoustic imaging (PAI) has sparked research interests in various fields of biomedical imaging and applications. In case tissues have different optical properties (i.e., wavelength-dependent absorption), PAI is able to provide the tissue composition together with the anatomical reference obtained from ultrasound (US). Cardiovascular disease diagnosis is one of the promising areas where PAI has potential in both noninvasive [74]–[76] and intravascular imaging [50], [71], [86], [88]. One important application is the use of PAI to obtain the morphology of atherosclerotic plaques. Using multiple wavelengths, PAI has the potential to reveal the tissue 'signatures' of an unstable plaque such as intraplaque hemorrhages, necrotic lipid pool, and macrophage dispositions [72]. Mostly, the recorded photoacoustic (PA) signals from a plaque are not originating from a single chromophore. Instead, the PA response is the collective contribution of different chromophores. The composition of atherosclerosis is rather complex and different constituents are regarded as a continuum. Recent studies reported that the composition of a plaque is continuously transforming [11]. Findings implied that intraplaque hemorrhages entail the

lipid accumulation and that the content of hemorrhages was accompanied mostly by lipids. Therefore, it is not trivial to draw borders between different tissue components at any time in the progression of the plaque. Furthermore, in the literature, it was reported that the PA response of a mixture of components is highly dependent on the concentration of the absorbers [113], [114]. Despite the complexity of the tissue composition, the intrinsic chromophores can be revealed using spectral unmixing techniques. In the case the spectrum of the components is exactly known, a linear least-squared error minimization fitting procedure can be used to unmix these sources [115], [116]. However, the absorption curve of the chromophores should be known *a priori*, which is not possible for *in vivo* applications. Additionally, this unmixing approach requires higher sampling in the optical spectrum; i.e., the number of wavelengths used in PA measurements should be sufficiently high to fit data accurately. Mercep et al. reported that the number of wavelengths used should be roughly 7 for separating oxygenated and deoxygenated hemoglobin [75]. Finally, wavelength-dependent optical fluence differences should be corrected for in order to make a correct quantitative estimate in linear fitting-based unmixing methods [117], [118].

Spectral absorption *in vivo* will be most likely unknown due to the unknown and complex plaque morphology and the reported intersubject variability of optical properties [36], [119], [120]. Therefore, blind source separation could be an option for PAI of plaques. The most commonly used blind unmixing techniques are principal component analysis (PCA) and independent component analysis (ICA). Glatz et al. reported that ICA outperforms PCA in unmixing of PA signals [116], [121] by in the sense of better separation. Additionally, PCA can be used complementary to ICA to enhance the unmixing performance as a whole [122].

In this study, we aimed to adopt a data-driven approach to differentiate distinct components in human carotid plaque samples that have independent spectral behavior under different illumination wavelengths. Therefore, no prior spectral information is required as opposed to fitting based methods. The classical ICA method assumes a non-Gaussian, zero-mean data distribution of the signal values [123]. However, in the reconstructed PA images, the contrast is based on optical absorption of different tissues, which yields all positive data. Therefore, in this study, we used a modified version of the ICA algorithm for non-negative signal sources [124], [125].

Furthermore, we used spatially compounded photoacoustic data for unmixing. As a result, the optical fluence over the sample can be assumed to be homogeneous due to illumination from different perspectives (see [126]), and no additional fluence correction is required. For verification of the method, we applied the technique to a plaque phantom made of polyvinyl alcohol (PVA) with three different inclusions: fresh porcine blood, thrombus, and pure cholesterol. Next, we used the technique on human carotid plaque samples. We aimed to relate the unmixed components to the critical composition materials that can be found in the plaque. Finally, we performed histologic staining and microscopic examination of stained carotid plaque sections to verify the results of unmixing.

4.3 Materials and Methods

4.3.1 Sample Preparation for Imaging

PVA phantom preparation

A simplified plaque phantom was made to investigate the unmixing of different tissue components concurrently. The phantom is a cylindrical vessel tube of polyvinyl alcohol (PVA) with an external diameter of 8 mm and an internal diameter of 3 mm. Additionally, the mold was designed such that three cylindrical holes of 1 mm diameter in the vessel wall were available for inclusion materials (see Fig. 4.1). The PVA gel was prepared in demi-water with 15 wt% PVA (Mowiol 28-99, Sigma-Aldrich, Zwijndrecht, The Netherlands), and 1 wt% Orgasol (ELF Atochem, Paris, France) as acoustic scatterers [126]. Next, the gel was injected into the mold and subjected to 2 freeze-thaw cycles, i.e., freezing for 16 hours and thawing for 8 hours to stiffen the cryogel. Finally, the three inclusions were injected into the holes in the vessel wall, and the open ends were sealed using PVA and one additional freeze-thaw cycle. Porcine blood, freshly obtained from a local slaughterhouse, was used to mimic recent intraplaque hemorrhages. Next, human thrombus, obtained as waste material from an abdominal aortic aneurysm surgery, was used to mimic aged hemorrhages. Finally, commercially available cholesterol crystals (C8667, Sigma-Aldrich Chemie GmbH, Munich, Germany) were added to the third channel, representing a lipid inclusion [69].

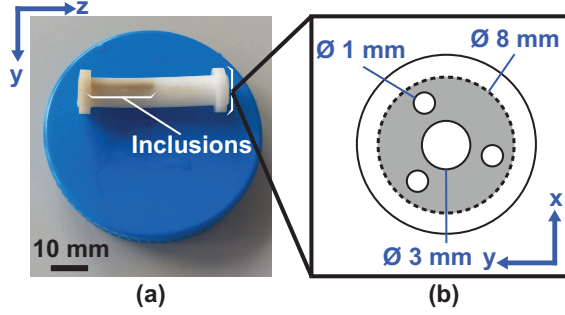


Figure 4.1: (a) The polyvinyl alcohol vessel phantom. (b) Illustrations of the phantom including dimensions. The diameter of the ends of the cylinder were enlarged for easy attachment to the imaging setup. The dashed-line indicates the diameter in the vessel area.

Human Plaque Samples

The carotid plaques were excised during carotid endarterectomy operations at the Catharina Hospital Eindhoven and transferred to the photoacoustic laboratory. The study was approved by the local ethics committee, and the samples were collected with the informed consent of the patients. Once the intact plaque sample was obtained, it was flushed with a phosphate-buffered-saline (PBS) solution to remove excess blood from the outer surface and the lumen. Next, two plastic cannulas were glued to the tips of the sample so that it could be mounted to the rotational measurement setup [101], [126]. In case the measurements were not performed on the day of the surgery, the samples were snap-frozen in liquid nitrogen and conserved at -80°C , until the experiment, and defrosted at room temperature prior to the PA measurements.

4.3.2 Scanning setup and photoacoustic acquisition system

Each sample was scanned in a custom-designed setup that allows controlled positioning (x, y, z) of the PA probe and the angular position (θ) of the sample. The setup consists of an immersion chamber (see Fig. 4.2), a three-dimensional (3-D) linear stage (M-403.2DG, Physik Instrumente, Germany), and a rotary controller (RS-40 DC, Physik Instrumente, Germany) controlled by a PC using LabVIEW software (National Instruments, Austin, Texas, USA). For a detailed description of the setup,

we refer to Arabul et al. 2016 [101]. The PA imaging probe consisted of a diode laser

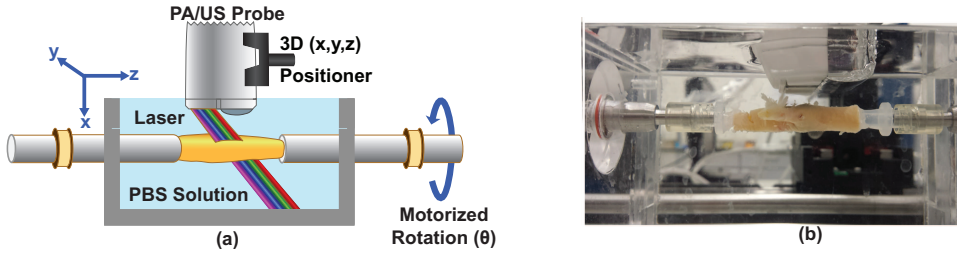


Figure 4.2: Illustration (a) and picture (b) of the experimental setup and photoacoustic (PA) probe used in this study.

(Lumibird, Paris, France) with four wavelengths ($\lambda = 808, 915, 940, 980$ nm), capable of generating pulses with a pulse duration of 130 ns and energy of 1 mJ. The acoustic signals were acquired by a linear array transducer (SL3323, ESAOTE, Maastricht, The Netherlands) that was integrated into the PA probe. For data acquisition, the PA probe was attached to an ultrasound scanner (MyLabOne, ESAOTE, The Netherlands), and the raw data were digitized at a sampling frequency of 50 MHz before transfer to a PC [95].

4.3.3 Experiment Protocol

A single image frame in both PA and US mode is obtained after spatially compounding 36 image data acquired from different angular positions. The details and the advantages of spatial compounding method were presented previously by Arabul et al. [126]. Briefly, the PA probe was positioned to image a cross-section of the sample, and the images were acquired by rotating the sample by 10° , covering the full 360° . Next, the 3-D stage moves to the next transverse position with a step size of 0.5 mm, and the semi-tomographic, compound imaging is repeated. Depending on the length of the sample, approximately 50 cross-sectional images were recorded for each wavelength. During the experiment, the temperature of the immersion bath was kept at body temperature (37°C). The effect of the temperature was not tested; however, it is known from the literature that the PA pressure increases with increasing medium temperature [127], [128]. Therefore, body temperature was preferred instead of room temperature.

4.3.4 Blind Source Spectral Unmixing

Since no prior information regarding the absorption spectrum exists due to the complex plaque morphology, and multiple chromophores concurrently contribute to PA generation, a blind-source unmixing technique was implemented, and its ability to distinguish chromophores in plaque tissue was investigated. Assuming that the contribution of each chromophore to the PA signal is statistically independent [123], the sources can be unmixed with independent component analysis (ICA)[116], [121], [129]. In this study, the algorithm of Oja et al. for non-negative signal sources was adopted [124], [125].

The value of each pixel in a PA image is assumed to be the weighted sum of different PA sources. Then the PA measurements can be formulated as

$$\underline{p} = \mathbf{A}\underline{s} \quad (4.1)$$

where \mathbf{A} is an $m \times n$ matrix. The elements of the vector \underline{s} (s_i for $i = 1, 2, 3, \dots, n$) represents the actual independent sources and the elements of the matrix \mathbf{A} (a_{ij} for $i = 1, 2, 3, \dots, m$ and $j = 1, 2, 3, \dots, n$) represents the weight of the j^{th} independent component (IC) for the i^{th} measurement. Then, \underline{p} becomes a column vector that represents m measurements of a single pixel. Therefore, 2-D PA images were reshaped into a 1-D row vector to treat images as a random variable. Next, PA images from different transverse positions were concatenated to obtain photoacoustic measurement matrix \mathbf{P} of size $m \times l$, with l being the total number of pixels.

The number of measurements should be at least equal to the number of independent components for unmixing to converge and lead to an accurate solution. Therefore, \mathbf{A} becomes an orthogonal unit variance matrix that is $\mathbf{A}\mathbf{A}^T = \mathbf{I}$. Thus, the blind source separation problem can be restated as finding an orthogonal unmixing matrix \mathbf{U} of size $m \times m$ from measurements \mathbf{P}

$$\mathbf{Y} = \mathbf{U}\mathbf{P} \quad (4.2)$$

where \mathbf{Y} represents the permutation of independent sources, i.e., different PA absorbers. Unmixing matrix \mathbf{U} was calculated based on an iterative optimization algorithm as described by Oja & Plumbley [124]. First, all PA images from all the plaques were rearranged, so that each row represents a measurement with one of

the four wavelengths ($\lambda = 808, 915, 940, 980$ nm) and columns represent different pixels. Next, data are pre-whitened using an $m \times m$ matrix \mathbf{V} to obtain a unit-variance matrix $\mathbf{Z} = \mathbf{V} \times \mathbf{P}$; i.e. the covariance matrix $cov(\mathbf{Z}) = \mathbb{E}((\mathbf{Z} - \mathbb{E}(\mathbf{Z}))(\mathbf{Z} - \mathbb{E}(\mathbf{Z}))^T) = \mathbf{I}$. This is required for working around the zero-mean data distribution requirement of conventional ICA. Finally, an optimization algorithm was applied to the whitened data \mathbf{Z} to find \mathbf{W} such that $\mathbf{Y} = \mathbf{W} \times \mathbf{Z}$, by minimizing the cost function:

$$\mathbb{E} \|\mathbf{Z} - \mathbf{W}^T(\mathbf{Y}^+)\|^2. \quad (4.3)$$

The matrix \mathbf{Y}^+ is obtained by selecting only the positive values of \mathbf{Y} . See the study by Oja & Plumbley [124] for further details of the algorithm.

The unmixing algorithm was applied to the datasets of individual plaque samples both separately, and to a combined dataset, i.e., all plaque PAI datasets merged as input for one unmixing step.

4.3.5 Histology Procedure

The plaque samples were fixated in 3.7% formalin solution for 24 hours. Next, the samples were decalcified in buffered ethylenediaminetetraacetic acid (EDTA) solution for a week. The buffered EDTA solution was prepared by mixing 400 ml phosphate buffered saline (PBS) solution with 40 gr of EDTA powder (Sigma-Aldrich Chemie GmbH, Munich, Germany). Next, NaOH pellets (Merck, Darmstadt, Germany) were added gradually to adjust the pH to 7.5.

Next, tissue samples were dehydrated with a standard tissue processor (Microm STP 120, Thermo Fisher Scientific, Walldorf, Germany) and embedded in paraffin blocks. Samples were sectioned in the transverse plane with the thickness of $5 \mu\text{m}$ using a microtome (RM2255, Leica Microsystems B.V., Amsterdam, The Netherlands). Finally, histology sections were stained with Weigner's Iron Hematoxylin and Mason's trichrome (Sigma-Aldrich Chemie GmbH, Munich, Germany). The histology overview images were manually matched to the US images based on the structural similarity of the lumen and vessel wall.

4.4 Results

The results of the plaque phantom are presented in Fig. 4.3 demonstrating the effect of unmixing on PA data. See Supplementary Fig. 4.7 for the effect of unmixing on plaque data. Fig. 4.3b is the compounded US image that clearly resembles the geometry of the phantom. The echogenicity is lowest for the blood and the highest for the cholesterol crystal. The high echogenicity of the cholesterol is due to the relatively stiff crystal form of the cholesterol used, and should not be mistaken for calcifications in plaque samples. The PA images of the phantom obtained at the four available wavelengths ($\lambda = 808, 915, 940, 980$ nm) are shown in Fig. 4.3c-f. The dynamic range of the colormap of each PA image is normalized with respect to its maximum intensity. Although the signal intensities vary, all four PA images provide signals from all three inclusions. The signals from the cholesterol are much lower than the hemorrhages due to low absorption of lipid in the spectral range available. However, as seen in Fig. 4.3f-i, the results of blind source unmixing do reveal different patterns of the plaque. The unmixed components are labeled as follows: IC1 is fresh blood, IC2 is the thrombus-based hemorrhage, IC3 shows the signal from all three components, and lastly, IC4 is the compounding artifact with the outer boundary of the sample. The overlaid US and PA images were rendered in 3-D, see

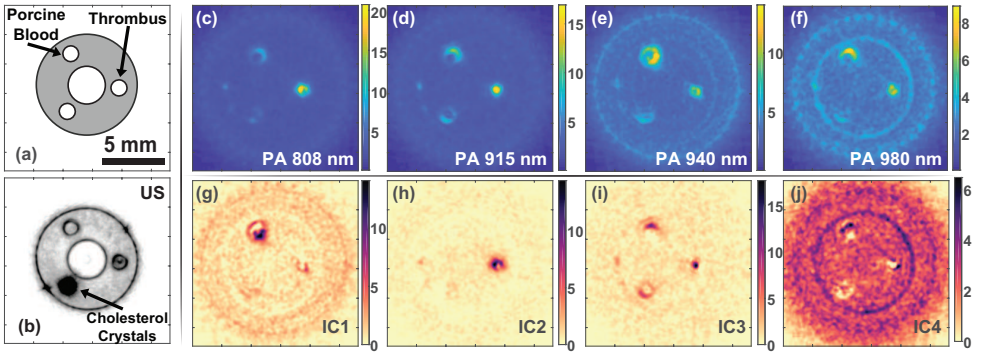


Figure 4.3: A cross-section image of PVA phantom: (a) an illustration, (b) ultrasound (US) image, (c-f) photoacoustic (PA) measurements at wavelengths $\lambda = 808, 915, 940, 980$ nm and (g-j) unmixed independent components, labeled as IC1 to IC4.

Fig. 4.4, to provide an overview of all samples and to demonstrate the continuity in

the unmixed PA sources. For visualization, non-linear transparency functions were used as the alpha channel for each image. Since the unmixing algorithm pushes the histogram of the sources away from each other, a different part of the colormap remains visible for different images after applying transparency in 3-D. The unmixing algorithm was applied to each individual carotid plaque dataset, and to a combined dataset, i.e., all plaque PAI datasets were combined and used as input for a single unmixing step. Due to variation in the signal-to-noise ratios (SNR) in the different datasets, unmixing performance decreases when all data were used together; i.e., the optimization converges with a more substantial mean-squared error (MSE). Despite the more noisy output, the converged optima and patterns of unmixed components did not alter significantly. Since the order of the unmixed components is arbitrary, the result of unmixing on combined data was used as a reference to obtain a consistent permutation of the independent components for all samples (i.e., sort them in the same order).

In Fig. 4.5, the results of unmixed PA data are presented together with the histology overview and US images. Each row represents a different cross-section (denoted as S1 and S2) obtained in various samples. The results of unmixing for plaque cross-sections are in agreement with the phantom results. IC1 represents the recent hemorrhages with a more confined area. IC2 shows a lower signal contrast than IC1; however, the area that provides a signal is generally originating from a larger area. Similar to the results of the phantom, IC4 resembles the outer boundary of the sample and the compounding artifact (circular haze).

Based on the overview of histology pictures, no indication of PA-based lipid detection was observed in the plaque samples, which is in contrast to the case of the pure cholesterol inclusion in the phantom. Therefore, further analysis of the histology images was performed, where the slices were subjected to microscopic examination (see Fig. 4.6). In Fig. 4.6 the histologic examination of two cross-sections is demonstrated, which supports the findings in the phantom experiments. The presence of erythrocytes (see Fig. 4.6 a-I) is evidence of recent hemorrhages, which matches with the dark high-intensity signals in the IC1 image. For the cross-section P1S1, the presence of erythrocytes is also confirmed in the zoomed image in Fig. 4.6b-I, which coincides with the signals in IC1 of the same section. Detailed examination of the histology sections for the regions with high signals in IC2 revealed the com-

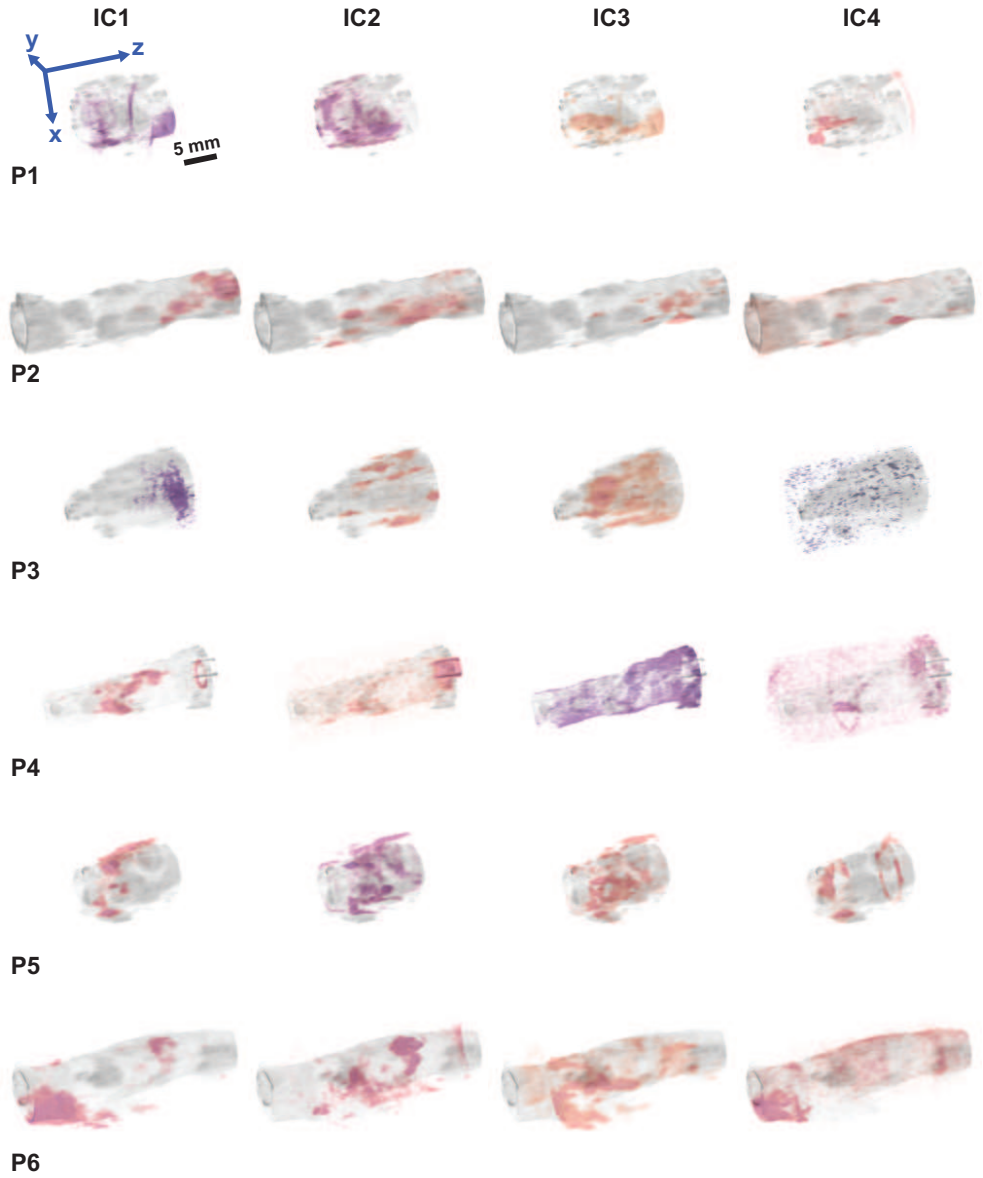


Figure 4.4: 3-D rendered overlay images of ultrasound (US) and unmixed photoacoustic signals, labeled as independent component (IC) IC1 to IC4. Each row shows a different carotid plaque sample (labeled P1 to P6).

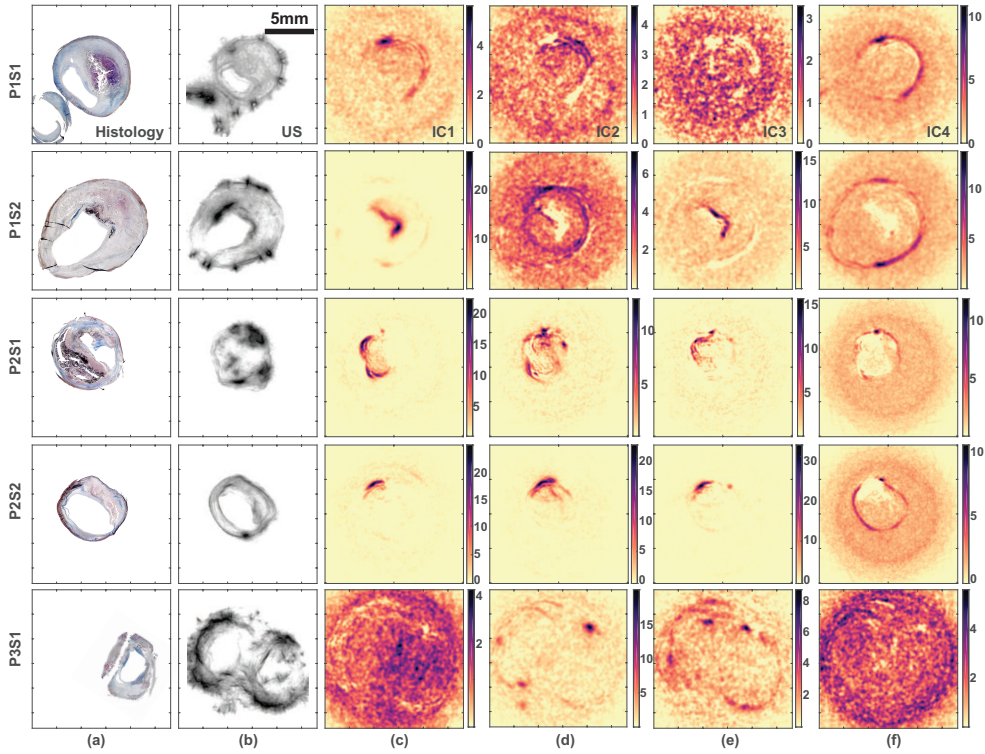


Figure 4.5: Overview of the measurements from five different cross-sections of three plaque samples and a cross-section of the PVA phantom. Rows show different cross-sections and the annotation P1S1 stands for ‘plaque one - section one’. The first column (a) is the histology section corresponding to the measured cross-section. The second column (b) is the US image to show the geometry of the measured cross-section. Please note that the dark color in the US image indicates high echogenicity. The columns from (c) to (f) are the independent components (IC1 - IC4) as the output of the unmixing algorithm. Darker color represents a higher signal in the unmixed source.

mon morphological characteristics. Having a darker pink color then its surrounding indicates the existence of matured hemorrhages in the vicinity. Additionally, those regions are accompanied by sharp-edged void areas that resemble the cholesterol clefts (see Fig. 4.6 a-II and b-II). This supports previous literature that old hemorrhages trigger lipid accumulation and their presence is mostly concurrent [11]. Finally, the high signal regions in IC4 coincide with the outer layer of the sample, see Fig. 4.6 (a-III) and (b-III). That is the media layer of the artery; however, we strongly

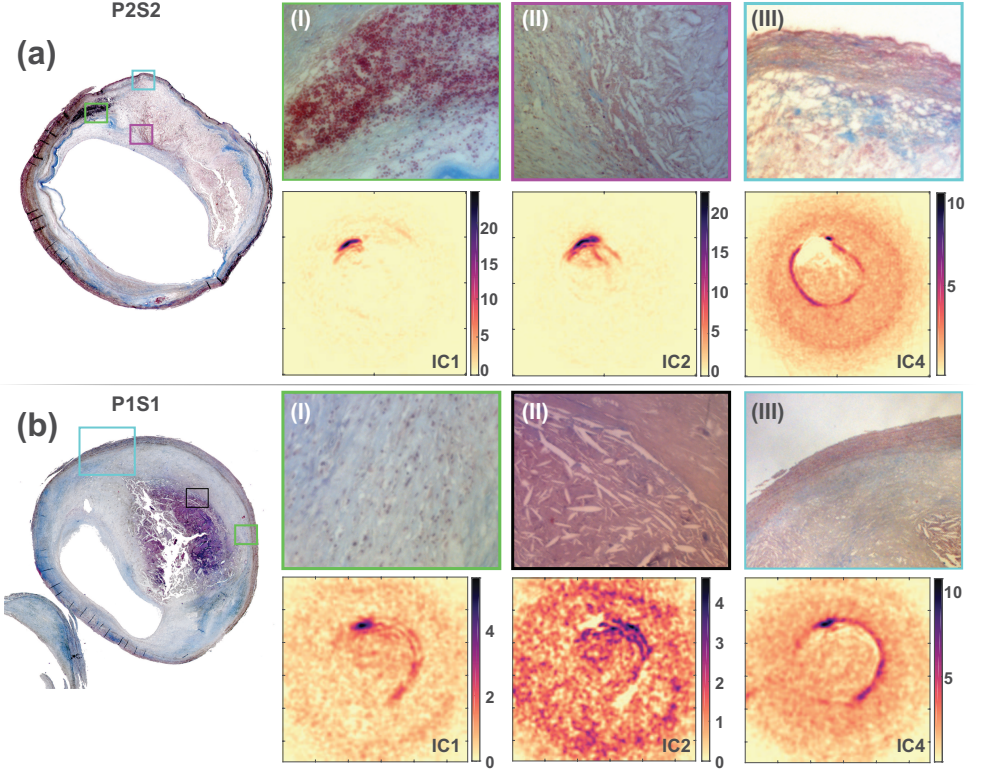


Figure 4.6: Histological details of plaque sample one - cross-section one (P1S1) and plaque sample two - cross-section two (P2S2). The overview of the histology is shown for two histologic sections in (a) and (b). The images (I) to (III) are the three magnified microscopy images of the histologic section. The locations of the magnified areas are indicated by the rectangles with different frame colors.

believe that this component is the PA signals generated on the surface of the sample. This is confirmed by the evidence that the same signal component was also present in the PVA phantom experiment. Since that surface PA signal also presents uniform behavior over the spectrum, it remains in the same component as the artifact.

4.5 Discussion

In this study, we showed the feasibility of blind-source spectral unmixing of multi-wavelength PA data obtained in human carotid plaques *ex vivo*. We adopted non-

negative independent component analysis (ICA) for unmixing reconstructed optical absorption maps obtained from PA measurements. We showed that unmixed components of PA images show high resemblance with the inclusions in the phantom experiments. Furthermore, we demonstrated that the results of unmixed components in distinct regions in the PA images that were corroborated by the histology images.

The two dominant PA sources, recent and matured hemorrhages, were successfully discriminated using blind-source unmixing. Detection of intraplaque hemorrhages is vital to capture indications of plaque vulnerability. Therefore, this can potentially be used to differentiate hemorrhages from the luminal blood when applied to *in vivo* data. Additionally, ICA was able to separate the large artifacts from the signal sources. In that sense, unmixing can also be used for denoising of multi-spectral PA data assuming that the artifacts will have a uniform response over the spectrum, which was in the case in our experiments.

IC3 as the output of unmixing provided signals from all three inclusions for the phantom. However, pure cholesterol crystals (as used in the phantom) are not found *in vivo* in carotid plaques, neither in these concentrations [130]. Moreover, the available wavelengths in this study were not optimal for PA signal generation in lipids. Therefore, the unmixing performance of the human plaque samples will be different from the phantom experiments.

The primary advantage of blind source unmixing is that no a priori data on the PA sources is needed, which makes the technique suitable for *in vivo* application. However, at the same time, this also is the main drawback of the technique due to the non-specific order of sources. Using a phantom, we were able to relate the unmixed sources in the plaque samples to the inclusions for proof of principle. Moreover, it provided partial validation of the signals measured in the plaque samples despite the limitations of the phantom as mentioned earlier.

During histology, the tissues were subjected to a sequence of chemical processes, which cause structural deformation. Therefore, the automatic registration of histology images to the images of a different modality, US images, was not feasible. Hence, a first, qualitative comparison of the selected cross-sections to the unmixed PA data

was presented instead of a quantitative comparison including all the cross-sections.

Blind-source spectral unmixing using non-negative ICA is promising for prospective *in vivo* application of PAI for carotid plaques. Spatial compounding can elevate the image quality when applied *in vivo* [126], whereas ICA-based unmixing can identify different plaque regions and remove the compounding artifact from actual signal sources. The principle of ICA dictates that all the data from different measurements should be complete. Therefore, it can only be implemented for off-line data. However, the mixing matrices obtained from real plaque samples can be used as a lookup table for real-time measurements. Possible unmixed components can be generated based on the same linear mixing model provide insight into the components.

For the future, a larger preclinical study is planned to support the findings in this study and showing the clinical relevance for a larger population. Furthermore, to obtain a better tissue specificity, additional staining methods will be used in histology to stain additional materials such as macrophages, collagen, and lipid.

4.6 Conclusion

In conclusion, we showed that a data-driven approach could be used to differentiate chromophores in human carotid plaque samples based on their independent PA response for distinct wavelengths. We used the non-negative ICA algorithm on spatially compounded photoacoustic data and showed that the recent hemorrhages and mature hemorrhages on plaques could be differentiated. Additionally, the signatures of cholesterol clefts were captured, which is supported by the phantom experiment and histologic analysis. Furthermore, using ICA, we demonstrated that the background artifact could be removed in the unmixed components, which elevated the PA image quality of unmixed components. The results of this study showed the merit of blind-source spectral unmixing for morphological assessment of the complex tissue compositions as carotid plaques, in which the spectral absorption is most likely unknown.

4.7 Acknowledgments

The author acknowledges Dr. Jaeger from the University of Bern for sharing the MATLAB script for the k-space reconstruction of ultrasound and photoacoustic data. We thank Hans-Martin Schwab and Georg Schmitz from the Ruhr-Universität Bochum for valuable discussions regarding spectral unmixing. We would also like to show our gratitude to Dr. Aryan Vink from the University Medical Center Utrecht for contributions on histologic examination. This study is funded by the European Community's Horizon2020 (CVENT) under grant agreement no: 731771.

4.8 Supplementary Materials

4.8.1 ICA overview of plaque section

In Fig. 4.7, an example cross-section is shown to illustrate the performance of ICA on PA images similar to polyvinyl alcohol (PVA) phantom case. Fig. 4.7a shows the geometry of the plaque cross-section obtained using the rotational compounding approach, using all 36 spatially compounded US images. The darker color in the gray-scale indicates higher echogenicity in pulse-echo images; therefore, these regions are identified as calcified regions. Fig. 4.7b-e shows the PA images of the same imaging plane, obtained at the four available wavelengths ($\lambda = 808, 915, 940, 980$ nm). The dynamic range of the colormap of each PA image is normalized to its maximum intensity. The dominant patterns in all PA images are similar; therefore, no differentiation between distinct chromophores is possible. However, as seen in Fig. 4.7f-i, the results of blind source unmixing do reveal different signatures of the plaque. Since the unmixed source matrix Y in Eq. 4.2 is a permutation of the independent sources, the order is arbitrary and does not indicate any specific chromophores alone.

4.8.2 Convergence MSE values of ICA

Non-negative ICA algorithm was applied to each sample separately and as well as the combined data. Table 4.1 shows the mean square error (MSE) of the converged optima for both cases. As seen in the table, MSE is less when ICA was applied to individual samples except for the P2.

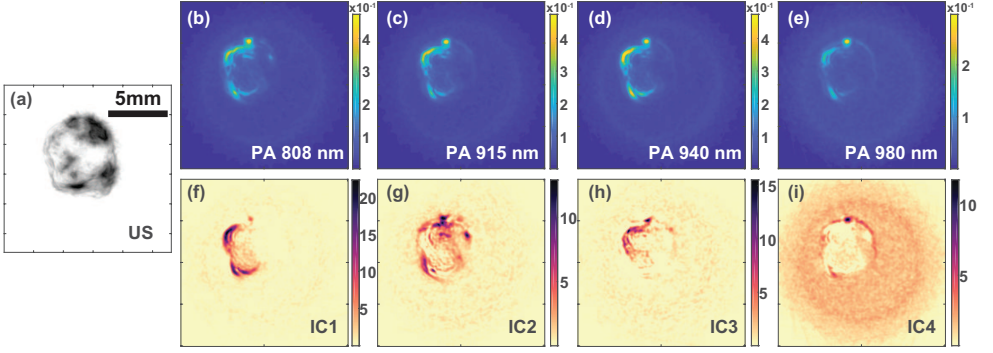


Figure 4.7: An example cross-section to illustrate the effect of blind source spectral unmixing using independent component analysis. (a) Shows the US image of the cross-section. From (b) to (e) are the PA measurements at wavelengths $\lambda = 808, 915, 940, 980$ nm. Figures (f) to (i) are the unmixed independent components, labeled as IC1 to IC4.

Unmixing combined data provided a consistent order of the independent components. Moreover, as seen in Fig. 4.8, the main pattern of unmixed signals do not differ significantly for both cases. Therefore, results with less MSE were presented for the manuscript.

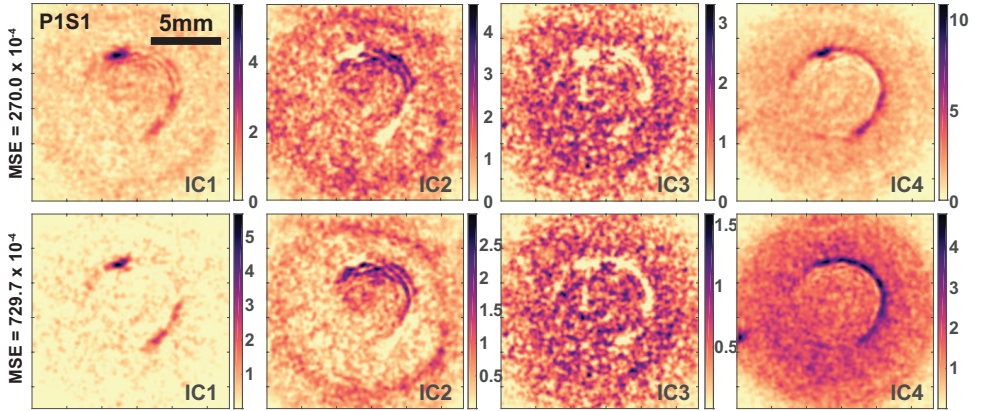


Figure 4.8: Unmixed components of plaque 1 - sample 1 (P1S1) to demonstrate the effect of converging error on the result images.

Table 4.1: The mean square error (MSE) of the converged optima for ICA.

	P1	P2	P3	P4	P5	P6
Individual MSE ($\times 10^{-4}$)	270.0	760.2	69.4	112.1	89.7	149.0
Combined MSE ($\times 10^{-4}$)	729.7	729.7	729.7	729.7	729.7	729.7

Chapter 5

Photoacoustic simulation tool-chain for 3-D simulations of heterogeneous media

The content of this chapter is based on M. U. Arabul, M. C. M. Rutten, M. R. H. M. van Sambeek, F. N. van de Vosse, and R. G. P. Lopata, “Photoacoustic simulation tool-chain for 3-D simulations of heterogeneous media,” *In Preparation*.

5.1 Introduction

Photoacoustic imaging (PAI) has been attracting scientific interest for biomedical applications due to its high potential in tissue specificity [131]. Photoacoustic (PA) is based on pressure wave generation at the site of endogenous absorbers due to optical absorption and subsequent thermo-elastic expansion. For an efficient PA generation, the optical illumination duration should be much less compared to the thermal diffusion and stress relaxation time of the absorber which yields pulse durations in the order of nanoseconds [43], [49]. Next, the PA waves, which propagate in biological tissue obeying the 3-D wave equation, can be detected by an ultrasound transducer from the tissue surface. Finally, PA images are formed by reconstructing the initial pressure distribution, see Chapter 1. Hence, PAI provides a contrast based on the wavelength-specific optical absorption of biological tissues with the acoustic resolution of medical ultrasound.

PAI technology requires comprehensive knowledge and advanced technology in both photonics and acoustics. There are various approaches both in the photonic part of the PA system, e.g., the use of fiber lasers [132], crystal lasers [133], and diode lasers [95], [134], as well as in the acoustic part of the system including single element transducers [135], linear array medical transducers [95], and custom-designed transducers [74], [75]. The use of conventional (linear) array transducers is in high demand due to the potential that such a PAI system can easily be applied in the clinic as an add-on to the current clinical ultrasound systems.

During PA acquisition with a linear array transducer the system acquires data that originates from a 3-D volume; however, the conventional reconstruction algorithms adopted from pulse-echo ultrasound are based on 2-D assumptions. Due to the acoustic lens, the emitted US energy is concentrated within a slab with limited thickness in the out-of-plane direction. Therefore, the 2-D assumption works well with conventional pulse-echo US imaging. However, light illumination propagates more diffusely in 3-D due to significant scattering in turbid tissue. Hence, some contribution to the PA waves sensed by the array originates from the outside of the 2-D imaging plane as well. Applying the reconstruction algorithm, which was modeled based on 2D propagation, projects those out-of-plane signals to the imaging plane

and creates so-called clutter artifacts.

New solutions to these challenges of PAI are mostly tested on tissue-mimicking phantoms that have fixed optical and acoustic properties. In reality, a wide range in optical and acoustic properties is found *in vivo* which may vary between subjects. Manufacturing multiple phantoms with sufficient realism that cover all these different values is cumbersome. Therefore, there is a high need for a photoacoustic simulation tool-chain to simulate realistic images, from optics to acoustics, to test new acquisition schemes, quantify penetration depth or expected SNR *in vivo*, or identify and characterize possible clutter sources.

Jacques used a Monte Carlo (MC) simulation developed for layered, homogeneous structures. In this study, the energy deposited in a spherical volume was coupled to the initial source of the acoustical simulation to calculate the velocity potential of the induced stress at the tissue surface[136]. The optical part of the simulation was designed for simple, layered geometries only. Furthermore, this approach assumed homogeneous acoustic properties in the acoustic part of the simulation.

Mastanduno et al. used k-Wave simulations to develop an accurate reconstruction of optical absorption in quantitative PA tomography in 2-D. Here, the analytical solution to the diffusion equation for homogeneous media was used to perform optical simulations [137]. Only a few other studies are found that aimed to reconstruct quantitative optical absorption in a similar approach; however, with different methods, including iterative reconstruction, to simulate PA signals in simple 2-D geometries [138], [139]. The optical photon distributions were estimated based on the numerical approximation of the analytical photon diffusion equation for a homogeneous medium. Additionally, the acoustic waves at the boundaries (sensor locations) were calculated using the forward solution of the 3-D PA wave equation for a homogeneous tissue.

Mostly, *in vivo* PAI targets tissues with complex geometries and heterogeneities, which can also vary between different subjects. Therefore, the challenges introduced for *in vivo* application require dedicated solutions that cannot be replicated with simple simulation geometries with homogeneous properties. Hence, there is an unmet need that would enable PA simulations of complex heterogeneous structures.

In this study, we aimed to create a PA simulation tool-chain: from optics to acoustics, and, finally, reconstruction of PA images. The tool-chain was designed such that it can simulate PA generation in complex heterogeneous geometries of known geometries (phantoms) or based on clinical or histological input to simulate realistic in vivo PA images. To achieve this, we combined an existing open-source simulation toolbox that was used in the field of biomedical optics with the acoustic k-Wave Toolbox and characterized the resulting PA images. Finally, we simulated a carotid plaque sample, as investigated with PAI in previous chapters. The geometry and optical map were created using histological images of a real carotid plaque sample and tissue parameters obtained from the literature, and results were compared to real PA measurements of the same sample.

5.2 Materials and methods

5.2.1 Monte Carlo Photon Migration

An open-source tool, a mesh-based Monte Carlo (MMC) method for the simulation of photon distributions, was adopted from [140], [141]. The MMC is able to simulate photon distribution in any 3-D geometry that is meshed with tetrahedral elements. The software is based on the ray-tracing technique using Plücker Coordinates [140]. Therefore, it allows for the simulation of curved structures with an arbitrary shape. After generation of the 3-D mesh and assignment of the optical properties to each element, and definition of the necessary input parameters, the simulation is executed. These steps are described in more detail in the following sections.

Mesh generation

Two different phantoms were designed and simulated: a simple sphere in a homogeneous block of surrounding material, and a carotid plaque sample. For the simple spherical mesh phantom (see Section 5.2.3), DistMesh (Department of Mathematics, UC Berkeley [142], [143]) was used to generate spheres. For the more complex phantom, i.e., the human plaque sample, the surface meshes were created by manually segmenting histology pictures, 10 consecutive cross-sections of a plaque sample obtained from a local hospital (see Chapter 4 for details) in Blender (Blender Foun-

dation, Amsterdam, The Netherlands). Next, a box surface surrounding the objects (either the spheres or the plaque mesh) was created manually in MATLAB (R2017a, The Mathworks, Natick, MA, USA). The whole surface mesh was then exported as piece-wise linear complex (PLC). Finally, TetGen (3-D Delaunay Triangulator [144], WIAS, Berlin, Germany) was used to re-mesh 3-D volumes with tetrahedral elements based on the surface meshes.

Additionally, the mesh was re-tessellated to add the illumination plane as a part of the mesh. This was to meet the requirement of the MMC method that the light source should be enclosed, thereby allowing a custom-shaped illumination geometry. See Yao et al. for more details [145].

Optical properties

The optical properties were defined for each mesh element in the MMC simulation. This desired property of the method allowed for simulation of the photon distribution in complex heterogeneous geometries. The optical properties used in the MMC simulations are the optical absorption coefficient μ_a (cm^{-1}), the scattering coefficient μ_s (cm^{-1}), the refractive index n (dimensionless), and anisotropy constant g (dimensionless).

The optical properties are wavelength dependent; therefore, the optical properties for four wavelengths (808, 915, 940, and 980 nm), that were available in the PA system described in Chapter 4, were used. Properties were all based on values found in literature and are tabulated in Table 5.2. For absorption and scattering of the different tissues distinct values for each wavelength were found except for the muscle tissue. The refractive index, n , and the anisotropy constant, g , were assumed to be the same for all wavelengths. In case the values for the desired wavelengths were not explicitly available in literature, values were interpolated based on the existing data [36].

Simulation input and output

The pre-compiled binary of the MMC simulation, suitable for multi-core processors, was used on a computational cluster (22 Intel Xeon X5550 nodes, each with 2 Ne-

Table 5.1: Optical properties for different tissue types. The values were adopted from the literature and corresponding references are indicated next to the values.

Tissue Types	μ_a [cm ⁻¹]	μ_s [cm ⁻¹]	g	n
water [146]	19.9×10^{-3}	10^{-6}	0.99	1,33 [36]
	91.1×10^{-3}			
	267.4×10^{-3}			
	430×10^{-3}			
skin	1.5	463,90	0.95 [147]	1,36 [148]
	1.28	398,01		
	1.15	385,42		
	0.9 [147]	366,97 [36]		
fat/lipid	49.70×10^{-2}	266,83	0.95 [150]	1,33 [150]
	899.40×10^{-2}	247,26		
	875.40×10^{-2}	243,30		
	141.70×10^{-2} [149]	237,34 [36]		
muscle [151]	0.54	66.70	0.95	1,37
vessel wall	1,09	4,22	0.91 [152]	1,38 [153]
	0,97	2,64		
	0,96	2,27		
	0,94 [83]	1,68 [83]		
hemorrhage	3,88	762.5	0.98 [155]	1,35 [36]
	4,17	678.2		
	3,71	660.8		
	1,93 [36], [154]	626.8 [155]		

halem quad-core processors) to simulate 10^6 photons on each mesh. The optical fluence at each node was stored as simulation output. The output of MMC provided the normalized flux in the unit area, i.e., when the mesh coordinates are in mm then the output corresponds to the fraction of the input optical energy, and the unit becomes $1/mm^2$. Since the laser pulse energy was 1 mJ per pulse in the PA system used in Chapter 4, the output flux unit was regarded as (mJ/mm^2) .

5.2.2 Acoustic Wave Propagation

The acoustic wave propagation was simulated using the open-source k-Wave toolbox that uses a pseudo-spectral, time-domain, finite difference method to solve the governing wave equation to simulate the ultrasound propagation [156]. k-Wave calculates the acoustic wave propagation over a regularly spaced Cartesian grid. The transducer (sensor) positions, the initial pressure source, and the acoustic properties of the different media should be defined in the so-called k-grid.

In our simulations, we modeled the ultrasound transducer that is part of the same PA system available in our research lab (Chapter 2). The PA system consisted of a linear array transducer with 64 elements with a pitch of 245 μm (SL3323, ESAOTE, Maastricht, The Netherlands). However, for numerical reasons, the separation of the elements in the actual array (kerf) was not taken into account. By doing so, the bottleneck for grid density, use of a small kerf which leads to an extremely fine grid, was bypassed. The density of the k-grid determines the maximum acoustic frequency that can be simulated, and in case of a fine grid, the number of grid points, and thus the memory requirements and computation time, vastly increase [156], [157]. In all simulations, the kerf was set to zero, since the effect on the simulation results was found to be negligible (See Section 5.6.1)

To define the initial pressure sources at the absorber site, the optical flux output of the MMC simulation was interpolated to the Cartesian grid (k-grid) using linear interpolation. Similarly, the optical absorption values of the tetrahedral mesh were also interpolated to the k-grid. Lastly, the initial pressure was calculated by multiplication of the flux and absorption, μ_a , in an element-wise fashion. In theory, the PA wave generation also depends on the Grüneisen coefficient; however, it was assumed to be constant (and was set to 1) for all biological tissues for computational simplicity [158].

Acoustic Properties

The acoustic properties of different tissues were defined for each tetrahedral mesh element using the existing segmentation of the meshed structure. The values were adopted from the database of ITIS [159] and are listed in Table 5.2. The acoustic

properties used in k-Wave were the mass density ρ (kg/m^3), the speed of sound c_0 (m/s), and the attenuation coefficient α_0 (dB/cm/MHz). Additionally, k-Wave takes the power law of the frequency dependent attenuation into account. However, for all the acoustic simulations the attenuation power was chosen to be 1.005, close but not equal to 1, as suggested in [157]. Lastly, the acoustic properties of the tetrahedral mesh were interpolated for the k-grid as used when interpolating the MMC output flux.

Table 5.2: Acoustic properties for different tissue types. The values were adopted from the literature [159].

Tissue Types	α_0 [dB/cm/MHz]	ρ [kg/m ³]	c [m/s]
water	0.0022	994	1482
skin	1.84	1109	1624
fat/lipid	0.38	911	1440
muscle	0.62	1027	1545
vessel wall	0.61	1102	1569
hemorrhage	0.21	1050	1578

5.2.3 Simulations

Embedded Spheres

First, a simple phantom was constructed. Two spheres of 2 mm in diameter were simulated to characterize the point source response of the PAI system using the simulation tool-chain. The optical properties of blood were assigned to the spheres to exhibit high absorption at a wavelength of 808 nm. The surrounding medium was chosen to be muscle tissue. PA images were simulated for 2 different cases: (1) both spheres were in the imaging plane, where one sphere was kept at a depth of 12 mm, whereas the depth of the other sphere was varied between 4 mm to 20 mm in 2 mm steps. (2) One sphere was kept in the imaging plane at the same constant position (12 mm), but now the second sphere was moved orthogonally (in the +z direction), away from the imaging plane up to 21 mm (in 2 mm steps). For each sphere ge-

ometry, a new mesh was generated, and the complete PAI simulation was repeated.

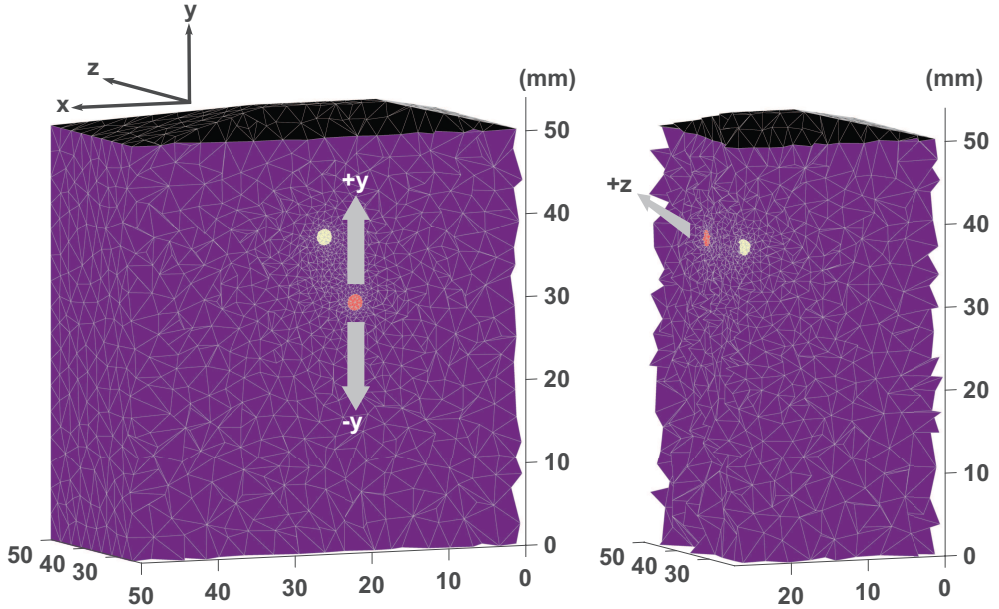


Figure 5.1: Mesh of the cube phantom with embedded sphere. An example mesh is given for each simulation case: in-plane and out-of-plane movement of the second sphere, respectively. The arrows indicate the direction in which the sphere moved for the two different simulation cases.

Human Carotid Plaque

The plaque mesh was simulated for four different excitation wavelengths (808, 915, 940, 980 nm), as were available and used in the *ex vivo* PA study on multi-spectral PA imaging of plaques (See Chapter 4). Upon the manual segmentation and meshing of the plaque section (8 mm long), the mesh was embedded in a multilayer surrounding medium mimicking connective surrounding tissue including muscle tissue, subcutaneous fat, and skin. See Figure 5.2 for the illustration. The transducer was positioned in the cross-section of the plaque mesh where the two hemorrhages and the lipid pool are visible. The optical properties of blood were used for the hemorrhages for simplicity. The same optical properties of the turbid surrounding

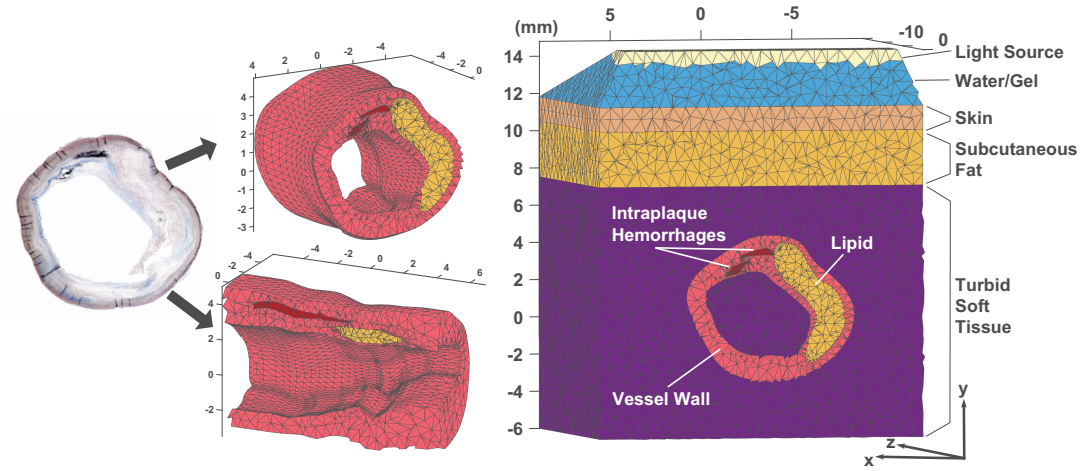


Figure 5.2: Cross-section of the 3-D mesh of a human carotid plaque. Tetrahedral mesh of a human carotid plaque sample that was created based on histology pictures of an actual human plaque sample. There are two intraplaque hemorrhage regions and one large lipid pool in the plaque.

tissue were assigned to the lumen. The optical photon distribution was simulated in 3-D for each wavelength. Next, the acoustic wave propagation was calculated for both 3-D and 2-D grids to observe the effect of PA sources in the regions outside of the imaging plane and their contribution to the PA signal acquired. Finally, the PA simulations of the plaque mesh were performed to simulate measurements *ex vivo*. Here, the surrounding medium is replaced by water, as was the case in the *ex vivo* experiments described in Chapters 2- 4.

5.3 Results

5.3.1 Sphere Simulations

The reconstructed images are shown in Figure 5.3. The in-plane simulation case (first row) nicely demonstrates the clutter caused over the sphere at the fixed position. As the position of the second sphere was set close to the probe, the signal generated by that sphere increases due to the increase in optical fluence, leading to more background noise. However, in the out-of-plane case, the effect of the second

sphere was only observed for the first two cases. For the rest of the cases, where the second sphere was positioned 7 mm to 21 mm away from the imaging plane, the optical fluence was not sufficient to create PA signals that lead to clutter in the imaging plane. The quantitative SNR comparison of the effect of the second absorber

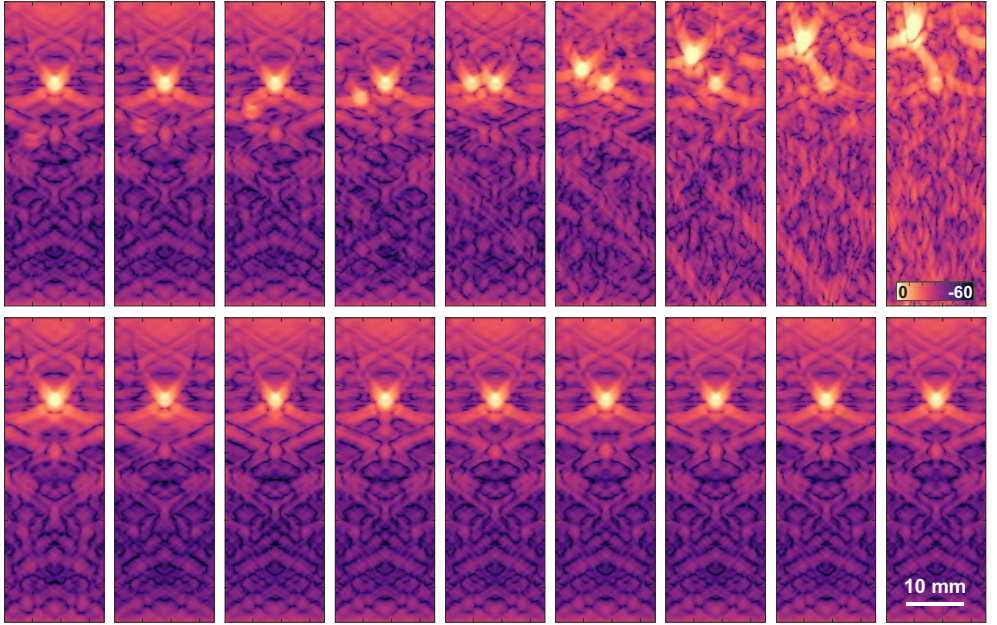


Figure 5.3: Results for the sphere-embedded cube phantom: the first row are PA images for the in-plane spheres with the second sphere at increasing height; the second row shows the PA images for the second case, with increasing out-of-plane distance of the second sphere.

was presented in Figure 5.4. The SNR of the fixed sphere decreased as the moving sphere approached the probe. There are two factors yielding this outcome: (1) as the second sphere absorbed more optical energy, the fluence at the fixed sphere is reduced, (2) the PA signal generated by the second sphere generated clutter artifacts around the sphere and additionally at deeper regions of the reconstructed image (See Figure 5.3).

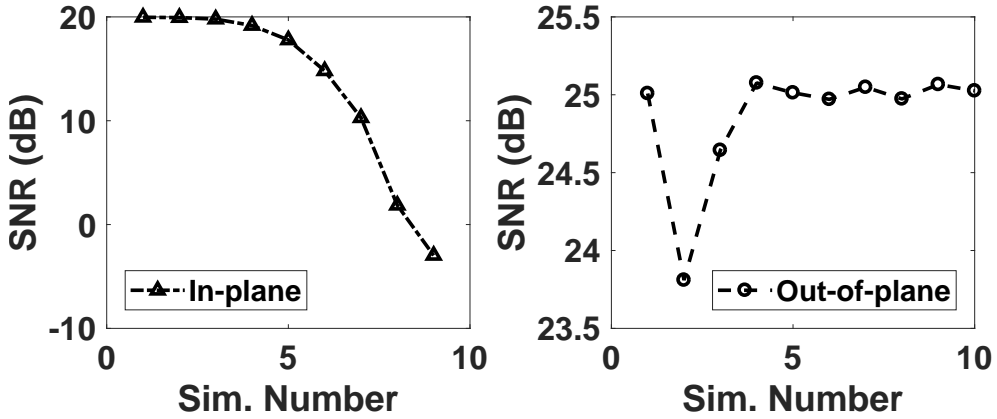


Figure 5.4: SNR analysis of the reconstructed images of the embedded sphere simulations for the in-plane and out-of-plane cases.

5.3.2 Human Carotid Sample Simulation

The simulation results of the carotid plaque mesh surrounded by water are shown in Figure 5.5. As seen in the optical flux results (see the second row of Figure 5.5) light propagates in water without significant scattering. Therefore, the top region of the absorbers consumes a significant amount of light. As a result, only the top part of the absorbers becomes visible in the reconstructed PA images. The PA simulation results resemble the experimental PA measurements performed with the actual carotid plaque sample *ex vivo* as described in Chapter 4. In Figure 5.6, the results of the PA experiments of the corresponding plaque sample are demonstrated. The simulated images resemble the actual measurements, especially for 808 and 980 nm. However, for 915 and 940 nm the lipid absorption was dominant in the simulated images. The simulation results of the carotid plaque mesh with the surrounding tissue (muscle, fat, and skin) are shown in Figure 5.7. For the realistic carotid simulation, the skin is the region where the highest optical fluence occurs. Therefore, in the k-Wave simulations, the initial pressure generated by skin suppresses the PA signal generated by the plaque in the reconstructed images. To circumvent this problem, the skin signal was removed from the initial pressure input of the acoustic simulations, as would be needed *in vivo*, using a Chebyshev window. In Figure 5.7 each row demonstrates a different step in the simulation tool-chain. The simulations demonstrate that the 3-D acoustic simulations have 2 dB less SNR (a drop from 16 dB to 14 dB) and re-

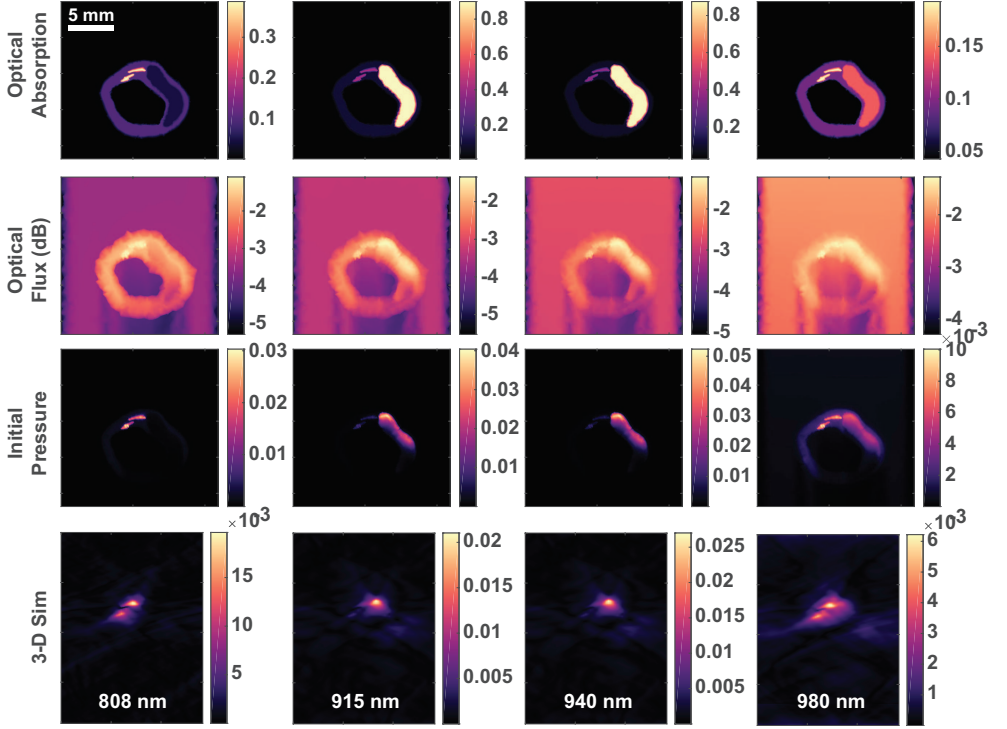


Figure 5.5: The results of the 2-D and 3-D PA simulations of a human plaque model when immersed in water as in *ex vivo* experiments. Each column represents the results of the photoacoustic simulation of human carotid plaque mesh for four discrete wavelengths (808, 915, 940, 980 nm). From top to bottom, the rows represent the optical absorption μ_a map of the medium, the optical flux results of the MMC simulation, the initial pressure input of the k-Wave, and the reconstruction results of the 3-D acoustic simulation.

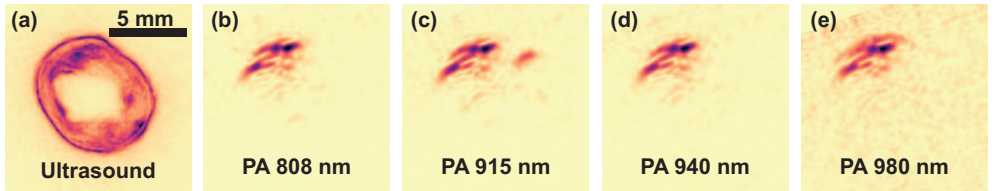


Figure 5.6: The results of the *ex vivo* experiments. (a) The ultrasound image obtained by spatial compounding (see Chapter 4) and (b-e) Photoacoustic measurements at a wavelength of 808, 915, 940, 980 nm.

semble the *in vivo* case better than the 2-D reconstruction assumption when a linear array ultrasound transducer was used.

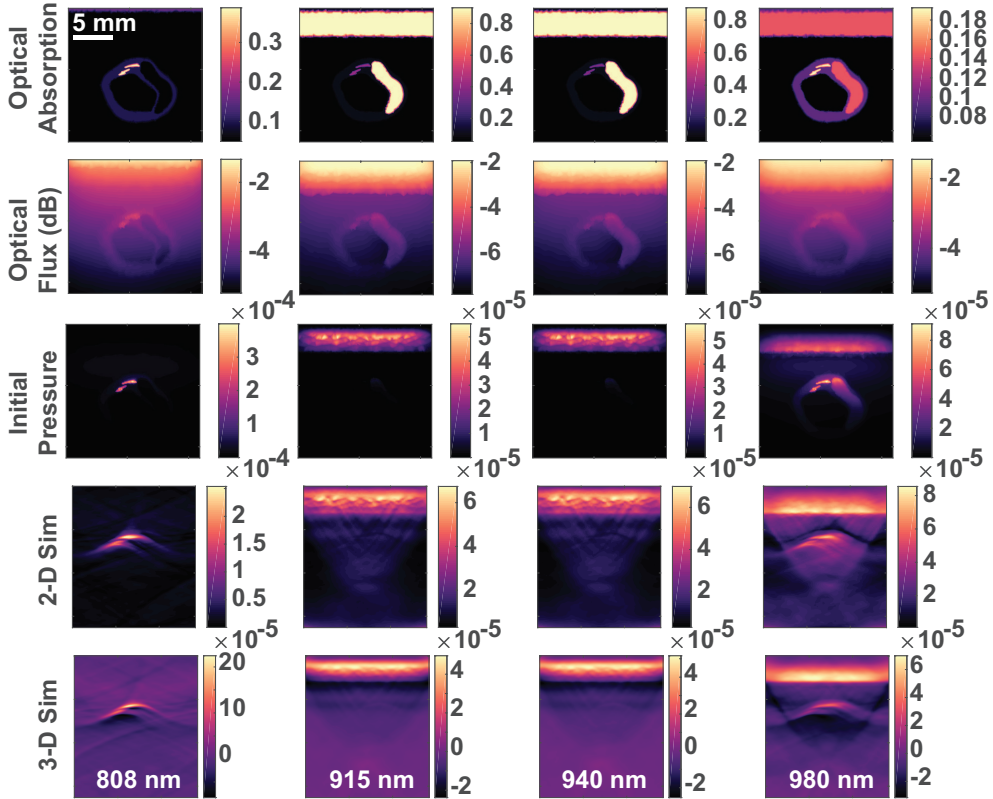


Figure 5.7: The results of the 2-D and 3-D PA simulations of a human plaque model. Each column represents the results of the photoacoustic simulation of human carotid plaque mesh for four discrete wavelengths (808, 915, 940, 980 nm). From top to bottom, the rows represent the optical absorption μ_a map of the medium, the optical flux results of the MMC simulation, the initial pressure input of the k-Wave, and the reconstruction results of the 2-D and 3-D acoustic simulations, respectively.

5.4 Discussion

In this study, we established a 3-D photoacoustic simulation tool-chain by coupling the optical flux estimation of mesh-based Monte Carlo (MMC) photon migration

analysis to acoustic simulations. We simulated PA wave generation and propagation in 3-D in phantoms. The performance of the simulation tool-chain was demonstrated with embedded sphere phantoms and showed that realistic clutter artifacts could be generated in a simulation environment. Furthermore, we modeled a 3-D plaque mesh based on a real human plaque geometry and simulated PA generation when surrounded by water as in the *ex vivo* experiments, with images closely resembling the actual measurement data. Finally, we embedded the plaque mesh into surrounding soft tissue including a subcutaneous fat and skin layer as in the *in vivo* case, to get an idea of *in vivo* performance of the technique.

Having such a simulation tool-chain is desirable, and has the potential to accelerate development of novel techniques toward *in vivo* PAI by providing a tool to manipulate the parameters more easily than in real measurements or phantom experiments. The PA tool-chain can also be beneficial to investigate limitations of methods and further improve the techniques presented in this thesis such as spatial compounding (Chapter 3) and blind-source spectral unmixing (Chapter 4).

The current optical and acoustic simulation tools used in this study are ongoing open-source projects and currently used in different fields. For example, the MMC simulations are widely used to estimate photon distribution in the brain for fMRI studies [160], [161].

The platform would facilitate simulation of novel imaging geometries and virtual patients, and aid in an initial performance assessment of new PAI techniques such as image reconstruction, spectral imaging, and clutter reduction. The tissue properties play a crucial role in the accuracy of the simulations. However, especially for optical properties, the variance in the values obtained from the literature is high due to the actual variance between different subjects and samples and additionally due to the different methods used for measuring optical properties. Therefore, a library for biological tissue properties could be useful to integrate into the PA simulation tool-chain, similar to the ITIS database available for acoustic simulation [159].

The difference between the simulated PA images and the measured PA images for 915 and 940 nm are mostly since the optical absorption values used pure fat in the simulation was not representative for the real plaque. In the real plaque samples,

the absorption by the hemorrhages was probably higher than the lipid pool for the corresponding two wavelengths.

For simulating the acoustic wave propagation, k-Wave was chosen due to availability and widespread use in the field of biomedical ultrasound and photoacoustics. However, for a large 3-D computation grid size, the memory requirements of k-Wave become very high (60 GB for human plaque simulations). Therefore, the simulations were run on a computational cluster. In the future, alternative acoustic simulation tools should be tested to investigate the performance improvements (in terms of computation time) compared to k-Wave.

The simulation tool-chain can be improved further by having a more realistic transducer model incorporating the directivity of the transducer elements. In the future, the PA simulations can also be combined with pulse-echo ultrasound simulations to generate hybrid PA/US imaging sequences. Moreover, the additional aspects of *in vivo* conditions can be added step-by-step. For example, the pulsation of the artery can also be simulated using a biomechanical simulation tool such as ABAQUS (Dassault Systèmes, Cedex - France) or measured *in vivo*, and added to the framework to simulate realistic, time-resolved PAI sequences.

5.5 Conclusion

In this study, we built a photoacoustic (PA) simulation tool-chain for 3-D heterogeneous media by adopting mesh-based Monte Carlo photon migration software with the k-Wave acoustic field simulation toolbox. The tool-chain is suitable for designing complex 3-D geometries and assigning heterogeneous properties to them, in both the optical and acoustic domains. With this flexibility and ease-of-use, we aim to provide an initial framework for future PA studies specifically towards advanced *in vivo* imaging, e.g. in carotid plaques.

5.6 Supporting information

5.6.1 Kerf Analysis

In the case of a realistic transducer, a kerf parameter should be defined as the input for the k-Wave simulations. However, a typical kerf size is approximately one-tenth of the transducer element width. So, for a 64 element transducer, it requires at least 640 grid points to define the transducer. This will lead to a significantly fine grid which increases the computation time and required memory. Therefore, we tested the effect of having a nonzero kerf in the transducer and compared the results (See Figure 5.8). A mesh of $512 \times 512 \times 512$ was created with a grid separation of

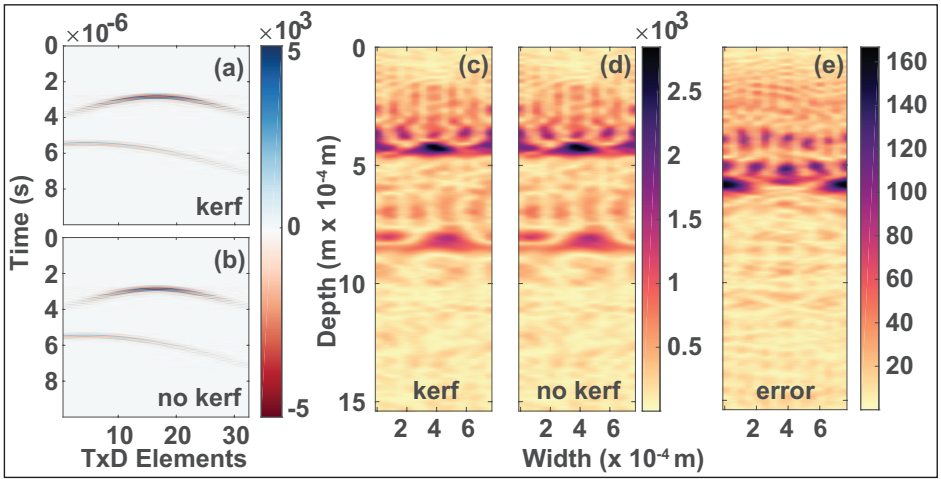


Figure 5.8: The effect of having zero element spacing in the transducer model in k-Wave results. The raw sensor data for the two cases: (a) non-zero element spacing and (b) zero element spacing. The reconstructed images of the same input for (c) non-zero element spacing and (d) zero element spacing. (e) The difference image of (c) and (d).

$24.5 \mu\text{m}$. Next, two point sources were defined, i.e., spheres with the diameter of 3 grid elements inside a cube. The grid medium properties were chosen to be homogeneous with the density $\rho = 1000 \text{ (kg/m}^3\text{)}$, the speed of sound $c_0 = 1500 \text{ (m/s)}$, and the attenuation coefficient $\alpha_0 = 0.75 \text{ (dB/cm/MHz)}$. A 64 element transducer was placed at the cross-section where the imaging plane intersects the center of the

sphere. Next, two cases were simulated: (1) A transducer element represented by nine grid points and a kerf of one grid point; (2) A transducer element was represented by ten grid points with zero element separation (kerf = 0). In both cases, the pitch of the transducer was kept the same.

The results of the simulations are shown in Figure 5.8. Qualitatively, the time-of-flight recordings (Figure 5.8a-b) and the reconstructed initial pressures (Figure 5.8c-d) of both transducers were similar in appearance. Next, to make a quantitative analysis, the normalized root-mean-squared error (NRMSE) between two reconstructed images was calculated and was found to be less than 0.4%. This led to the conclusion that the effect of having no kerf between the elements of the transducer has a negligible effect on the resultant image.

5.7 Acknowledgments

This study is funded by the European Community's Horizon2020 (CVENT) under grant agreement no: 731771. The author acknowledges the contributions of Osman Akdağ, Femke Vaessen, Max van Wanrooij during their Bachelor End Projects (Eindhoven University of Technology) and Arianna Girardi (University of Twente) for her master's internship.

Chapter 6

General Discussion

In this thesis, the merit of photoacoustic imaging (PAI) for carotid artery atherosclerosis was investigated in several preclinical studies. A novel experimental technique was developed for 3-D scanning of *ex vivo* samples of human carotid plaques to assess the capabilities and performance of photoacoustic imaging in a preclinical phase.

Using this *ex vivo* approach, the challenges of *in vivo* imaging, such as optical and acoustic attenuation due to soft tissue surrounding carotid artery was bypassed. Moreover, the optical fluence over the carotid artery was virtually equalized due to the multi-perspective illumination of the plaque and multi-angle, spatial compounding of the acquired PA data (Chapter 2- 3).

On seven endarterectomy samples, intra-plaque hemorrhages were successfully detected and mapped in 3-D using overlay PA and US images. Detection of hemorrhages was verified using a quantitative comparison to the available histology pictures (Chapter 2). The fundamental novelty of this study is targeting intra-plaque hemorrhages rather than lipid as in other PA studies on carotid imaging [50], [69], [71], [76], [86], [90], [162]. Towards clinical use of PA for carotid imaging, the findings of Chapter 2 are promising: especially when considering the clinical significance of intra-plaque hemorrhages in plaque progression and vulnerability. However, the methods used in this study are still purely experimental. In *in vivo* clinical imaging, it will not be possible to obtain data from all angles. Therefore, the performance improvements of PAI were examined for the limited range of measurement angles that would be available *in vivo* (Chapter 3).

In the worst-case scenario, where the *in vivo* conditions are mimicked with an optically turbid surrounding medium and porcine blood-filled lumen, the SNR and CNR of PA images showed a 7 dB increase with spatial compounding. The depth at which compounding could still be effective was found to be approximately 2 cm in the case of the optically turbid surrounding medium. Beyond 2 cm depth, the initial SNR of the absorbers in the phantoms was not sufficient for spatial compounding. Additionally, the absorption of light by the luminal blood, and/or the presence of calcified plaques in the proximal wall, would also hamper the PA generation in the distal wall.

One of the critical steps in compounding is the registration of data to the correct geometrical reference. This was trivial for the experimental study (Chapter 3), where motorized stages precisely controlled the position of the probe and the rotation of the sample. Even with the rigid experimental setup, drastic changes in the compounded image quality were observed when the mismatch in the center of rotation was only a few pixels. For prospective clinical experiments, hand-held use of the probe is targeted. In that case, the orientation of the probe should be tracked precisely and accurately using, for instance, additional sensor technology such as gyroscopic sensors or accelerometers. Moreover, the probe position can be externally tracked using optical or magnetic sensors to achieve more accurate compounding during hand-held use. Final mismatches may be corrected by using image analysis techniques such as image registration and feature matching.

The presence of intra-plaque hemorrhage is vital, however, from the clinical point of view, the complete morphology is required to assess plaque vulnerability. A multi-wavelength approach was used to add more information to the morphology assessment. Additional to the 808 nm wavelength, 915, 940, 980 nm wavelength laser sources were added to the system to acquire multi-spectral PA data. Next, blind-source spectral unmixing based on independent component analysis (ICA) method was adopted to capture independent signatures of different composition of plaque samples.

The blind-source separation technique is advantageous as compared to fitting based methods as it does not require prior spectral knowledge. This is important since the composition of plaque tissue is complex and varies significantly between patients. Therefore, the optical absorption spectra of pure chromophores such as hemoglobin and lipids may not always resemble the actual absorption in real tissue. However, this advantage leads to a random order in the resultant unmixed components. Therefore a benchmarking phantom study was performed to match the unmixed components with the known materials. This approach led to overcome the limitation of randomness and demonstrated promising results for plaque morphology assessment in future clinical studies. The histological examination further verified the consistent match between the results of plaque samples and phantom.

In most studies found in literature, new techniques such as PAI are often tested in custom-made, tissue-mimicking phantoms. In this thesis, experimental PAI was applied to both phantoms and plaque samples, revealing promising results. The design and production of more realistic phantoms are both cumbersome. Investigating multiple parameters requires a high number of different phantom designs and verification experiments. Therefore, we aimed to design a digital phantom and simulation tool-chain that simulates PA from optics to acoustics. With this, we aimed to simulate realistic *in vivo* scenarios and reproduce possible artifacts such as clutter artifact sources in carotid plaque images. We adopted a mesh-based Monte-Carlo simulation tool for optical photon distribution simulation and coupled the output to the acoustic simulation of the k-Wave Toolbox.

The benefit of this platform is that it allows simulations of complex geometries as opposed to simplified layered simulations. Although the platform requires further development at this stage, it would ultimately start with an existing CT or MR image of a patient that will undergo endarterectomy as input, then simulating the US and PA images that would be acquired *in vivo* or *in vitro* as shown in the previous chapters. This would serve as validation of the PA images acquired, but would also give more insights into the specific patterns or spectral information that fatty streaks or other lesions would add to the image data acquired. Moreover, it would provide data that can be used to test and verify new image processing or filtering techniques.

6.1 General Limitations

Photoacoustic imaging (PAI) has advanced in the last decade, and the collective scientific knowledge and output on PAI have grown exponentially. The *ex vivo* studies in this thesis explored new directions in handheld, integrated PAI technology, and provided a better understanding of the use of PA for carotid plaque imaging. This aims to facilitate PAI towards the clinic. However, regarding plaque imaging with PA, there are still some challenges to overcome before making clinical *in vivo* imaging a reality.

The wavelengths used in this thesis were limited to the available wavelengths in the PA probe that was designed and build as part of the FULLPHASE project (EU FP7

Programme) and consortium. This also limits the number of tissue components that are activated during PAI. Unfortunately, the optimal wavelengths for lipid detection (1200 and 1700 nm) were beyond the available range [163]. A better unmixing performance, when considering both hemorrhage and lipid detection, can be obtained by using more specific wavelengths for lipids. The use of more wavelengths, in general, would improve the unmixing results. However, this would lead to a non-handheld, high-cost system, which would hamper the introduction of the technique in the clinical setting.

Secondly, the mechanism of PA generation leads to a wide-band signal that propagates in 3-D in contrast to pulse-echo ultrasound, where US waves are emitted in the imaging plane with the bandwidth of the transducer and the secondary reflections are neglected in conventional medical US. Therefore, wide-band transducers specific to the PA application would provide better imaging performance. Additionally, the use of a linear array transducer for acquisition leads to a limited spatial sampling and leads to artifacts in the images due to band-limited data. Considering the fact that the actual PA signals propagate in 3-D, a concave hemispherical transducer as reported by Dima et al. [74] would be a solution to this problem. Alternatively, the use of 2-D matrix arrays can circumvent the issue of limited spatial sampling with the aid of synthetic apertures. This would also be a solution to reduce out-of-plane clutter artifacts since matrix arrays allow the reconstruction to be applied in 3-D.

Regarding the verification of morphology assessment by multispectral PAI, multiple histologic staining is needed to be done additional to Masson's trichrome, which was chosen based on previous MRI studies [164]–[166]. This would increase the specificity of the histological morphology identification.

The *ex vivo* experiments described in this thesis were performed mostly in water (transparent PBS solution). Although some preliminary analysis was performed in the presence of the surrounding medium in Chapter 3, a more elaborate study should be performed to test the penetration depth and potential to increase the achievable depth *in vivo*. Additional to the turbid surrounding medium, the presence of blood in the lumen, which highly absorbs light, affects the penetration depth. Although we showed the effect of luminal blood in a PVA phantom experiment in Chapter 3, no experiments were performed on the effects of blood filled lumen in

the endarterectomy samples. This requires perfectly intact leakage-free samples so that blood can be pumped through the lumen during immersion, which will make experiments more challenging.

Measurements were performed in static conditions, where in the *in vivo* case the artery would be pulsating. Even though the endarterectomy samples are highly calcified and significantly lost their elastic properties, there will be still motion which will limit the temporal averaging and reduce the SNR of PA images. In the setup proposed, pressurization of intact samples is feasible and a recommendation for future research.

Finally, in the scope of this thesis, there is no comparison of PA images of carotid samples with other imaging modalities which are commonly used in the clinic, such as CT, MRI, and US (elastography and contrast-enhanced US). For a clinically viable verification of PAI, comparing the imaging performance to the gold standard methods is essential.

6.2 Outlook

The performance of PA highly depends on the optical energy delivered to the targeted absorber. Therefore, the performance may drastically be affected by high body-mass in elderly patients, and the shade of a subject's skin color. This also raises an ethical concern toward the widespread use of PA in the clinic. The photon energy delivered to the carotid artery should be significantly higher for more efficient generation of photoacoustic waves and higher SNR images. Within the safety limits of the allowed laser energy and skin illumination, this is still challenging. The primary energy loss occurs at the skin interface due to high absorption and backscattering of photons. Therefore, alternative illumination methods might increase the effective light energy delivered to carotid. One alternative can be delivering light subcutaneously via needle-tip fiber patches. As subcutaneous drug delivery patches are available [167], [168], the know-how can be transferred, and the approach can be adopted for fiber light delivery. Although this would render the procedure to be minimally invasive instead of non-invasive, it is likely to reduce inter-subject variability with respect to imaging performance.

Beyond all the technical challenges, the physiological conditions *in vivo*, such as pulsation of the artery, might cause blurring or loss of signals, especially when significant temporal averaging is required to improve SNR. Therefore, a new reconstruction approach should be developed for moving structures in combination with pulse-echo ultrasound, for instance by combining US-based motion tracking with interleaved PA acquisitions [169], [170].

Isolating potential causes of artifacts is beneficial to develop a systematic understanding of the capabilities and the limitations of the imaging technique. Similarly, more realistic experiments can be performed by adding the complexity in a controlled way. The first step should be an analysis of the motion during pulsation of the artery. To achieve this, the experimental approach of plaque elastography studies can be adopted [171]. Next, the same luminal pressurization experiment should be repeated with the porcine blood instead of PBS solution to see the effect of blood in the lumen on PA signal. Next, the optically scattering surrounding medium should be added during *ex vivo* experiments. This can be achieved by embedding endarterectomy samples in a block of agar or a gelatin phantom. However, since those gels solidify around 40°C, this can damage the tissue due to heat. More easily, Intralipid solutions of different concentrations can mimic the optical scattering of the surrounding medium. Finally, the effect of the surrounding medium can be investigated with pre/peri/post-operative PA images of the patients. The ethical approval for patient studies with the existing PA system has already been obtained. Imaging patients that will undergo an endarterectomy surgery can be imaged prior to the surgery, during the surgery with an open neck, and, lastly, the *ex vivo* measurement with the obtained sample can be performed in the lab. This will provide a comprehensive data to gain insight regarding the challenges introduced *in vivo* and overall feasibility of the technique.

Eventually, the clinical relevance and added value for plaque characterization would be high once all the aforementioned challenges are minimized. Combining the simulation tool-chain, which was discussed in Chapter 5, with the experiments with rather realistic conditions, we believe that the challenges of *in vivo* PA imaging can be characterized and innovative solutions to those challenges can be introduced more easily.

Once those steps are taken towards *in vivo*, then the next step will be to conduct clinical research studies with a larger population to validate the technique and compare the findings to other imaging modalities, to show that photoacoustics actually introduces a benefit for the clinician and the patient. Achieving this would affect the decision criteria for endarterectomy and lead to changes in the medical guidelines. Ultimately, detecting the morphology of carotid plaques may yield a reduction in the risk of stroke and minimize the obvious overtreatment in present-day medicine.

The popularity of PAI vastly increased since the 2000s, and in approximately two decades achieved significant improvements. Considering the reputation of the field, I envision further achievements in the upcoming decade and believe that PAI will start entering clinics for disease diagnosis, including carotid plaques.

Curriculum Vitae

Mustafa Ümit Arabul was born in Istanbul, Turkey in 1988. He received the B.Sc. degree (2011) in electrical and electronics engineering from the Middle East Technical University (METU), Ankara, Turkey. He received his minor specializations in Control Engineering & Biomedical Engineering. Upon graduation, he joined the Medical Imaging Lab. in the Institute of Biomedical Engineering, Bogaziçi University (BOUN), Istanbul, Turkey. He worked on a photoacoustic microscopy project, where he designed and build a custom-made microscopy system, and he received the M.Sc. degree in biomedical engineering in 2013. He pursued his Ph.D. in the Photoacoustics and Ultrasound Laboratory of Eindhoven (PULS/e Lab), in the Cardiovascular Biomechanics group of the department of Biomedical Engineering in the Eindhoven University of Technology, The Netherlands. His research focused on photoacoustic imaging of carotid arteries and fundamental characterization and preclinical validation of photoacoustic imaging. The studies conducted and reported in this thesis were performed as part of the FULLPHASE (2013-2016) and CVENT (2016-2018) projects, funded by the European Union (FP7 and H2020).



Acknowledgments

The PhD was the last steps of a long journey and I would like to express my deepest gratitude to my promoter prof. ir. Frans van de Vosse for offering me the opportunity to take those steps in his group. I would like to express my sincere thanks to my daily supervisor dr. ir. Richard Lopata, for all his contributions and guidance for me to become a better researcher. I would like to extend my sincere thanks to my second supervisor dr. ir. Marcel Rutten for his support and supervision, also for his precious help in designing and building experiment setups. Additionally, the completion of this dissertation would not have been possible without the support of our medical collaborator Marc van Sambeek. Many thanks for valuing scientific research and providing us with all the samples used in this thesis.

I am also grateful to my thesis committee members, prof. Peter Hilbers, prof. ir. Chris de Korte, prof. Georg Schmitz, and prof. ir. Menno Prins. Thank you for carefully reviewing this dissertation.

I would like to express my special thanks to my project collaborators dr. Michael Jaeger, dr. Martin Beckman, Hans-Martin Schwab, dr. Khalid Daoudi, dr. Mithun Kuniyil Ajith Singh, dr. Pim van den Berg in the FULLPHASE and CVENT projects. Especially at the beginning of my PhD, I learned a lot from our discussions in the meetings. I must also thank to the work-package leaders, prof. Wiendelt Steenberg, prof. Martin Frenz, prof. Georg Schmitz, prof. Pierre Boutouyrie and all industrial partners, especially Celine Canal, Olivier Rabot, David Sontrop, Theo Mulder. Finally, I would like to extend my special thanks to dr. Peter Brands for facilitating this research through his leadership in both projects.

I had a great pleasure working with Maarten Heres, my project and office colleague, thank you. I very much appreciate the efforts of Louise Gouteux and dr. Min Wu in the PA experiments.

Thanks should also go to the other PULS/e Lab members, Niels Petterson, Emiel van Disseldorp, Joerik Ruijter, Louis Fixsen, Marloes Sjoerdsma, and Cristina Caresio for their invaluable discussions about my research, and Roy van Hees, who will continue the research where I finished. As my paranymphs, Niels and Joerik deserves special thanks for their precious support during my defense and graduation.

I cannot omit my office mates Rob Driessen, Eline van Haaften, Jibbe Soetens, Nicole van Engeland, Kujtim Gashi, and Stefan Heinen, as well as the people in neighboring offices: Ashley Heuijerjans, Tommaso Ristori, Johanna Melke, Tilai Rosalina, Andres Arias, Lorenza Henao, Nicole van Gestel, Willeke Traa, and Mathieu van Kelle. Thank you for making last 5 years full of joy.

Special thanks to Mascha Maenhout for being very helpful and nice to us and making everything easier for all the PhDs while taking charge of the lab. Our mechanic designer Jurgen Bulsink, thank you for your contribution, and enthusiasm. Every lab should have a mechanic like you! And finally, our secretary Alice van Litsenburg, thank you for your relentless assistance.

I am deeply indebted to my MSc supervisor prof. Cengizhan Ozturk and especially co-supervisor prof. Burcin Unlu for nurturing me in the field of photoacoustics. I also gratefully acknowledge the support and expertise of my colleagues Dr. Hakan Erkol, Dr. Seydi Yavas during my master's study.

I would like to extend my gratitude to all my teachers in Uskudar Science High School especially my physics teacher Berran Karsli and my biology teacher Yasemin Senkal. I would like to convey special thanks to my commuting friend Cem Bozkus for our inspiring and encouraging discussions about science and technology.

The people of "Ataristan - *the Anger-land*" and the Gezi Solidarity NL, all my friends from Turkey living (or lived in last five years) in the Netherlands, thank you for making Eindhoven feel like home to me! I would like to recall the names of Erkan,

Makbule, Banu, Oktay, Abidin, Gizem, Seda and finally our sole native Dutch friend Kubilay. Thank you all for your warmth, sincerity and friendship.

My beloved class-mate, my dear friend (dostum) Yağız Aksoy, thanks for your "spiritual" support and enjoyable visits to Eindhoven.

Here I also want to thank my family in my mother-tongue.

Vakıf dostlarım! Ankara'da başlayan 10 yılı aşkın dostluğumuz için tüm Dostluk Yardımlaşma Vakfı dostlarıma teşekkür ediyorum. Vakıfta birlikte yaptığımız mesleğime, bilime, insanlığa dair sorgulamalar neticesinde bugün doktoramı tamamlıyorum. Bu dostluğun kazandırdıkları hep daim olacaktır.

Bu doktora tezinin yazılmasına kadar süreçte eğitim hayatımın ta en başından bugüne kadar beni destekleyen, bana güvenen ve benimle gurur duyan, sevgisini her daim gösteren ve hissettiren anneme, babama ablalarım Derya ve Arzu'ya en içten teşekkürlerimi, minnetlerimi ve kucak dolusu sevgilerimi sunuyorum. Ayrıca, yeğenlerim Çağan, Beren ve Simay'ın hasretlerini de anmadan geçemeyeceğim. Bu teze biraz da onların özlemi sindi.

Son olarak hayat yoldaşım Demet... Bu tezin yarısı da senin emeğin, desteğin, fedakarlığın ve en güzeli de sevgin. Çok güzel anılar biriktirdiğimiz yolculuğumuzda bir de bu tezin yazıldığı 5 yılı biriktirdik Hollanda'da. Daha nicelerini biriktirmek için yan yana olacağımız için mutluyum. Aşkla, sevgiyle kucaklıyor ve teşekkür ediyorum.

List of Publications

Peer-Reviewed Journal Publications

1. M. U. Arabul, M. C. M. Rutten, M. R. H. M. van Sambeek, F. N. van de Vosse, and R. G. P. Lopata, "Photoacoustic simulation tool-chain for 3-D simulations of heterogeneous media," [In Preparation].
2. M. U. Arabul, M. C. M. Rutten, M. R. H. M. van Sambeek, F. N. van de Vosse, and R. G. P. Lopata, "Unmixing multi-spectral photoacoustic sources in human carotid plaques using non-negative independent component analysis," *Photoacoustics*, [Under Review].
3. M. U. Arabul, H. M. Heres, M. C. M. Rutten, M. R. H. M. van Sambeek, F. N. van de Vosse, and R. G. P. Lopata, "Investigation on the Effect of Spatial Compounding on Photoacoustic Images of Carotid Plaques in the *In vivo* Available Rotational Range," *IEEE Trans. Ultrason. Ferroelectr. Freq. Control*, vol. 65, no. 3, pp. 440–447, Mar. 2018.
4. M. U. Arabul, M. Heres, M. C. M. Rutten, M. R. van Sambeek, F. N. van de Vosse, and R. G. P. Lopata, "Toward the detection of intraplaque hemorrhage in carotid artery lesions using photoacoustic imaging," *J. Biomed. Opt.*, vol. 22, no. 4, p. 041010, Dec. 2016.
5. H. M. Heres, M. U. Arabul, M. C. M. Rutten, F. N. van de Vosse, and R. G. P.

Lopata, "Visualization of vasculature using a hand-held photoacoustic probe: phantom and *in vivo* validation," *J. Biomed. Opt.*, vol. 22, no. 4, p. 041013, Jan. 2017.

Conference Publications

1. M. U. Arabul, M. Rutten, M. van Sambeek, F. van de Vosse, and R. Lopata, "Multi-spectral photoacoustic morphology assessment of human carotid plaques using blind spectral unmixing and histologic validation," *2018 IEEE International Ultrasonics Symposium (IUS)*, Kobe, Japan.
2. M. U. Arabul, M. Heres, M. Rutten, M. van Sambeek, F. van de Vosse, and R. Lopata, "Characterization of human carotid plaques using multi-wavelength photoacoustic imaging," *2017 IEEE International Ultrasonics Symposium (IUS)*, Washington, DC, 2017, pp. 1-1.
3. L. Gouteux, Ü. Arabul, M. Rutten, F. van de Vosse, and R. Lopata, "Hemorrhages detection in atherosclerotic plaques using ultrasound and photoacoustic, phantom study," *2017 IEEE International Ultrasonics Symposium (IUS)*, Washington, DC, 2017, pp. 1-1.
4. M. U. Arabul, H. M. Heres, M. C. M. Rutten, M. R. H. M. van Sambeek, F. N. van de Vosse, and R. G. P. Lopata, "Investigation of the effects of multi-angle compounding in photoacoustic imaging," *2016 IEEE International Ultrasonics Symposium (IUS)*, Tours, 2016, pp. 1-3.
5. M. U. Arabul, H. M. Heres, M. C. M. Rutten, M. R. H. M. van Sambeek, F. N. van de Vosse, and R. G. P. Lopata, "Ex vivo photoacoustic imaging of atherosclerotic carotid plaques," *2015 IEEE International Ultrasonics Symposium (IUS)*, Taipei, 2015, pp. 1-4.
6. M. U. Arabul, H. M. Heres, M. Rutten, F. van de Vosse, and R. Lopata, "Optical absorbance measurements and photoacoustic evaluation of freeze-thawed polyvinyl-alcohol vessel phantoms," *Proc. SPIE 9323, Photons Plus Ultrasound:*

Imaging and Sensing 2015, 93232M, 2015.

7. H. M. Heres, M. Ü. Arabul, B. Tchang, F. N. van de Vosse, M. C. M. Rutten, and R. G. P. Lopata, "Photoacoustic perfusion measurements: a comparison with power Doppler in phantoms," *Proc. SPIE 9323, Photons Plus Ultrasound: Imaging and Sensing 2015*, 932345, 2015.
8. M. U. Arabul, M. Rutten, F. van de Vosse, and R. Lopata, "Optical and acoustic characterization of freeze-thawed polyvinyl alcohol gels," *2014 IEEE International Ultrasonics Symposium (IUS)*, Chicago, IL, 2014, pp. 2410-2413.
9. S. Yavas, E. A. Kipergil, O. Akcaalan, Y. B. Eldeniz, M. U. Arabul, H. Erkol, M. B. Unlu, F. O. Ilday, "All-fiber nanosecond laser system generating super-continuum spectrum for photoacoustic imaging," *2013 Conference on Lasers Electro-Optics Europe International Quantum Electronics Conference CLEO EUROPE/IQEC*, 2013.
10. H. Erkol, E. Aytac-Kipergil, M. U. Arabul, and M. B. Unlu, "Analysis of laser parameters in the solution of photoacoustic wave equation," *Proc. SPIE 8581, Photons Plus Ultrasound: Imaging and Sensing 2013*, 858136, 2013.
11. S. Yavas, E. A. Kipergil, M. U. Arabul, H. Erkol, O. Akcaalan, Y. B. Eldeniz, F. O. Ilday, M. B. Unlu, "A novel fiber laser development for photoacoustic microscopy," *Proc. SPIE 8581, Photons Plus Ultrasound: Imaging and Sensing 2013*, 85813S, 2013.

Bibliography

- [1] S. Mendis, P. Puska, B. Norrving, W. H. Organization, W. H. Federation, and W. S. Organization, Eds., *Global Atlas on Cardiovascular Disease Prevention and Control*, OCLC: ocn756166722, Geneva: World Health Organization in collaboration with the World Heart Federation and the World Stroke Organization, 2011, 155 pp.
- [2] J. Biller, W. M. Feinberg, J. E. Castaldo, A. D. Whittemore, R. E. Harbaugh, R. J. Dempsey, L. R. Caplan, T. F. Kresowik, D. B. Matchar, J. F. Toole, J. D. Easton, H. P. Adams, L. M. Brass, R. W. H. Li, T. G. Brott, and L. Sternau, "Guidelines for Carotid Endarterectomy," *Circulation*, vol. 97, no. 5, pp. 501–509, 1998.
- [3] V. Aboyans, J.-B. Ricco, M.-L. E. Bartelink, M. Björck, M. Brodmann, T. Cohnert, J.-P. Collet, M. Czerny, M. De Carlo, S. Debus, C. Espinola-Klein, T. Kahan, S. Kownator, L. Mazzolai, A. R. Naylor, M. Roffi, J. Röther, M. Sprynger, M. Tendera, G. Tepe, M. Venermo, C. Vlachopoulos, I. Desormais, Document Reviewers, P. Widimsky, P. Kolh, S. Agewall, H. Bueno, A. Coca, G. J. De Borst, V. Delgado, F. Dick, C. Erol, M. Ferrini, S. Kakkos, H. A. Katus, J. Knuuti, J. Lindholt, H. Mattle, P. Pieniazek, M. F. Piepoli, D. Scheinert, H. Sievert, I. Simpson, J. Sulzenko, J. Tamargo, L. Tokgozoglu, A. Torbicki, N. Tsakountakis, J. Tuñón, M. V. de Ceniga, S. Windecker, and J. L. Zamorano, "Editor's Choice – 2017 ESC Guidelines on the Diagnosis and Treatment of Peripheral Arterial Diseases, in collaboration with the European Society

-
- for Vascular Surgery (ESVS)," *European Journal of Vascular and Endovascular Surgery*, vol. 55, no. 3, pp. 305–368, Mar. 2018.
- [4] P. Rothwell and C. Warlow, "Prediction of benefit from carotid endarterectomy in individual patients: A risk-modelling study," *The Lancet*, vol. 353, no. 9170, pp. 2105–2110, Jun. 1999.
- [5] M. J. Davies, P. D. Richardson, N. Woolf, D. R. Katz, and J. Mann, "Risk of thrombosis in human atherosclerotic plaques: Role of extracellular lipid, macrophage, and smooth muscle cell content," *Heart*, vol. 69, no. 5, pp. 377–381, May 1, 1993.
- [6] H. Huang, R. Virmani, H. Younis, A. P. Burke, R. D. Kamm, and R. T. Lee, "The Impact of Calcification on the Biomechanical Stability of Atherosclerotic Plaques," *Circulation*, vol. 103, no. 8, pp. 1051–1056, Feb. 27, 2001.
- [7] R. Virmani, A. P. Burke, A. Farb, and F. D. Kolodgie, "Pathology of the Vulnerable Plaque," *Journal of the American College of Cardiology*, Detection of Vulnerable Plaques, vol. 47, pp. C13–C18, 8, Supplement Apr. 18, 2006.
- [8] M. Naghavi, "From Vulnerable Plaque to Vulnerable Patient: A Call for New Definitions and Risk Assessment Strategies: Part I," *Circulation*, vol. 108, no. 14, pp. 1664–1672, Oct. 7, 2003.
- [9] A. V. Finn, M. Nakano, J. Narula, F. D. Kolodgie, and R. Virmani, "Concept of Vulnerable/Unstable Plaque," *Arteriosclerosis, Thrombosis, and Vascular Biology*, vol. 30, no. 7, pp. 1282–1292, Jul. 1, 2010.
- [10] H. Sillesen and T. Nielsen, "Clinical Significance of Intraplaque Hemorrhage in Carotid Artery Disease," *Journal of Neuroimaging*, vol. 8, no. 1, pp. 15–19, Jan. 1, 1998.
- [11] F. D. Kolodgie, H. K. Gold, A. P. Burke, D. R. Fowler, H. S. Kruth, D. K. Weber, A. Farb, L. Guerrero, M. Hayase, R. Kutys, J. Narula, A. V. Finn, and R. Virmani, "Intraplaque Hemorrhage and Progression of Coronary Atheroma," *New England Journal of Medicine*, vol. 349, no. 24, pp. 2316–2325, Dec. 11, 2003.
- [12] N. Takaya, "Presence of Intraplaque Hemorrhage Stimulates Progression of Carotid Atherosclerotic Plaques: A High-Resolution Magnetic Resonance Imaging Study," *Circulation*, vol. 111, no. 21, pp. 2768–2775, May 31, 2005.

-
- [13] R. P. Choudhury, "MRI and Characterization of Atherosclerotic Plaque: Emerging Applications and Molecular Imaging," *Arteriosclerosis, Thrombosis, and Vascular Biology*, vol. 22, no. 7, pp. 1065–1074, Jul. 1, 2002.
 - [14] A. J. Young, "New technologies and general practice," *Br J Gen Pract*, vol. 66, no. 653, pp. 601–602, Dec. 1, 2016. pmid: 27884890.
 - [15] M. Goudelin, B. Evrard, F. Dalmay, A. H. Padilla, C. Gonzalez, T. Lafon, T. Daix, A.-L. Fedou, B. François, and P. Vignon, "Diagnostic capability of a next-generation, ultra-miniaturized ultrasound system in patients with cardiopulmonary compromise assessed using basic critical care echocardiography," *Intensive Care Medicine*, May 31, 2018.
 - [16] S. J. Nicholls, "Intravascular Ultrasound in Cardiovascular Medicine," *Circulation*, vol. 114, no. 4, e55–e59, Jul. 25, 2006.
 - [17] R. Puri, M. I. Worthley, and S. J. Nicholls, "Intravascular imaging of vulnerable coronary plaque: Current and future concepts," *Nature Reviews Cardiology*, vol. 8, no. 3, pp. 131–139, Mar. 2011.
 - [18] M. Tanter and M. Fink, "Ultrafast imaging in biomedical ultrasound," *IEEE Transactions on Ultrasonics, Ferroelectrics, and Frequency Control*, vol. 61, no. 1, pp. 102–119, Jan. 2014.
 - [19] M. A. Vannan, G. Pedrizzetti, P. Li, S. Gurudevan, H. Houle, J. Main, J. Jackson, and N. C. Nanda, "CASE REPORTS: Effect of Cardiac Resynchronization Therapy on Longitudinal and Circumferential Left Ventricular Mechanics by Velocity Vector Imaging: Description and Initial Clinical Application of a Novel Method Using High-Frame Rate B-Mode Echocardiographic Images," *Echocardiography*, vol. 22, no. 10, pp. 826–830, Nov. 1, 2005.
 - [20] S. Holbek, "3-D Vector Flow Imaging," Technical University of Denmark, Lyngby, Denmark, 2016.
 - [21] T. C. Gasser, R. W. Ogden, and G. A. Holzapfel, "Hyperelastic modelling of arterial layers with distributed collagen fibre orientations," *Journal of The Royal Society Interface*, vol. 3, no. 6, pp. 15–35, Feb. 22, 2006. pmid: 16849214.
 - [22] J. M. Clark and S. Glagov, "Transmural organization of the arterial media. The lamellar unit revisited," *Arteriosclerosis, Thrombosis, and Vascular Biology*, vol. 5, no. 1, pp. 19–34, Jan. 1, 1985.

-
- [23] E. N. Marieb, *Human Anatomy & Physiology*, 5th ed., ser. Pearson education; Pearson education book. San Francisco : Benjamin Cummings, 2001.
- [24] Blausen.com staff, "Medical gallery of Blausen Medical 2014," *WikiJournal of Medicine*, vol. 1, no. 2, Jan. 15, 2014.
- [25] W. G. Webb, "3 - Organization of the Nervous System II," in *Neurology for the Speech-Language Pathologist (Sixth Edition)*, W. G. Webb, Ed., Mosby, Jan. 1, 2017, pp. 44–73.
- [26] C. J. Pepine, "The effects of angiotensin-converting enzyme inhibition on endothelial dysfunction: Potential role in myocardial ischemia," *A Symposium: Endothelial Function and Cardiovascular Disease: Potential Mechanisms and Interventions*, vol. 82, S23–S27, 10, Supplement 1 Nov. 19, 1998.
- [27] D. Mozaffarian, E. J. Benjamin, A. S. Go, D. K. Arnett, M. J. Blaha, M. Cushman, S. de Ferranti, J.-P. Després, H. J. Fullerton, V. J. Howard, M. D. Huffman, S. E. Judd, B. M. Kissela, D. T. Lackland, J. H. Lichtman, L. D. Lisabeth, S. Liu, R. H. Mackey, D. B. Matchar, D. K. McGuire, E. R. Mohler, C. S. Moy, P. Muntner, M. E. Mussolino, K. Nasir, R. W. Neumar, G. Nichol, L. Palaniappan, D. K. Pandey, M. J. Reeves, C. J. Rodriguez, P. D. Sorlie, J. Stein, A. Towfighi, T. N. Turan, S. S. Virani, J. Z. Willey, D. Woo, R. W. Yeh, and M. B. Turner, "Heart Disease and Stroke Statistics—2015 Update: A Report From the American Heart Association," *Circulation*, vol. 131, no. 4, e29–e322, Jan. 27, 2015.
- [28] Fisher C, "Capsular infarcts: The underlying vascular lesions," *Archives of Neurology*, vol. 36, no. 2, pp. 65–73, Feb. 1, 1979.
- [29] C. M. Fisher, "Lacunes: Small, deep cerebral infarcts," *Neurology*, vol. 50, no. 4, p. 841, Apr. 1, 1998.
- [30] W. M. Blackshear, D. J. Phillips, P. M. Chikos, J. D. Harley, B. L. Thiele, and D. E. Strandness, "Carotid artery velocity patterns in normal and stenotic vessels," *Stroke*, vol. 11, no. 1, pp. 67–71, Jan. 1980.
- [31] R. A. Knox, P. J. Breslau, and D. E. Strandness, "A simple parameter for accurate detection of severe carotid disease," *British Journal of Surgery*, vol. 69, no. 4, pp. 230–233, Apr. 1, 1982.

- [32] E. G. Grant, C. B. Benson, G. L. Moneta, A. V. Alexandrov, J. D. Baker, E. I. Bluth, B. A. Carroll, M. Eliasziw, J. Gocke, B. S. Hertzberg, S. Katanick, L. Needleman, J. Pellerito, J. F. Polak, K. S. Rholl, D. L. Wooster, and R. E. Zierler, "Carotid Artery Stenosis: Gray-Scale and Doppler US Diagnosis—Society of Radiologists in Ultrasound Consensus Conference," *Radiology*, vol. 229, no. 2, pp. 340–346, Nov. 1, 2003.
- [33] "Randomised trial of endarterectomy for recently symptomatic carotid stenosis: Final results of the MRC European Carotid Surgery Trial (ECST)," *The Lancet*, vol. 351, no. 9113, pp. 1379–1387, May 1998.
- [34] W. Casscells, "Vulnerable Atherosclerotic Plaque: A Multifocal Disease," *Circulation*, vol. 107, no. 16, pp. 2072–2075, Apr. 29, 2003.
- [35] N. Nighoghossian, L. Derex, and P. Douek, "The Vulnerable Carotid Artery Plaque: Current Imaging Methods and New Perspectives," *Stroke*, vol. 36, no. 12, pp. 2764–2772, Dec. 1, 2005.
- [36] S. L. Jacques, "Optical properties of biological tissues: A review," *Physics in Medicine and Biology*, vol. 58, no. 11, R37–R61, Jun. 7, 2013.
- [37] D. A. Boas, D. H. Brooks, E. L. Miller, C. A. DiMarzio, M. Kilmer, R. J. Gaudette, and Q. Zhang, "Imaging the body with diffuse optical tomography," *IEEE Signal Processing Magazine*, vol. 18, no. 6, pp. 57–75, Nov. 2001.
- [38] H. Lei, L. A. Johnson, S. Liu, D. S. Moons, T. Ma, Q. Zhou, M. D. Rice, J. Ni, X. Wang, P. D. R. Higgins, and G. Xu, "Characterizing intestinal inflammation and fibrosis in Crohn's disease by photoacoustic imaging: Feasibility study," *Biomedical Optics Express*, vol. 7, no. 7, pp. 2837–2848, Jul. 1, 2016.
- [39] A. G. Bell, "The production of sound by radiant energy," *Science*, vol. os-2, no. 49, pp. 242–253, May 28, 1881. pmid: 17741736.
- [40] H. K. Wickramasinghe, R. C. Bray, V. Jipson, C. F. Quate, and J. R. Salcedo, "Photoacoustics on a microscopic scale," *Applied Physics Letters*, vol. 33, no. 11, pp. 923–925, Dec. 1, 1978.
- [41] G. Busse, "Imaging with the optoacoustic effect," *Optics & Laser Technology*, vol. 12, no. 3, pp. 149–154, Jun. 1980.
- [42] H. Coufal, U. Moller, and S. Schneider, "Photoacoustic imaging using a Fourier transform technique," *Applied Optics*, vol. 21, no. 13, p. 2339, Jul. 1, 1982.

-
- [43] Y. Zhou, J. Yao, and L. V. Wang, "Tutorial on photoacoustic tomography," *Journal of Biomedical Optics*, vol. 21, no. 6, p. 061 007, Apr. 18, 2016.
- [44] C. G. A. Hoelen and F. F. M. de Mul, "A new theoretical approach to photoacoustic signal generation," *The Journal of the Acoustical Society of America*, vol. 106, no. 2, pp. 695–706, Aug. 1999.
- [45] H. Erkol, E. Aytac-Kipergil, M. U. Arabul, and M. B. Unlu, "Analysis of laser parameters in the solution of photoacoustic wave equation," A. A. Oraevsky and L. V. Wang, Eds., Mar. 4, 2013, p. 858 136.
- [46] X. L. Dean-Ben, A. Buehler, V. Ntziachristos, and D. Razansky, "Accurate Model-Based Reconstruction Algorithm for Three-Dimensional Optoacoustic Tomography," *IEEE Transactions on Medical Imaging*, vol. 31, no. 10, pp. 1922–1928, Oct. 2012.
- [47] M. Jaeger, S. Schüpbach, A. Gertsch, M. Kitz, and M. Frenz, "Fourier reconstruction in optoacoustic imaging using truncated regularized inverse k -space interpolation," *Inverse Problems*, vol. 23, no. 6, S51–S63, Dec. 1, 2007.
- [48] L. V. Wang, "Tutorial on Photoacoustic Microscopy and Computed Tomography," *IEEE Journal of Selected Topics in Quantum Electronics*, vol. 14, no. 1, pp. 171–179, 2008.
- [49] P. Beard, "Biomedical photoacoustic imaging," *Interface Focus*, vol. 1, no. 4, pp. 602–631, Aug. 6, 2011.
- [50] A. Rosenthal, F. A. Jaffer, and V. Ntziachristos, "Intravascular multispectral optoacoustic tomography of atherosclerosis: Prospects and challenges," *Imaging in Medicine*, vol. 4, no. 3, pp. 299–310, Jun. 2012.
- [51] V. Ntziachristos, "Emerging optoacoustic methods in bio-optics," *Journal of Biophotonics*, vol. 6, no. 6-7, pp. 473–474, Jun. 2013.
- [52] A. Taruttis and V. Ntziachristos, "Advances in real-time multispectral optoacoustic imaging and its applications," *Nature Photonics*, vol. 9, no. 4, pp. 219–227, Apr. 2015.
- [53] E. M. Strohmer, M. J. Moore, and M. C. Kolios, "Single Cell Photoacoustic Microscopy: A Review," *IEEE Journal of Selected Topics in Quantum Electronics*, vol. 22, no. 3, pp. 137–151, May 2016.

- [54] E. M. Strohman, M. J. Moore, and M. C. Kolios, "High resolution ultrasound and photoacoustic imaging of single cells," *Photoacoustics*, vol. 4, no. 1, pp. 36–42, Mar. 1, 2016.
- [55] C. Kim, C. Favazza, and L. V. Wang, "In Vivo Photoacoustic Tomography of Chemicals: High-Resolution Functional and Molecular Optical Imaging at New Depths," *Chemical Reviews*, vol. 110, no. 5, pp. 2756–2782, May 12, 2010.
- [56] D. Razansky, N. J. Harlaar, J. L. Hillebrands, A. Taruttis, E. Herzog, C. J. Zeebregts, G. M. van Dam, and V. Ntziachristos, "Multispectral Photoacoustic Tomography of Matrix Metalloproteinase Activity in Vulnerable Human Carotid Plaques," *Molecular Imaging and Biology*, vol. 14, no. 3, pp. 277–285, Jun. 2012.
- [57] K. Pu, A. J. Shuhendler, J. V. Jokerst, J. Mei, S. S. Gambhir, Z. Bao, and J. Rao, "Semiconducting polymer nanoparticles as photoacoustic molecular imaging probes in living mice," *Nature Nanotechnology*, vol. 9, no. 3, pp. 233–239, Mar. 2014.
- [58] S. Manohar, C. Ungureanu, and T. G. V. Leeuwen, "Gold nanorods as molecular contrast agents in photoacoustic imaging: The promises and the caveats," *Contrast Media & Molecular Imaging*, vol. 6, no. 5, pp. 389–400, Sep. 1, 2011.
- [59] S. Hu and L. V. Wang, "Photoacoustic imaging and characterization of the microvasculature," *Journal of Biomedical Optics*, vol. 15, no. 1, p. 011 101, 2010.
- [60] Y. Lao, D. Xing, S. Yang, and L. Xiang, "Noninvasive photoacoustic imaging of the developing vasculature during early tumor growth," *Physics in Medicine and Biology*, vol. 53, no. 15, pp. 4203–4212, Aug. 7, 2008.
- [61] J. Laufer, P. Johnson, E. Zhang, B. Treeby, B. Cox, B. Pedley, and P. Beard, "In vivo preclinical photoacoustic imaging of tumor vasculature development and therapy," *Journal of Biomedical Optics*, vol. 17, no. 5, p. 056 016, 2012.
- [62] S. Manohar, A. Kharine, J. C. G. van Hespén, W. Steenbergen, and T. G. van Leeuwen, "The Twente Photoacoustic Mammoscope: System overview and performance," *Physics in Medicine and Biology*, vol. 50, no. 11, pp. 2543–2557, Jun. 7, 2005.

-
- [63] J. J. Niederhauser, M. Jaeger, R. Lemor, P. Weber, and M. Frenz, "Combined ultrasound and optoacoustic system for real-time high-contrast vascular imaging in vivo," *IEEE Transactions on Medical Imaging*, vol. 24, no. 4, pp. 436–440, Apr. 2005.
- [64] G. Xu, J. R. Rajian, G. Girish, M. J. Kaplan, J. B. Fowlkes, P. L. Carson, and X. Wang, "Photoacoustic and ultrasound dual-modality imaging of human peripheral joints," *Journal of Biomedical Optics*, vol. 18, no. 1, p. 010 502, Dec. 2012.
- [65] P. J. van den Berg, K. Daoudi, H. J. Bernelot Moens, and W. Steenbergen, "Feasibility of photoacoustic/ultrasound imaging of synovitis in finger joints using a point-of-care system," *Photoacoustics*, vol. 8, pp. 8–14, Dec. 2017.
- [66] K. Maslov, H. F. Zhang, and L. V. Wang, "Effects of wavelength-dependent fluence attenuation on the noninvasive photoacoustic imaging of hemoglobin oxygen saturation in subcutaneous vasculature *in vivo*," *Inverse Problems*, vol. 23, no. 6, S113–S122, Dec. 1, 2007.
- [67] E. Z. Zhang, J. G. Laufer, R. B. Pedley, and P. C. Beard, "In Vivo high-resolution 3D photoacoustic imaging of superficial vascular anatomy," *Physics in Medicine and Biology*, vol. 54, no. 4, pp. 1035–1046, Feb. 21, 2009.
- [68] H. M. Heres, M. U. Arabul, M. C. M. Rutten, F. N. Van de Vosse, and R. G. P. Lopata, "Visualization of vasculature using a hand-held photoacoustic probe: Phantom and *in vivo* validation," *Journal of Biomedical Optics*, vol. 22, no. 4, p. 041 013, Jan. 24, 2017.
- [69] K. Jansen, M. Wu, A. F. van der Steen, and G. van Soest, "Photoacoustic imaging of human coronary atherosclerosis in two spectral bands," *Photoacoustics*, vol. 2, no. 1, pp. 12–20, Mar. 2014.
- [70] M. Wu, K. Jansen, A. F. W. van der Steen, and G. van Soest, "Specific imaging of atherosclerotic plaque lipids with two-wavelength intravascular photoacoustics," *Biomedical Optics Express*, vol. 6, no. 9, p. 3276, Sep. 1, 2015.
- [71] M. Wu, G. Springeling, M. Lovrak, F. Mastik, S. Iskander-Rizk, T. Wang, H. M. M. van Beusekom, A. F. W. van der Steen, and G. Van Soest, "Real-time volumetric lipid imaging in vivo by intravascular photoacoustics at 20 frames per second," *Biomedical Optics Express*, vol. 8, no. 2, p. 943, Feb. 1, 2017.

- [72] B. Wang, E. Yantsen, T. Larson, A. B. Karpouk, S. Sethuraman, J. L. Su, K. Sokolov, and S. Y. Emelianov, "Plasmonic Intravascular Photoacoustic Imaging for Detection of Macrophages in Atherosclerotic Plaques," *Nano Letters*, vol. 9, no. 6, pp. 2212–2217, Jun. 10, 2009.
- [73] B. Wang, P. Joshi, V. Sapozhnikova, J. Amirian, S. H. Litovsky, R. Smalling, K. Sokolov, and S. Emelianov, "Intravascular photoacoustic imaging of macrophages using molecularly targeted gold nanoparticles," in *Photons Plus Ultrasound: Imaging and Sensing 2010*, vol. 7564, International Society for Optics and Photonics, Feb. 23, 2010, 75640A.
- [74] A. Dima and V. Ntziachristos, "Non-invasive carotid imaging using optoacoustic tomography," *Optics Express*, vol. 20, no. 22, p. 25 044, Oct. 22, 2012.
- [75] E. Merčep, X. L. Deán-Ben, and D. Razansky, "Imaging of blood flow and oxygen state with a multi-segment optoacoustic ultrasound array," *Photoacoustics*, vol. 10, pp. 48–53, Jun. 1, 2018.
- [76] P. Kruizinga, A. F. W. van der Steen, N. de Jong, G. Springeling, J. L. Robertus, A. van der Lugt, and G. van Soest, "Photoacoustic imaging of carotid artery atherosclerosis," *Journal of Biomedical Optics*, vol. 19, no. 11, p. 110 504, Nov. 21, 2014.
- [77] S. Chaturvedi, A. Bruno, T. Feasby, R. Holloway, O. Benavente, S. N. Cohen, R. Cote, D. Hess, J. Saver, J. D. Spence, B. Stern, and J. Wilterdink, "Carotid endarterectomy—An evidence-based review: Report of the Therapeutics and Technology Assessment Subcommittee of the American Academy of Neurology," *Neurology*, vol. 65, no. 6, pp. 794–801, Sep. 27, 2005.
- [78] S. E. Clarke, R. R. Hammond, J. R. Mitchell, and B. K. Rutt, "Quantitative assessment of carotid plaque composition using multicontrast MRI and registered histology," *Magnetic Resonance in Medicine*, vol. 50, no. 6, pp. 1199–1208, Dec. 2003.
- [79] B. Chu, "Hemorrhage in the Atherosclerotic Carotid Plaque: A High-Resolution MRI Study," *Stroke*, vol. 35, no. 5, pp. 1079–1084, Apr. 1, 2004.
- [80] S. Fabiano, S. Mancino, M. Stefanini, M. Chiocchi, A. Mauriello, L. G. Spagnoli, and G. Simonetti, "High-resolution multicontrast-weighted MR imaging from human carotid endarterectomy specimens to assess carotid plaque components," *European Radiology*, vol. 18, no. 12, pp. 2912–2921, Dec. 2008.

-
- [81] L. J. Walker, A. Ismail, W. McMeekin, D. Lambert, A. D. Mendelow, and D. Birchall, "Computed Tomography Angiography for the Evaluation of Carotid Atherosclerotic Plaque: Correlation With Histopathology of Endarterectomy Specimens," *Stroke*, vol. 33, no. 4, pp. 977–981, Apr. 1, 2002.
- [82] T. T. de Weert, "In Vivo Characterization and Quantification of Atherosclerotic Carotid Plaque Components With Multidetector Computed Tomography and Histopathological Correlation," *Arteriosclerosis, Thrombosis, and Vascular Biology*, vol. 26, no. 10, pp. 2366–2372, Oct. 1, 2006.
- [83] M. J. C. van Gemert, R. Verdaasdonk, E. G. Stassen, G. A. C. M. Schets, G. H. M. Gijbbers, and J. J. Bonnier, "Optical properties of human blood vessel wall and plaque," *Lasers in Surgery and Medicine*, vol. 5, no. 3, pp. 235–237, 1985.
- [84] S. A. Prahl, M. J. C. van Gemert, and A. J. Welch, "Determining the optical properties of turbid media by using the adding–doubling method," *Applied Optics*, vol. 32, no. 4, p. 559, Feb. 1, 1993.
- [85] D. Wang, Y. Chen, and J. T. C. Liu, "A liquid optical phantom with tissue-like heterogeneities for confocal microscopy," *Biomedical Optics Express*, vol. 3, no. 12, p. 3153, Dec. 1, 2012.
- [86] S. Sethuraman, S. Mallidi, S. R. Aglyamov, J. H. Amirian, S. Litovsky, R. W. Smalling, and S. Y. Emelianov, "Intravascular photoacoustic imaging of atherosclerotic plaques: Ex-vivo study using a rabbit model of atherosclerosis," A. A. Oraevsky and L. V. Wang, Eds., Feb. 8, 2007, p. 643 729.
- [87] S. Sethuraman, S. R. Aglyamov, R. W. Smalling, and S. Y. Emelianov, "Remote Temperature Estimation in Intravascular Photoacoustic Imaging," *Ultrasound in Medicine & Biology*, vol. 34, no. 2, pp. 299–308, Feb. 2008.
- [88] Bo Wang, J. L. Su, A. B. Karpouk, K. V. Sokolov, R. W. Smalling, and S. Y. Emelianov, "Intravascular Photoacoustic Imaging," *IEEE Journal of Selected Topics in Quantum Electronics*, vol. 16, no. 3, pp. 588–599, 2010.
- [89] B. Wang, A. Karpouk, D. Yeager, J. Amirian, S. Litovsky, R. Smalling, and S. Emelianov, "Intravascular photoacoustic imaging of lipid in atherosclerotic plaques in the presence of luminal blood," *Optics Letters*, vol. 37, no. 7, p. 1244, Apr. 1, 2012.

-
- [90] J. Zhang, S. Yang, X. Ji, Q. Zhou, and D. Xing, "Characterization of Lipid-Rich Aortic Plaques by Intravascular Photoacoustic Tomography," *Journal of the American College of Cardiology*, vol. 64, no. 4, pp. 385–390, Jul. 2014.
- [91] Y. Cao, J. Hui, A. Kole, P. Wang, Q. Yu, W. Chen, M. Sturek, and J.-X. Cheng, "High-sensitivity intravascular photoacoustic imaging of lipid-laden plaque with a collinear catheter design," *Scientific Reports*, vol. 6, no. 1, Jul. 2016.
- [92] P. R. Moreno, "Plaque Neovascularization Is Increased in Ruptured Atherosclerotic Lesions of Human Aorta: Implications for Plaque Vulnerability," *Circulation*, vol. 110, no. 14, pp. 2032–2038, Sep. 27, 2004.
- [93] J. Scott McNally, H.-C. Yoon, S.-E. Kim, K. K. Narra, M. S. McLaughlin, D. L. Parker, and G. S. Treiman, "Carotid MRI Detection of Intraplaque Hemorrhage at 3T and 1.5T: Carotid MRI Detection of Intraplaque Hemorrhage," *Journal of Neuroimaging*, vol. 25, no. 3, pp. 390–396, May 2015.
- [94] J. M. U-King-Im, A. J. Fox, R. I. Aviv, P. Howard, R. Yeung, A. R. Moody, and S. P. Symons, "Characterization of Carotid Plaque Hemorrhage: A CT Angiography and MR Intraplaque Hemorrhage Study," *Stroke*, vol. 41, no. 8, pp. 1623–1629, Aug. 1, 2010.
- [95] K. Daoudi, P. van den Berg, O. Rabot, A. Kohl, S. Tisserand, P. Brands, and W. Steenbergen, "Handheld probe integrating laser diode and ultrasound transducer array for ultrasound/photoacoustic dual modality imaging," *Optics Express*, vol. 22, no. 21, p. 26 365, Oct. 20, 2014.
- [96] S. Wijeyaratne, C. Abbott, and M. Gough, "A Modification to the Standard Technique for Carotid Endarterectomy Allowing Removal of Intact Endarterectomy Specimens: Implications for Research and Quality Control of Pre-operative Imaging," *European Journal of Vascular and Endovascular Surgery*, vol. 23, no. 4, pp. 370–371, Apr. 2002.
- [97] R. W. Boekhoven, R. G. Lopata, M. R. van Sambeek, F. N. van de Vosse, and M. C. Rutten, "A Novel Experimental Approach for Three-Dimensional Geometry Assessment of Calcified Human Stenotic Arteries in Vitro," *Ultrasound in Medicine & Biology*, vol. 39, no. 10, pp. 1875–1886, Oct. 2013.
- [98] M. Jaeger, K. Gashi, H. G. Akarçay, G. Held, S. Peeters, T. Petrosyan, S. Preisser, M. Gruenig, and M. Frenz, "Real-time clinical clutter reduction in combined

epi-optoacoustic and ultrasound imaging,” *Photonics & Lasers in Medicine*, vol. 3, no. 4, Jan. 1, 2014.

- [99] M. Kuniyil Ajith Singh and W. Steenbergen, “Photoacoustic-guided focused ultrasound (PAFUSion) for identifying reflection artifacts in photoacoustic imaging,” *Photoacoustics*, vol. 3, no. 4, pp. 123–131, Dec. 2015.
- [100] R. W. Boekhoven, M. C. Rutten, M. R. van Sambeek, F. N. van de Vosse, and R. G. Lopata, “Echo-Computed Tomography Strain Imaging of Healthy and Diseased Carotid Specimens,” *Ultrasound in Medicine & Biology*, vol. 40, no. 6, pp. 1329–1342, Jun. 2014.
- [101] M. U. Arabul, M. Heres, M. C. M. Rutten, M. R. van Sambeek, F. N. van de Vosse, and R. G. P. Lopata, “Toward the detection of intraplaque hemorrhage in carotid artery lesions using photoacoustic imaging,” *Journal of Biomedical Optics*, vol. 22, no. 4, p. 041 010, Dec. 23, 2016.
- [102] D. Yeager, A. Karpouk, B. Wang, J. Amirian, K. Sokolov, R. Smalling, and S. Emelianov, “Intravascular photoacoustic imaging of exogenously labeled atherosclerotic plaque through luminal blood,” *Journal of Biomedical Optics*, vol. 17, no. 10, p. 106 016, Oct. 17, 2012.
- [103] S. K. Jespersen, J. E. Wilhjelm, and H. Sillesen, “Multi-Angle Compound Imaging,” *Ultrasonic Imaging*, vol. 20, no. 2, pp. 81–102, Apr. 1, 1998.
- [104] G. Montaldo, M. Tanter, J. Bercoff, N. Benech, and M. Fink, “Coherent plane-wave compounding for very high frame rate ultrasonography and transient elastography,” *IEEE Transactions on Ultrasonics, Ferroelectrics and Frequency Control*, vol. 56, no. 3, pp. 489–506, Mar. 2009.
- [105] E. Tiran, T. Defieux, M. Correia, D. Maresca, B.-F. Osmanski, L.-A. Sieu, A. Bergel, I. Cohen, M. Pernot, and M. Tanter, “Multiplane wave imaging increases signal-to-noise ratio in ultrafast ultrasound imaging,” *Physics in Medicine and Biology*, vol. 60, no. 21, pp. 8549–8566, Nov. 7, 2015.
- [106] M. Jaeger, G. Held, S. Peeters, S. Preisser, M. Grünig, and M. Frenz, “Computed Ultrasound Tomography in Echo Mode for Imaging Speed of Sound Using Pulse-Echo Sonography: Proof of Principle,” *Ultrasound in Medicine & Biology*, vol. 41, no. 1, pp. 235–250, Jan. 2015.

- [107] X. L. Deán-Ben and D. Razansky, "On the link between the speckle free nature of optoacoustics and visibility of structures in limited-view tomography," *Photoacoustics*, vol. 4, no. 4, pp. 133–140, Oct. 25, 2016. PMID: 28066714.
- [108] H. J. Kang, M. A. L. Bell, X. Guo, and E. M. Boctor, "Spatial Angular Compounding of Photoacoustic Images," *IEEE Transactions on Medical Imaging*, vol. 35, no. 8, pp. 1845–1855, Aug. 2016.
- [109] M. U. Arabul, H. M. Heres, M. C. M. Rutten, M. R. H. M. van Sambeeky, F. N. van de Vosse, and R. G. P. Lopata, "Investigation of the effects of multi-angle compounding in photoacoustic imaging," *IEEE*, Sep. 2016, pp. 1–3.
- [110] P. Lai, X. Xu, and L. V. Wang, "Dependence of optical scattering from Intralipid in gelatin-gel based tissue-mimicking phantoms on mixing temperature and time," *Journal of Biomedical Optics*, vol. 19, no. 3, p. 035 002, Mar. 6, 2014.
- [111] J. R. Cook, R. R. Bouchard, and S. Y. Emelianov, "Tissue-mimicking phantoms for photoacoustic and ultrasonic imaging," *Biomedical Optics Express*, vol. 2, no. 11, p. 3193, Nov. 1, 2011.
- [112] W. J. Tompkins, *Biomedical Digital Signal Processing: C-Language Examples and Laboratory Experiments for the IBM PC*. Prentice Hall, 1993, 368 pp.
- [113] J. Laufer, D. Delpy, C. Elwell, and P. Beard, "Quantitative spatially resolved measurement of tissue chromophore concentrations using photoacoustic spectroscopy: Application to the measurement of blood oxygenation and haemoglobin concentration," *Physics in Medicine and Biology*, vol. 52, no. 1, pp. 141–168, Jan. 7, 2007.
- [114] B. T. Cox, J. G. Laufer, P. C. Beard, and S. R. Arridge, "Quantitative spectroscopic photoacoustic imaging: A review," *Journal of Biomedical Optics*, vol. 17, no. 6, p. 061 202, Jun. 2012.
- [115] N. Keshava and J. F. Mustard, "Spectral unmixing," *IEEE Signal Processing Magazine*, vol. 19, no. 1, pp. 44–57, 2002.
- [116] J. Glatz, N. C. Deliolas, A. Buehler, D. Razansky, and V. Ntziachristos, "Blind source unmixing in multi-spectral optoacoustic tomography," *Optics Express*, vol. 19, no. 4, p. 3175, Feb. 14, 2011.

-
- [117] S. Tzoumas, N. Deliolanis, S. Morscher, and V. Ntziachristos, "Unmixing Molecular Agents From Absorbing Tissue in Multispectral Optoacoustic Tomography," *IEEE Transactions on Medical Imaging*, vol. 33, no. 1, pp. 48–60, Jan. 2014.
 - [118] S. Tzoumas, A. Nunes, I. Olefir, S. Stangl, P. Symvoulidis, S. Glasl, C. Bayer, G. Multhoff, and V. Ntziachristos, "Eigenspectra optoacoustic tomography achieves quantitative blood oxygenation imaging deep in tissues," *Nature Communications*, vol. 7, p. 12 121, Jun. 30, 2016.
 - [119] G. S. Abela, Ed., *Lasers in Cardiovascular Medicine and Surgery: Fundamentals and Techniques*, Developments in Cardiovascular Medicine, Springer US, 1990.
 - [120] A. J. Welch and M. J. van Gemert, Eds., *Optical-Thermal Response of Laser-Irradiated Tissue*, 2nd ed., Springer Netherlands, 2011.
 - [121] L. An and B. Cox, "Independent component analysis for unmixing multi-wavelength photoacoustic images," A. A. Oraevsky and L. V. Wang, Eds., Mar. 18, 2016, p. 970 851.
 - [122] X. L. Deán-Ben, A. Buehler, D. Razansky, and V. Ntziachristos, "Estimation of optoacoustic contrast agent concentration with self-calibration blind logarithmic unmixing," *Physics in Medicine and Biology*, vol. 59, no. 17, pp. 4785–4797, Sep. 7, 2014.
 - [123] A. Hyvärinen and E. Oja, "Independent component analysis: Algorithms and applications," *Neural Networks*, vol. 13, no. 4-5, pp. 411–430, Jun. 2000.
 - [124] E. Oja and M. Plumbley, "Blind Separation of Positive Sources by Globally Convergent Gradient Search," *Neural Computation*, vol. 16, no. 9, pp. 1811–1825, Sep. 2004.
 - [125] Z. Yuan and E. Oja, "A FastICA Algorithm for Non-negative Independent Component Analysis," in *Independent Component Analysis and Blind Signal Separation*, C. G. Puntonet and A. Prieto, Eds., red. by D. Hutchison, T. Kanade, J. Kittler, J. M. Kleinberg, F. Mattern, J. C. Mitchell, M. Naor, O. Nierstrasz, C. Pandu Rangan, B. Steffen, M. Sudan, D. Terzopoulos, D. Tygar, M. Y. Vardi, and G. Weikum, vol. 3195, Berlin, Heidelberg: Springer Berlin Heidelberg, 2004, pp. 1–8.

- [126] M. U. Arabul, H. M. Heres, M. C. M. Rutten, M. R. H. M. van Sambeek, F. N. van de Vosse, and R. G. P. Lopata, "Investigation on the Effect of Spatial Compounding on Photoacoustic Images of Carotid Plaques in the In Vivo Available Rotational Range," *IEEE Transactions on Ultrasonics, Ferroelectrics, and Frequency Control*, vol. 65, no. 3, pp. 440–447, Mar. 2018.
- [127] I. V. Larina, K. V. Larin, and R. O. Esenaliev, "Real-time optoacoustic monitoring of temperature in tissues," *Journal of Physics D: Applied Physics*, vol. 38, no. 15, p. 2633, 2005.
- [128] J. Shah, S. Park, S. Aglyamov, T. Larson, L. Ma, K. Sokolov, K. Johnston, T. Milner, and S. Y. Emelianov, "Photoacoustic imaging and temperature measurement for photothermal cancer therapy," *Journal of Biomedical Optics*, vol. 13, no. 3, p. 034 024, 2008.
- [129] S. Morscher, J. Glatz, N. C. Deliolanis, A. Buehler, A. Sarantopoulos, D. Razansky, and V. Ntziachristos, "Spectral unmixing using component analysis in multispectral optoacoustic tomography," *OSA*, 2011, p. 80 890.
- [130] T. Buma, N. C. Conley, and S. W. Choi, "Multispectral photoacoustic microscopy of lipids using a pulsed supercontinuum laser," *Biomedical Optics Express*, vol. 9, no. 1, pp. 276–288, Dec. 19, 2017. pmid: 29359103.
- [131] L. V. Wang and S. Hu, "Photoacoustic Tomography: In Vivo Imaging from Organelles to Organs," *Science*, vol. 335, no. 6075, pp. 1458–1462, Mar. 23, 2012.
- [132] E. Aytac-Kipergil, A. Demirkiran, N. Uluc, S. Yavas, T. Kayikcioglu, S. Salman, S. G. Karamuk, F. O. Ilday, and M. B. Unlu, "Development of a Fiber Laser with Independently Adjustable Properties for Optical Resolution Photoacoustic Microscopy," *Scientific Reports*, vol. 6, no. 1, Dec. 2016.
- [133] C. Li and L. V. Wang, "Photoacoustic tomography and sensing in biomedicine," *Physics in Medicine and Biology*, vol. 54, no. 19, R59–R97, Oct. 7, 2009.
- [134] T. J. Allen and P. C. Beard, "Pulsed near-infrared laser diode excitation system for biomedical photoacoustic imaging," *Optics Letters*, vol. 31, no. 23, pp. 3462–3464, Dec. 1, 2006.
- [135] J. Yao and L. V. Wang, "Photoacoustic microscopy," *Laser & Photonics Reviews*, vol. 7, no. 5, pp. 758–778,

-
- [136] S. L. Jacques, "Coupling 3D Monte Carlo light transport in optically heterogeneous tissues to photoacoustic signal generation," *Photoacoustics*, vol. 2, no. 4, pp. 137–142, Dec. 2014.
- [137] M. A. Mastanduno and S. S. Gambhir, "Quantitative photoacoustic image reconstruction improves accuracy in deep tissue structures," *Biomedical Optics Express*, vol. 7, no. 10, p. 3811, Oct. 1, 2016.
- [138] B. T. Cox, S. R. Arridge, K. P. Köstli, and P. C. Beard, "Two-dimensional quantitative photoacoustic image reconstruction of absorption distributions in scattering media by use of a simple iterative method," *Applied Optics*, vol. 45, no. 8, p. 1866, Mar. 10, 2006.
- [139] B. Banerjee, S. Bagchi, R. M. Vasu, and D. Roy, "Quantitative photoacoustic tomography from boundary pressure measurements: Noniterative recovery of optical absorption coefficient from the reconstructed absorbed energy map," *JOSA A*, vol. 25, no. 9, pp. 2347–2356, Sep. 1, 2008.
- [140] Q. Fang, "Mesh-based Monte Carlo method using fast ray-tracing in Plücker coordinates," *Biomedical Optics Express*, vol. 1, no. 1, p. 165, Aug. 2, 2010.
- [141] R. Yao, X. Intes, and Q. Fang, "Generalized mesh-based Monte Carlo for wide-field illumination and detection via mesh retessellation," *Biomedical Optics Express*, vol. 7, no. 1, p. 171, Jan. 1, 2016.
- [142] P.-O. Persson and G. Strang, "A Simple Mesh Generator in MATLAB," *SIAM Review*, vol. 46, no. 2, pp. 329–345, Jan. 2004.
- [143] P.-O. Persson, "Mesh Generation for Implicit Geometries," Massachusetts Institute of Technology, 2005, 126 pp.
- [144] H. Si, "TetGen, a Delaunay-Based Quality Tetrahedral Mesh Generator," *ACM Transactions on Mathematical Software*, vol. 41, no. 2, pp. 1–36, Feb. 4, 2015.
- [145] R. Yao, X. Intes, and Qianqian Fang, "Re-tessellated mesh-based Monte Carlo for wide-field illumination sources," *IEEE*, Apr. 2015, pp. 1–2.
- [146] G. M. Hale and M. R. Querry, "Optical Constants of Water in the 200-nm to 200-Mm Wavelength Region," *Applied Optics*, vol. 12, no. 3, p. 9, 1973.
- [147] X. Ma, J. Q. Lu, H. Ding, and X.-H. Hu, "Bulk optical parameters of porcine skin dermis at eight wavelengths from 325 to 1557 nm," *Optics Letters*, vol. 30, no. 4, pp. 412–414, Feb. 15, 2005.

- [148] H. Ding, J. Q. Lu, K. M. Jacobs, and X.-H. Hu, "Determination of refractive indices of porcine skin tissues and Intralipid at eight wavelengths between 325 and 1557 nm," *JOSA A*, vol. 22, no. 6, pp. 1151–1157, Jun. 1, 2005.
- [149] R. L. van Veen, H. Sterenborg, A. Pifferi, A. Torricelli, and R. Cubeddu, "Determination of VIS- NIR absorption coefficients of mammalian fat, with time- and spatially resolved diffuse reflectance and transmission spectroscopy," OSA, 2004, SF4.
- [150] D. Levitz, L. Thrane, M. H. Frosz, P. E. Andersen, C. B. Andersen, S. Andersson-Engels, J. Valanciunaite, J. Swartling, and P. R. Hansen, "Determination of optical scattering properties of highly-scattering media in optical coherence tomography images," *Optics Express*, vol. 12, no. 2, p. 249, 2004.
- [151] A. N. Bashkatov, E. A. Genina, and V. V. Tuchin, "Optical Properties of Skin, Subcutaneous, and Muscle Tissues: A Review," *Journal of Innovative Optical Health Sciences*, vol. 04, no. 01, pp. 9–38, Jan. 2011.
- [152] M. Keijzer, R. R. Richards-Kortum, S. L. Jacques, and M. S. Feld, "Fluorescence spectroscopy of turbid media: Autofluorescence of the human aorta," *Applied Optics*, vol. 28, no. 20, p. 4286, Oct. 15, 1989.
- [153] F. J. van der Meer, D. J. Faber, I. F. Cilesiz, M. J. C. van Gemert, and T. G. van Leeuwen, "Temperature-dependent optical properties of individual vascular wall components measured by optical coherence tomography," *Journal of Biomedical Optics*, vol. 11, no. 4, p. 041 120, Jul. 2006.
- [154] S. A. Prahl, "Light transport in tissue," The University of Texas at Austin, 1988.
- [155] N. Bosschaart, G. J. Edelman, M. C. G. Aalders, T. G. van Leeuwen, and D. J. Faber, "A literature review and novel theoretical approach on the optical properties of whole blood," *Lasers in Medical Science*, vol. 29, no. 2, pp. 453–479, Mar. 2014.
- [156] B. E. Treeby and B. T. Cox, "K-Wave: MATLAB toolbox for the simulation and reconstruction of photoacoustic wave fields," *Journal of Biomedical Optics*, vol. 15, no. 2, p. 021 314, Mar. 2010.
- [157] B. Treeby, B. Cox, and J. Jaros, *A MATLAB Toolbox for the Time Domain Simulation of Acoustic Waves: User Manual*. 2016.

-
- [158] D.-K. Yao, C. Zhang, K. Maslov, and L. V. Wang, "Photoacoustic measurement of the Grüneisen parameter of tissue," *Journal of Biomedical Optics*, vol. 19, no. 1, p. 17 007, Jan. 2014. pmid: 24474512.
- [159] P. A. Hasgall, F. Di Gennaro, C. Baumgartner, E. Neufeld, B. Lloyd, M. C. Gosselin, D. Payne, A. Kligenböck, and N. Kuster, "IT'IS Database for thermal and electromagnetic parameters of biological tissues," *ITIS Database*, 2018, Version 4.0.
- [160] C. Bonn  ry, M. Desjardins, P. Pouliot, F. Lesage, P.-O. Leclerc, R. D. Hoge, and L. Bherer, "Changes in diffusion path length with old age in diffuse optical tomography," *Journal of Biomedical Optics*, vol. 17, no. 5, p. 056 002, May 2012.
- [161] Y. Shin and H.-S. Kwon, "Mesh-based Monte Carlo method for fibre-optic optogenetic neural stimulation with direct photon flux recording strategy," *Physics in Medicine & Biology*, vol. 61, no. 6, p. 2265, 2016.
- [162] T. J. Allen, A. Hall, A. Dhillon, J. S. Owen, and P. C. Beard, "Photoacoustic imaging of lipid rich plaques in human aorta," A. A. Oraevsky and L. V. Wang, Eds., Feb. 11, 2010, p. 75640C.
- [163] P. Wang, T. Ma, M. N. Slipchenko, S. Liang, J. Hui, K. K. Shung, S. Roy, M. Sturek, Q. Zhou, Z. Chen, and J.-X. Cheng, "High-speed Intravascular Photoacoustic Imaging of Lipid-laden Atherosclerotic Plaque Enabled by a 2-kHz Barium Nitrite Raman Laser," *Scientific Reports*, vol. 4, p. 6889, Nov. 4, 2014.
- [164] C. Yuan, L. M. Mitsumori, M. S. Ferguson, N. L. Polissar, D. Echelard, G. Ortiz, R. Small, J. W. Davies, W. S. Kerwin, and T. S. Hatsukami, "In Vivo Accuracy of Multispectral Magnetic Resonance Imaging for Identifying Lipid-Rich Necrotic Cores and Intraplaque Hemorrhage in Advanced Human Carotid Plaques," *Circulation*, vol. 104, no. 17, pp. 2051–2056, Oct. 23, 2001.
- [165] M. Shinnar, J. T. Fallon, S. Wehrli, M. Levin, D. Dalmacy, Z. A. Fayad, J. J. Badimon, M. Harrington, E. Harrington, and V. Fuster, "The Diagnostic Accuracy of Ex Vivo MRI for Human Atherosclerotic Plaque Characterization," *Arteriosclerosis, Thrombosis, and Vascular Biology*, vol. 19, no. 11, pp. 2756–2761, Nov. 1, 1999.

- [166] T. Funaki, K. Iihara, S. Miyamoto, K. Nagatsuka, T. Hishikawa, and H. Ishibashi-Ueda, "Histologic characterization of mobile and nonmobile carotid plaques detected with ultrasound imaging," *Journal of Vascular Surgery*, vol. 53, no. 4, pp. 977–983, Apr. 2011.
- [167] M. R. Prausnitz and R. Langer, "Transdermal drug delivery," *Nature Biotechnology*, vol. 26, no. 11, pp. 1261–1268, Nov. 2008.
- [168] M. A. Kosoglu, R. L. Hood, Y. Chen, Y. Xu, M. N. Rylander, and C. G. Rylander, "Fiber Optic Microneedles for Transdermal Light Delivery: Ex Vivo Porcine Skin Penetration Experiments," *Journal of Biomechanical Engineering*, vol. 132, no. 9, p. 091 014, Sep. 1, 2010.
- [169] R. G. P. Lopata, H. H. G. Hansen, M. M. Nillesen, J. M. Thijssen, L. Kapusta, and C. L. de Korte, "Methodical study on the estimation of strain in shearing and rotating structures using radio frequency ultrasound based on 1-D and 2-D strain estimation techniques," *IEEE Transactions on Ultrasonics, Ferroelectrics, and Frequency Control*, vol. 57, no. 4, pp. 855–865, Apr. 2010.
- [170] R. G. P. Lopata, M. M. Nillesen, J. M. Thijssen, L. Kapusta, and C. L. de Korte, "Three-Dimensional Cardiac Strain Imaging in Healthy Children Using RF-Data," *Ultrasound in Medicine & Biology*, vol. 37, no. 9, pp. 1399–1408, Sep. 1, 2011.
- [171] R. W. Boekhoven, M. C. Rutten, M. R. van Sambeek, F. N. van de Vosse, and R. G. Lopata, "Towards mechanical characterization of intact endarterectomy samples of carotid arteries during inflation using Echo-CT," *Journal of Biomechanics*, vol. 47, no. 4, pp. 805–814, Mar. 2014.

